SLAC-R-669
UC-414

Measurement of R_b at SLD*

Jeffrey Aaron Snyder

Stanford Linear Accelerator Center
Stanford University
Stanford, CA 94309

SLAC-Report-669
May 1994

Prepared for the Department of Energy
under contract number DE-AC03-76SF00515

Printed in the United States of America. Available from the National Technical Information Service, U.S. Department of Commerce, 5285 Port Royal Road, Springfield, VA 22161.

* Ph.D. thesis, Yale University, New Haven, CT 06511

ABSTRACT

MEASUREMENT OF R_b AT SLD

Jeffrey Aaron Snyder
Yale University
May 1994

In 1992 the SLAC Large Detector (SLD) recorded over 10,000 decays of Z^0 bosons produced in e^+e^- collisions at the SLAC Linear Collider (SLC). We search through these decays for $Z^0 \to q\bar{q}$ events and then tag $Z^0 \to b\bar{b}$ events. From these numbers and the estimated tagging efficiencies, we measure $R_b \equiv \Gamma(Z^0 \to b\bar{b})/\Gamma(Z^0 \to q\bar{q})$. The tagging method used is to count the number of well–measured tracks with highly significant three–dimensional impact parameters. The significance of an impact parameter is defined as the impact parameter divided by the expected uncertainty in that impact parameter. This method should provide an excellent measurement of R_b because of SLD's vertex detector, which measures true three–dimensional space points and has a very small inner radius. Also, SLC's interaction point is well defined and stable. Requiring three or more tracks with significance of 3.0 or greater leads to a result of:

$$\begin{aligned} R_b &= 0.2270 \pm 0.0075_{(\text{stat.})} \pm 0.0091_{(\text{syst.})} \pm 0.0040_{(R_c)} \\ \Rightarrow R_b &= 0.227 \pm 0.012 \end{aligned}$$

This compares well with the current best measurement, $R_b = 0.2192 \pm 0.0037$, and with the minimal standard model expectation, $0.215 < R_b < 0.220$, for the allowed range of m_t and M_H. This measurement is not precise enough to place any significant constraints on the minimal standard model or new physics. As SLD accumulates more statistics and the Monte Carlo simulation is further refined, the uncertainty will decline and we will be able to probe the standard model at a telling level.

MEASUREMENT OF R_b AT SLD

A Dissertation
Presented to the Faculty of the Graduate School
of
Yale University
in Candidacy for the Degree of
Doctor of Philosophy

By
Jeffrey Aaron Snyder
May 1994

Advisor: Professor Charles Baltay

Acknowledgements

I would like to thank many people for making these last six years so instructive and memorable. I am indebted to my thesis advisor, Charlie Baltay, for his insightful guidance and for inspiring me with the love of physics. Steve Manly has also been an invaluable mentor and friend.

I wish to thank Sara Batter and Jean Belfonti for providing a buffer zone between the graduate school and us graduate students, Peter Martin for solving the myriad problems thrown his way and Rochelle Lauer for keeping the computer system from ruining our lives. I am indebted to the rest of the fifth–floor gang: Brenda Kuhn–Alexy, Jean Ahern, Carole DeVore and Harley Pretty for their assistance over the years.

I would like to acknowledge my thesis committee: Paul Karchin, Peter Parker, Charles Sommerfield, Michael Zeller and my outside reader, Konstantin Goulianos for their careful reading of this thesis and their helpful comments.

I am grateful for the support of my friends and fellow graduate students. Ram Ben–David has helped me in countless ways. Abhay Deshpande and Chris Darling have always been there for any kind of discussion, as well as the coffee club. Frank Rotondo and Karen Ohl have assisted in many ways, both as graduate students and as post–docs. Many others, including Sumit Sen, Jeff Turk, Doug Bergman and Rob Harr have helped me retain my sanity.

This thesis would never have been started without the hard work of the endcap CRID group, including Dick Plano, Ken Baird, Scott Geary, Sridhara Dasu and Stephane Willocq. Especially important were our engineer Will Emmet and our "super–tech" John Sinnott. This analysis would never have been finished without

the help of the SLD R_b group: Su Dong and Homer Neal, and the SLD B physics task force, including Rafe Schindler, Mike Strauss, Greg Punkar and Sarah Hedges.

Finally I reserve my deepest gratitude for my wife, Debbie Krauss, whose unending love has kept me going and who has helped me in more ways than I can express. I also want to thank my parents, Charles and Harriet Snyder, and the rest of my family for their love, guidance and encouragement over the years. Without them, none of this would have been possible.

Contents

List of Figures

List of Tables

Chapter 1

Introduction

The branching fraction ratio R_b measures the coupling of b quarks to the Z^0 boson. If measured precisely enough, R_b is sensitive to $Zb\bar{b}$ vertex corrections, although it is insensitive to other radiative corrections and oblique (vacuum polarization) corrections. In this manner it is possible to see effects from particles too heavy to observe directly. This analysis measures R_b from a sample of about 10,200 polarized Z^0's produced at the Stanford Linear Accelerator Center (SLAC) and detected by the SLAC Large Detector (SLD) from March through September 1992. By making full use of the SLD's high–precision vertex detector, we determine the three–dimensional impact parameter and the expected uncertainty in the impact parameter for all well–measured tracks. We measure R_b by tagging b–quark events. Events that contain a number of tracks with impact parameters significantly greater than their expected uncertainty are tagged as b–quark events.

1.1 The Standard Model

The standard model of strong and electroweak interactions describes all the known particles and their interactions, with the exception of gravity.[1] It is based on local $SU(3)_c \otimes SU(2)_L \otimes U(1)_Y$ gauge symmetry and encompasses quantum chromodynamics (QCD), quantum electrodynamics (QED) as well as weak interactions. There is direct evidence for all of the leptons, quarks and gauge bosons in the standard model

with the exception of the t quark and the τ neutrino, for which there is only indirect evidence.

The standard model has been a spectacular success, predicting the W and Z bosons with good approximations of their masses,* but it cannot appropriately explain the symmetry breaking that causes the basic fermions to have mass. The "minimal" standard model (MSM) accounts for this symmetry breaking via the Higgs mechanism which results in a massive scalar boson. No evidence for this Higgs boson has been found to date. The basic particles in the MSM are listed in table 1.1.[2]

Class	Particle	Symbol	Spin	Coulomb charge
Leptons	Electron neutrino	ν_e	1/2	0
	Electron	e	1/2	-1
	Muon neutrino	ν_μ	1/2	0
	Muon	μ	1/2	-1
	Tau neutrino	ν_τ	1/2	0
	Tau	τ	1/2	-1
Quarks	Up quark	u	1/2	$+2/3$
	Down quark	d	1/2	$-1/3$
	Charm quark	c	1/2	$+2/3$
	Strange quark	s	1/2	$-1/3$
	Top quark	t	1/2	$+2/3$
	Bottom quark	b	1/2	$-1/3$
Gauge	Photon	γ	1	0
Bosons	W Boson	$W^\pm$	1	± 1
	Z Boson	Z^0	1	0
	Gluon	g	1	0
Higgs	Higgs scalar	H	0	0

Table 1.1: Properties of basic particles in the minimal standard model.

There are many extensions to the MSM which are neither in disagreement with experimental data nor theoretically problematic. These extensions include extra Higgs–type fields, supersymmetric theories and technicolor theories, to name just a few.[3] We may categorize all of these theories which remain for us to experimentally prove

*This is true given a measurement of the Weinberg angle, *e.g.* from neutrino scattering

or disprove as possible "new physics."

Precision measurements of electroweak observables test the validity of the MSM and can act as a window on new physics. According to the MSM, loop effects cause small, calculable deviations from the lowest order predictions. These radiative corrections depend on the top and Higgs masses and are generally expected to be of order 1%. The effects of new physics depend strongly on the details of the theory, but for the most part these effects are also expected to be of order 1%.[4]

1.2 Theory

1.2.1 Z^0 partial decay widths

The partial decay width of the Z^0 boson into a quark species, $\Gamma_{q\bar{q}} \equiv \Gamma(Z^0 \to q\bar{q})$, in the MSM depends on the weak isospin of the quark. At the tree–level[†] this is given by the Born approximation:[5]

$$\Gamma^0_{q\bar{q}} = \beta \left(\frac{3 - \beta^2}{2} \right) \Gamma^V_0 + \beta^3 \Gamma^A_0 \tag{1.1}$$

where the velocity, $\beta \equiv \sqrt{1 - 4m_q^2/s}$, is approximately unity for all allowed quark species. We have used:

$$\Gamma^V_0 = \frac{G_{\rm F} M_Z^3}{8\sqrt{2}\pi} v_q^2 \qquad \text{and} \qquad \Gamma^A_0 = \frac{G_{\rm F} M_Z^3}{8\sqrt{2}\pi} a_q^2$$

where $G_{\rm F}$ is the Fermi coupling constant and the vector and axial vector couplings are given by:

$$v_q = 2t^q_{3L} - 4Q_q \sin^2\theta_W \qquad \text{and} \qquad a_q = 2t^q_{3L}$$

where t^q_{3L} is the weak isospin Z–component of quark q and Q_q is its Coulomb charge. For up–type quarks this reduces to $v_u = 1 - \frac{8}{3}\sin^2\theta_W = 0.380$ and $a_u = 1$; for down–type quarks, $v_d = -1 + \frac{4}{3}\sin^2\theta_W = -0.690$ and $a_d = -1$. We have taken the world–average values for $\sin^2\theta_W = 0.2325$, $M_Z = 91.173$ GeV/c^2 and $G_{\rm F} = 1.16639 \times 10^{-5}$ GeV^{-2}.[6] This leads to tree–level partial widths:

[†] All Feynman diagrams that can be split in half by breaking a single line

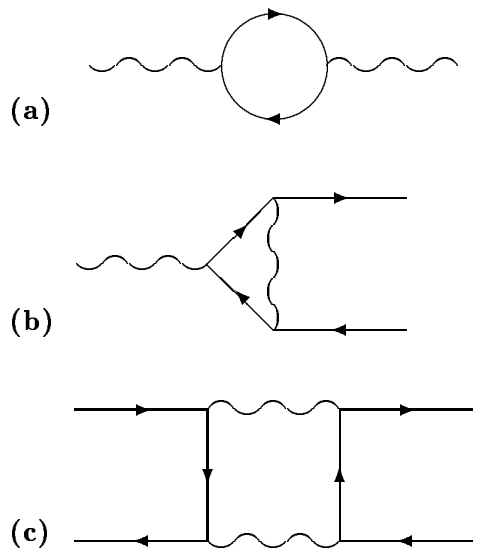

Figure 1.1: Generic loop level corrections: (a) Oblique, (b) Vertex, (c) Box

$$\begin{aligned}
\Gamma^0_{u\bar{u}} &= 284.6\ \text{MeV} \\
\Gamma^0_{d\bar{d}} &= 367.1\ \text{MeV} \\
\Gamma^0_{c\bar{c}} &= 284.2\ \text{MeV} \\
\Gamma^0_{s\bar{s}} &= 367.1\ \text{MeV} \\
\Gamma^0_{b\bar{b}} &= 362.9\ \text{MeV}
\end{aligned}$$

1.2.2 Corrections to the $\Gamma_{q\bar{q}}$

There are three classes of loop–level modifications to the lowest–order predictions of the MSM (see figure 1.1):[4, 7]

(a) Oblique (or vacuum polarization) corrections tend to lead to large effects because of the running of α_{EM} and smaller — but still measurable — effects from top quarks and Higgs scalars.

(b) Vertex corrections are small, but still observable. In general they are well understood within the standard model, but the $Z^0 \to b\bar{b}$ vertex has corrections

which are sensitive to the mass of the top quark and to much of the proposed new physics.

(c) Box corrections are very small and can usually be ignored.

Following the Kennedy–Lynn formalism,[8] we define the vacuum polarization amplitudes (self–energies) $\Pi_{ij} \equiv \langle J_i J_j \rangle$ where the photon, Z and $W^{\pm}$ currents are:

$$J_A = e_0 J_Q \tag{1.2}$$

$$J_Z = \frac{e_0}{s_0 c_0}\left(J_3 - s_0 J_Q\right) \tag{1.3}$$

$$J_{\pm} = \frac{e_0}{s_0}\left(\frac{J_1 \pm i J_2}{\sqrt{2}}\right) \tag{1.4}$$

We have used e_0 as the bare electric charge; s_0 and c_0 as the sine and cosine of the (bare) weak mixing angle; and J_Q, J_1, J_2 and J_3 as the electromagnetic and weak–isospin currents. Thus:

$$\Pi_{AA} = e_0^2 \Pi_{QQ} \tag{1.5}$$

$$\Pi_{ZA} = \frac{e_0^2}{s_0 c_0}\left(\Pi_{3Q} - s_0^2 \Pi_{QQ}\right) \tag{1.6}$$

$$\Pi_{ZZ} = \frac{e_0^2}{s_0^2 c_0^2}\left(\Pi_{33} - 2 s_0^2 \Pi_{3Q} + s_0^4 \Pi_{QQ}\right) \tag{1.7}$$

$$\Pi_{WW} = \frac{e_0^2}{s_0^2}\Pi_{+-} = \frac{e_0^2}{s_0^2}\Pi_{11} \tag{1.8}$$

It is convenient to define $\Pi'_{ij}(q^2)$ by:

$$\Pi_{ij}(q^2) \equiv \Pi_{ij}(0) + q^2 \Pi'_{ij}(q^2) \tag{1.9}$$

such that at $q^2 = 0$, $\Pi'_{ij} = \frac{d}{dq^2}\left(\Pi_{ij}\right)$.[7]

The oblique corrections affect the Z^0 propagator in three combinations (a fourth combination affects only the $W^{\pm}$ propagator):[9]

$$\Delta_\alpha(M_Z^2) \equiv \Pi'_{(AA)}(0) - \Pi'_{(AA)}(M_Z^2)$$

$$\Delta_\rho(0) \equiv \frac{\Pi_{(ZZ)}(0)}{M_Z^2} - \frac{\Pi_{(WW)}(0)}{M_W^2}$$

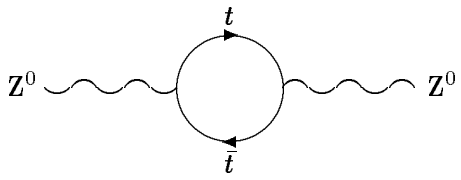

Figure 1.2: Leading Z^0 vacuum polarization correction.

$$\Delta_{3Q}(M_Z^2) \equiv \frac{e^2}{s^2c^2}\left[\frac{\Pi_{(33)}(M_Z^2)-\Pi_{(33)}(0)}{M_Z^2} - \frac{\Pi_{(3Q)}(M_Z^2)}{M_Z^2}\right]$$

One can absorb the Δ_α term into a redefinition of the electric charge:

$$\alpha \longrightarrow \alpha^* \equiv \alpha(M_Z) \simeq 1/128.8 \tag{1.10}$$

Δ_ρ contains the oblique corrections to the ρ–parameter,[10][‡] which have been investigated extensively.[9, 12, 13] For large top mass the dominant correction is from a $t\bar{t}$ loop (see fig. 1.2), hence:

$$\Delta_\rho^{(t)}(0) \simeq \frac{\alpha}{\pi}\frac{m_t^2}{M_Z^2} \tag{1.11}$$

There is also a smaller correction from the Higgs scalar that comes in with the opposite sign:

$$\Delta_\rho(0) \equiv \Delta_\rho^{(t)}(0) + \Delta_\rho^{(H)}(0) \simeq \frac{\alpha}{\pi}\frac{m_t^2}{M_Z^2} - \frac{\alpha}{4\pi}\ell n\frac{M_H^2}{M_Z^2} \tag{1.12}$$

The Z^0–γ cross–current term is not affected by the top quark, and it is quite small.

$$\Delta_{3Q}^{(H)}(M_Z^2) \simeq -\frac{\alpha}{9\pi}\ell n\frac{M_H^2}{M_Z^2} \tag{1.13}$$

The partial widths have been calculated by Renard and Verzegnassi:[9]

$$\Gamma_{u\bar{u}} \simeq \frac{5\alpha^* M_Z}{72 s_0^2 c_0^2}\left[1 + \frac{8}{5}\Delta_\rho(0) + \frac{3}{5}\Delta_{3Q}\right] \tag{1.14}$$

$$\Gamma_{d\bar{d}} \simeq \frac{13\alpha^* M_Z}{144 s_0^2 c_0^2}\left[1 + \frac{19}{13}\Delta_\rho(0) + \frac{6}{13}\Delta_{3Q}\right] \tag{1.15}$$

$\Gamma_{c\bar{c}}$ and $\Gamma_{s\bar{s}}$ follow, but $\Gamma_{b\bar{b}}$ must include the $Zb\bar{b}$ vertex correction, Δ_{bV}. This is dominated by terms from virtual t–W exchange (see fig. 1.3):[14, 15]

[‡] $\Delta_\rho(0) \equiv \rho - 1$. The ρ–parameter measures the relative strength of charged and neutral weak currents.[11, p. 100]

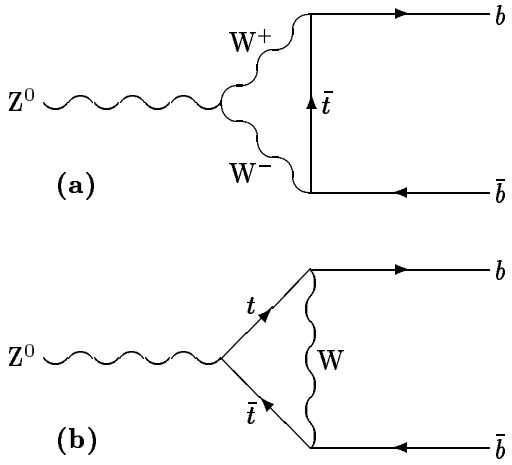

Figure 1.3: Z^0–b vertex corrections.

$$\Delta_{bV}^{(t)}(0) \simeq -\frac{20}{19}\frac{\alpha}{\pi}\left[\frac{m_t^2}{M_Z^2} + \frac{13}{6}\ell n\frac{m_t^2}{M_Z^2}\right] \tag{1.16}$$

The MSM Higgs does not contribute at all to Δ_{bV}.[9, 12] Similar vertex corrections exist for all quark flavors, but the Cabibbo–Kobayashi–Maskawa (CKM) mixing matrix suppresses these diagrams except the b's.[4] Note that this definition of Δ_{bV} is not universally accepted. Some authors[16, 4] define $\Delta_{bV} \equiv (\Gamma_{b\bar{b}}/\Gamma_{d\bar{d}}) - 1$, with the result that their Δ_{bV} is $\frac{19}{13}$ larger. We use the Δ_{bV} in equation 1.16 which introduces Δ_{bV} and Δ_ρ with the same coefficient.

$$\Gamma_{b\bar{b}} \simeq \frac{13\alpha^* M_Z}{144 s_0^2 c_0^2}\left[1 + \frac{19}{13}\left(\Delta_\rho(0) + \Delta_{bV}^{(t)}\right) + \frac{6}{13}\Delta_{3Q}\right] \tag{1.17}$$

Here $s_0^2 = \frac{1}{2}\left(1 - \sqrt{1 - \frac{4\mu^2}{M_Z^2}}\right)$, $\mu^2 = (38.45\,\mathrm{GeV})^2$ and $c_0^2 = 1 - s_0^2$ hence $s_0^2 = 0.2314, c_0^2 = 0.7686$.

Note that the oblique correction tends to cancel the vertex correction, leaving $\Gamma_{b\bar{b}}$ insensitive to m_t.[4]

$$\Gamma_{bb} = \Gamma_{bb}^0\left[1 - 0.05\frac{\alpha}{\pi}\frac{m_t^2}{M_Z^2} + \cdots\right] \tag{1.18}$$

1.2.3 R_b

From a theoretical standpoint, $R_b \equiv \Gamma_{b\bar{b}}/\Gamma_{\rm had}$ isolates Δ_{bV} from the other MSM corrections and is therefore a cleaner measure of the top mass. The final state QCD corrections, which are large, are flavor independent and thus cancel completely in the ratio. This is strictly true only if quark masses are zero, but the correction due to finite b mass is under 0.5%, so its associated error is negligible.[16] The oblique corrections are common to all fermions, hence they will also largely cancel when taking ratios.[13] This cancellation can be demonstrated using the partial widths reported above (equations 1.14, 1.15 and 1.17):

$$\begin{aligned}
\Gamma_{\rm had} &= \Gamma_{u\bar{u}} + \Gamma_{d\bar{d}} + \Gamma_{c\bar{c}} + \Gamma_{s\bar{s}} + \Gamma_{b\bar{b}} && (1.19)\\
\Rightarrow \Gamma_{\rm had} &\simeq \frac{59\alpha^* M_Z}{144 s_0^2 c_0^2}\left[1 + \frac{89}{59}\Delta_\rho(0) + \frac{19}{59}\Delta_{bV} + \frac{30}{59}\Delta_{3Q}\right] && (1.20)\\
\Rightarrow R_b &\simeq \frac{13}{59}\left[1 - \frac{36}{767}\Delta_\rho(0) + \frac{874}{767}\Delta_{bV} - \frac{36}{767}\Delta_{3Q}\right] && (1.21)\\
\Rightarrow R_b &\simeq 0.2203\left[1 - 0.047\Delta_\rho(0) + 1.14\Delta_{bV} - 0.047\Delta_{3Q}\right] && (1.22)
\end{aligned}$$

where we have neglected all terms of order $(\Delta)^2 \sim (m_t/M_Z)^4$ and higher. As described previously, the $\Delta_\rho(0)$ and Δ_{bV} corrections are in the range of 0.003 to 0.012 while Δ_{3Q} is under 0.002 for allowed values of m_t and M_{H^0}. In the ratio R_b, each of these corrections is multiplied by a coefficient. For $\Delta_\rho(0)$ and Δ_{3Q} the coefficients reduce their effect, while the effect of Δ_{bV} is increased by its coefficient.

This calculation is in agreement with a calculation done by Swartz, using slightly different notation:[4]

$$R_b = 0.2196\left[1 + 0.78\nabla_b^{(t)} - 0.06\nabla_\rho^{(t)} + \cdots\right] \qquad (1.23)$$

where:

$$\nabla_b^{(t)} \simeq -\frac{20}{13}\frac{\alpha}{\pi}\frac{m_t^2}{M_Z^2} \simeq \frac{19}{13}\Delta_{bV} \qquad (1.24)$$

1.2.4 New physics

The $Zb\bar{b}$ vertex is a good place to search for new physics that involves mass–dependant couplings, since the b–quark is the heaviest fermion produced in Z^0 decays.[4] Once

m_t is known, R_b will be a sensitive measure of new physics since it is not sensitive to MSM radiative and QCD corrections which are difficult to calculate. However, some extensions to the standard model do not contribute any corrections to R_b and must be detected by other methods. These extensions include extra families and non–canonical neutral higgses.[13]

Charged higgses can introduce significant corrections. Given an extra doublet of higgses with vacuum expectation values of v_1 and v_2, the dominant term in $\Delta_{bV}^{(H^+)}$ is proportional to $\frac{m_t^2}{M_Z^2 \tan^2\beta}$ where $\tan\beta \equiv \frac{v_2}{v_1}$. The dependence on M_{H^+} is weak. This dominant correction comes from virtual t–$H^\pm$ exchange similar to the virtual t–W exchange shown in figure 1.3.[4] Most models favor $\tan\beta \in [1, 10]$. The net effect of charged higgses is to enhance the MSM top contribution by 2% or less.[13]

Supersymmetric models (SUSYs) naturally contain charged higgses so the above discussion holds true. In addition the neutralino and chargino have a number of diagrams which could introduce corrections. However, most of these contributions are negligible.[17] The maximum contribution allowed within experimental bounds is sizable, but in all cases the maxima are near the experimental limits and the contributions away from the limits are small. These contributions have been calculated by Djouadi[13]: The maximum contribution from standard SUSY charginos within experimental limits is 0.015 compared to 0.015 from $m_t = 150$ GeV and 0.005 from $m_{H^+} = 100$ GeV. There is still some debate over the sign of these corrections in the minimal supersymmetric model (MSSM).[18]

Figure 1.4[18] shows R_b as a function of the top mass for three different models. The parameters for these models are chosen to show a maximal effect without disagreeing with current experimental limits. The parameters are: $\tan\beta = 1$, $M = 50$ GeV, $\mu = 30$ GeV and $\widetilde{m_t} = M_{H^+} = 100$ GeV. The mass of the MSM Higgs has little effect — roughly the width of each line for the entire allowed range.

Extra Z–type particles can cause two different kinds of effects. In one case the mixing can be reabsorbed into a redefinition of the ρ parameter:

$$\delta\rho^{(Z')} \sim \frac{\theta_m^2}{\epsilon} \qquad \text{where} \qquad \epsilon = M_Z^2/M_{Z'}^2 \tag{1.25}$$

In the other case there is pure mixing and $\delta_m \simeq \theta_m$. This is a tree–level effect and

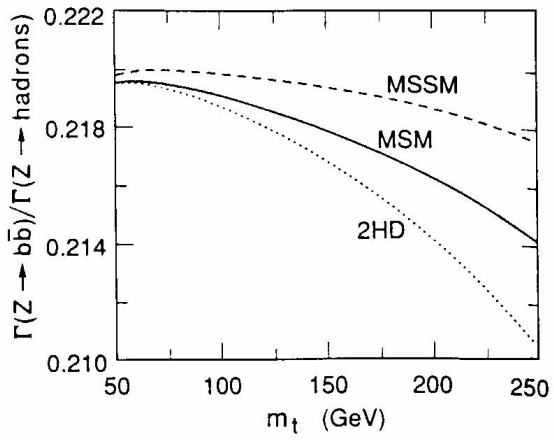

Figure 1.4: R_b as a function of the top mass in the minimal standard model (MSM), the minimal supersymmetric model (MSSM) and the two Higgs doublet (2HD) model.

cannot be reabsorbed into either Δ_ρ or δ_{bV}.[13]

1.3 Recent Results

1.3.1 R_b measurements

R_b has been measured previously by the MarkII, ALEPH, DELPHI, L3, OPAL and SLD collaborations using many different methods (see references [19] through [39] and table 1.2). The most common method looks for leptons with high momentum and high transverse momentum. Because of the large B meson mass and high semi–leptonic branching ratio, this method preferentially selects $b \to \ell X$ events over $b \to c \to \ell X$, $c \to \ell X$ and other background events. However, in order to determine R_b, the B semi–leptonic branching ratio must be factored out. Most of these analyses use an average of PEP and PETRA measurements which introduces a 7% uncertainty from this branching ratio. The CLEO and ARGUS collaborations have made more precise measurements, but since they run at the $\Upsilon(4S)$, only $B_u^\pm$ and B_d^0 mesons are accessible. One must then make an assumption about the semi–leptonic branching ratios and relative abundance of B_s^0 and $B_c^\pm$ mesons as well as B baryons. This assumption also introduces a comparable systematic uncertainty. With high–p_t lepton tags one can obtain purities of 80%—90% but the overall efficiency (including the

semi–leptonic branching ratio) is only 1%—6%. This assumes that both electron and muon channels are summed and some fraction of the tau channel is included via $\tau \to e$ and $\tau \to \mu$. Recently L3 has reported[28] a measurement of $\mathrm{Br}(b \to \ell X)$ that is nearly independent of R_b. However, that analysis depends on double tagging high–p_t leptons, and the total error is about 10% (statistically limited with 115,000 Z^0's). Similarly, DELPHI[23] has measured R_b by fitting the $p_t \times p$ distribution of all leptons. This method suffers from all of the above branching ratio problems, plus the fit introduces more model dependence on the shape of the distributions.

Several collaborations have reported results from using neural networks to tag events using many variables and their correlations.[21, 26, 29] This method can produce overall efficiencies of 35%—55% but the b purity suffers, dropping to 45%—60%. The neural network requires a "training" procedure to determine the node interconnection weights. The results are systematically sensitive to the Monte Carlo model (and its parameters) that are used in the training procedure. The dominant systematic error is in most cases the uncertainty in the b fragmentation function. DELPHI's later paper reports a 7.3% systematic error while L3 reports a 3.2% systematic error. The L3 error is lower primarily due to the choice of variables: L3 does not use any high–p_t lepton information as input to the neural network. Both of the above neural networks use the boosted sphericity product as an input variable. ALEPH combines a neural network tag and a high–p_t lepton tag to get a 2.2% systematic error. DELPHI has also reported[22, 24] results from fitting the boosted sphericity product alone. The results are very model dependant and the more recent paper reports a systematic error of 8.7%.

More recently, collaborations have been using impact parameter analyses.[20, 25, 31, 35, 37, 38, 39] An impact parameter analysis requires thorough understanding of the detector's tracking systematics and the ability to reconstruct the primary vertex with high accuracy. Generally these analyses project all tracks into the xy–plane (perpendicular to the beam) and calculate two–dimensional impact parameters. Using two–dimensional impact parameters essentially eliminates the dependence of R_b on the z position of the primary vertex (which is least well defined) and greatly reduces the dependence of R_b on the z alignment of the detector. In all of the detectors

except ALEPH and SLD, the vertex detector has poor z resolution, so including the z coordinate is not helpful. With sufficient data, the Monte Carlo dependence of impact parameter tag methods can be essentially removed by tagging hemispheres independently and then measuring ϵ_b from the number of events where both hemispheres are tagged. The double–tag method assumes that the probability of a $b\bar{b}$ pair emerging from the void is negligible. This assumption must be sound, otherwise many events would have several B hadrons in one hemisphere and none in the other. Previous impact parameter–based measurements of R_b are described below:

MarkII had two detectors for measuring the vertices: a drift chamber vertex detector (DCVD) which was a scaled–down version of their central drift chamber, and a silicon strip vertex detector (SSVD) which had three layers of silicon microstrips at radii of 29, 33 and 37 mm. This was the first use of silicon microstrips in a collider environment. MarkII's analysis was able to achieve b tagging efficiency, ϵ_b, of 50% and b tagging purity, Π_b, of 85%: they measured $R_b = 0.251 \pm 0.057$.[31] The analysis was statistically limited and did not have enough data to do a proper alignment.

ALEPH has a vertex detector that is composed of two–sided silicon microstrips enabling them to measure three–dimensional hits and form three–dimensional impact parameters. The innermost layer of silicon is at an average radius of 6.3 cm. ALEPH has enough data to double–tag and they measure $\epsilon_b = 26\%$, $\Pi_b = 96\%$ and $R_b = 0.2192 \pm 0.0037$.[20] They are systematics limited.

DELPHI does its vertexing with a vertex detector made of silicon microstrips. Only the $r\phi$ coordinate can be measured with any accuracy ($\sigma_{\rm VD} = 11\,\mu$m). They use a slightly different approach, determining τ_B from the two–dimensional impact parameter distribution of high–p_t hadrons. By comparing the measured τ_B to the τ_B determined from Monte Carlo data with different R_b, they measure $R_b = 0.222 \pm 0.037$.[25] The error is dominated by the world average $\sigma(\tau_B)$.

OPAL had a jet–cell drift chamber vertex detector with single wire resolution in $r\phi$ of 50 μm. They compared the forward (b > 0) multiplicity to the backward (b < 0)

multiplicity and made a fit to determine $R_b = 0.222 \pm 0.011$.[35] In May 1991, OPAL installed a two–layer silicon microstrip vertex detector with intrinsic $\sigma(r\phi) \simeq 6\,\mu$m.[40] With this they have done a mixed tag using the forward multiplicity and high–p_t leptons to measure ϵ_b and get $R_b = 0.222 \pm 0.013$.[37] This result is statistics limited because of the semi–leptonic branching ratio.

SLD is described in detail in the next chapter. SLD has submitted two conference reports: The first report[38] uses two methods: a two–dimensional impact parameter technique ($\epsilon_b = 0.71$, $\Pi_b = 0.74$) and a displaced two–prong vertex technique ($\epsilon_b = 0.58$, $\Pi_b = 0.77$) on a sample of about 10k Z^0 events. The former method gives $R_b = 0.214 \pm 0.027$ while the latter method gives $R_b = 0.204 \pm 0.032$. The second report[39] uses the two–dimensional impact parameter technique on a sample of about 27k Z^0 events. It gives $R_b = 0.235 \pm 0.019$. In all cases the systematic error (which is conservative) is the limiting factor.

1.3.2 Determination of Δ_{bV}

The most recent combined LEP measurement is $R_b = 0.2200 \pm 0.0027$. This value is consistent with the MSM and $m_t \sim 160$ GeV/c^2.[4] Blondel *et al.*[16] have used an older combined LEP measurement of $R_b = 0.2168 \pm 0.0067$ to derive:

$$\Delta_{bV} = -0.011 \pm 0.039_{(\mathrm{exp})} \pm 0.001_{(m_b)} \pm 0.0004_{(\alpha_s)} \tag{1.26}$$

They then derive the upper bound on m_t using the CDF physical limit of $m_t > 91$ GeV/c^2:

$$\Delta_{bV} > -0.078 \qquad (95\%\ \text{c.l.}) \tag{1.27}$$

$$m_t < 360\ \text{GeV}/c^2 \qquad (95\%\ \text{c.l.}) \tag{1.28}$$

The central value corresponds to $m_t = 160$ GeV/c^2.

1.4 Preview of Analysis Technique

B mesons have relatively long lifetimes. The decay daughters of B mesons have, on average, large impact parameters with respect to the Z^0 decay (primary) vertex. By

Collaboration	Sample Size	Method	R_b
ALEPH [19]	25k	leptons	0.220 ± 0.029
ALEPH [20]	680k	3–dim b	0.2192 ± 0.0037
ALEPH [21]	440k	event shape/leptons	0.228 ± 0.007
DELPHI [22]	18k	event shape	0.209 ± 0.043
DELPHI [23]	120k	leptons	$(0.0221 \pm 0.015)/\mathrm{Br}^b_{\mathrm{s.l.}}$
DELPHI [24]	120k	event shape	0.219 ± 0.024
DELPHI [25]	120k	τ_B	$0.222^{+0.037}_{-0.035}$
DELPHI [26]	120k	neural net	0.232 ± 0.018
L3 [27]	18k	leptons	0.204 ± 0.020
L3 [28]	115k	leptons	$(385 \pm 23)/\Gamma_{\mathrm{had}}$
L3 [29]	238k	neural net	0.222 ± 0.008
MarkII [30]	0.4k	leptons	$0.23^{+0.11}_{-0.09}$
MarkII [31]	0.2k	2–dim b	0.251 ± 0.057
OPAL [32]	133k	lepton $P \times P_t$	0.193 ± 0.024
OPAL [33]	136k	leptons	0.226 ± 0.020
OPAL [34]	450k	leptons	0.220 ± 0.013
OPAL [35]	130k	2–dim b	0.222 ± 0.011
OPAL [36]	450k	leptons	0.222 ± 0.013
OPAL [37]	450k	2–dim b & leptons	0.218 ± 0.012
SLD [38]	10k	2–dim b	0.214 ± 0.027
SLD [38]	10k	displaced vertex	0.204 ± 0.032
SLD [39]	27k	2–dim b	0.235 ± 0.019

Table 1.2: Summary of previous R_b measurements.

counting the number of well–measured tracks in each event that miss the primary vertex by a significant amount, it is possible to isolate those events that contain B mesons. This technique is very difficult to employ in a detector where the innermost sensitive element is far from the primary vertex. The SLD vertex detector begins at 2.9 cm from the beamline and has true three–dimensional pixels with a typical precision of 5 μm in each coordinate.[45] The vertex detector, in combination with the SLD's central drift chamber, allows the majority of tracks in a Z^0 decay to be reconstructed with high accuracy.

Despite the precise measurements already done at LEP, there are several reasons for doing this analysis at SLC. The systematic errors at the LEP experiments are different from those at the SLD. The SLD vertex detector is more precise than any

of the vertex detectors currently in use and should give the lowest systematic error, given similar amounts of data. As demonstrated by the ALEPH group, the three–dimensional impact parameter technique provides the most accurate measurement of R_b; this analysis is the first use of three–dimensional impact parameters at the SLD. Over the next few years, the SLD will record several hundred thousand Z^0 decays. The SLD collaboration will then be able to double–tag and should measure R_b to better than 1%, limited by systematic errors.

Chapter 2

The Experiment

The SLD is the center of a large complex experiment requiring the hard work of hundreds of people. Without discussing the many details of the experiment, this chapter will give detailed explanations of the hardware that is most important to this analysis. The components that are not as important for this analysis will also be briefly discussed.

2.1 Accelerator

The SLAC Linear Collider (SLC) is a novel configuration for a colliding beam accelerator. Instead of the typical circular beam path with frequent down–time for "fills" and beam cooling, SLC generates, cools and accelerates both electrons and positrons on a cycle–by–cycle basis with a cycling frequency of 120 Hz. Two bunches of electrons are produced at an electron source, usually referred to as the "electron gun." After the transverse size of the bunches is reduced in a damping ring, the bunches are both accelerated along the two–mile linear portion of the accelerator (the "linac"). Part of the way down, the trailing bunch is kicked out of the accelerator and collides with a stationary target. From this collision, positrons are collected and returned to the start of the accelerator. The positron bunch is damped, then it is accelerated in between the next pair of electron bunches. The positron intensity usually is somewhat lower than the electron intensity due to limited positron yield and losses in the

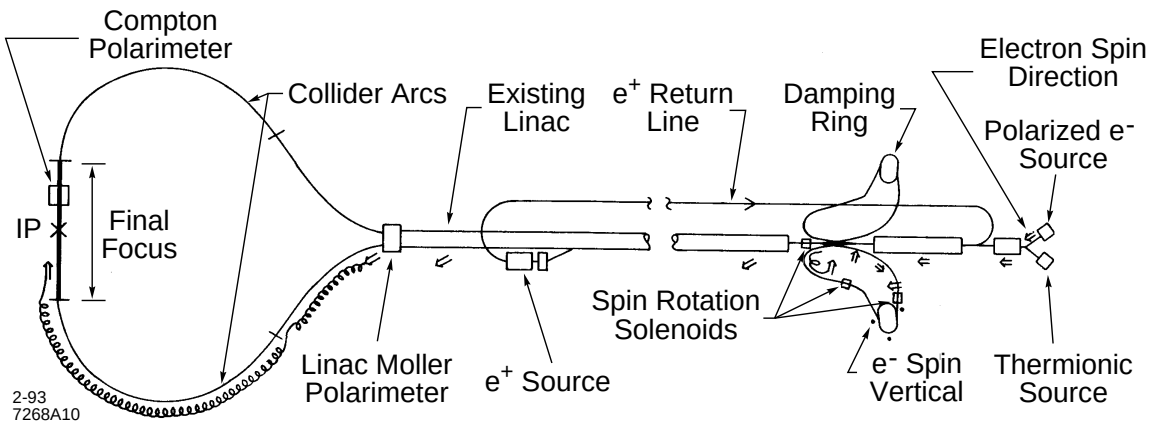

Figure 2.1: Layout of the SLC (not to scale).

return path. During the 1992 run, SLC's positron yield peaked at 1.25 (per electron incident on the target) and that yield could be maintained above unity "with little effort."[42]

At the end of the linac, the positron and electron bunches are sent into different arcs: positrons to the right, electrons to the left. These arcs, roughly eggbeater shaped, bend the particles' trajectories — but do not otherwise accelerate them — such that at the end of the arcs the two beams are directed exactly at each other. The particles collide with their center–of–mass at rest with respect to the Earth. Particles that do not interact continue past the interaction point and are directed into beam dumps.

For this run, the SLC was upgraded to use longitudinally polarized electrons. These electrons are produced by photoemission from a gallium arsenide photocathode.[44] A spin rotation system rotates the electron spins into the vertical direction for storage in the electron damping ring and adjusts the spin direction upon extraction from the ring to achieve longitudinal polarization at the SLC interaction point. The beam helicity is changed randomly on a cycle–by–cycle basis.

The longitudinal polarization ($\mathcal{P}_e$) is measured by a Compton scattering polarimeter located about 30 m downstream of the interaction point (IP). The polarization of the electron beam at the IP was on average $22.4 \pm 0.7\%$ (syst).[72]

During the 1992 data run, SLC routinely ran with an intensity of 3×10^{10} particles

per bunch and average beam spot sizes of $\sim 2\,\mu\mathrm{m} \times 2\,\mu\mathrm{m}$ at the IP.[42] These parameters correspond to event rates of about 10—20 Z^0's per hour; the peak rate was 28 Z^0's per hour. The center–of–mass energy was slightly off the Z^0 peak, $\sqrt{s} = 91.55$ GeV.

2.2 Detector

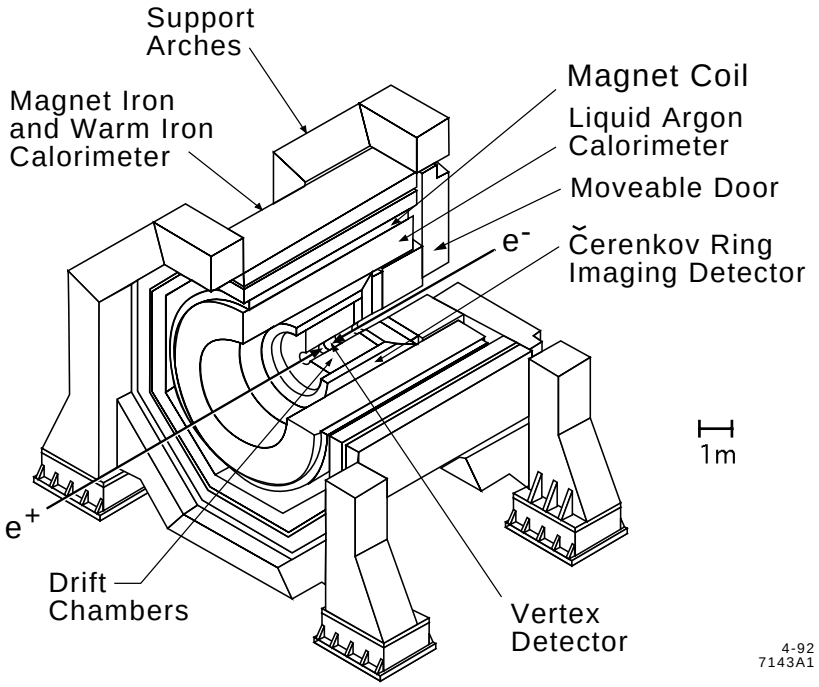

Figure 2.2: Cutaway view of the SLD.

The SLD is a large 4π detector located at SLC's interaction point. Figures 2.2 and 2.3[43] show different views of the SLD. The detector provides four types of measurements: tracking, calorimetry, particle identification and luminosity monitoring. The following discussion emphasizes tracking, as it is most relevant to this analysis.

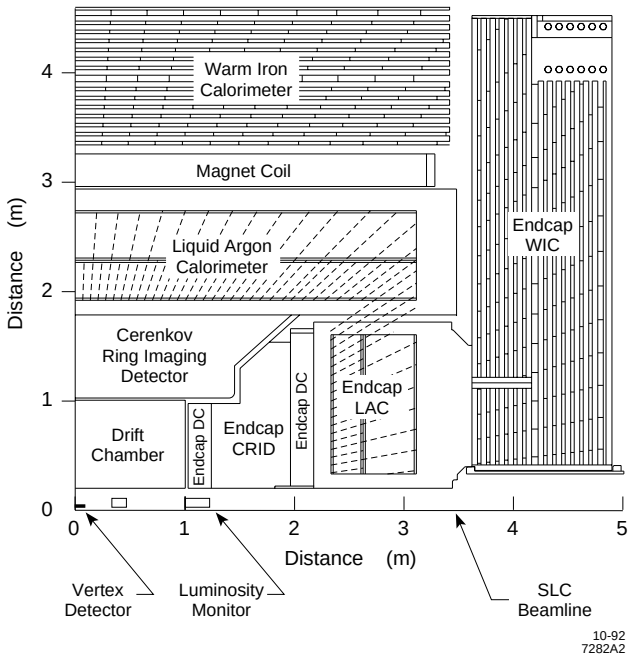

Figure 2.3: Quadrant view of the SLD.

2.2.1 Tracking

Track reconstruction and momentum determination are done primarily using standard technology drift chambers. A conventional solenoidal magnet produces a 0.6 Tesla axial magnetic field. A novel vertex detector, based on charge–coupled devices (CCDs), allows for accurate extrapolation of the tracks near the interaction point.

2.2.1.1 Vertex Detector

In order to accurately measure the position of charged particles near the interaction point, the SLD has a silicon CCD vertex detector (VXD). The VXD is designed to obtain a one–hit precision of $5\,\mu$m and a two–hit vertex resolution of $40\,\mu$m. The innermost layer of the VXD is at a radius of 29.5 mm from the SLC beamline, hence little precision is lost when extrapolating to the IP.

Each CCD has an active area of 9 mm $\times$ 13 mm and is divided into 222,530 pixels, each pixel being $22\,\mu$m $\times$ $22\,\mu$m. The depletion depth is $8\,\mu$m. When a minimum ionizing particle crosses a CCD at roughly normal incidence, it deposits a charge of

1300 electrons (on average), typically with 80% of the charge in one or two pixels.

The price paid for the high precision device is twofold: (1) The CCDs and their support structure present a large block of material ($L/X_0 = 5.8\%$) in front of the main drift chamber. Multiple scattering in the VXD is more significant than multiple scattering in the drift chambers since track reconstruction begins with the innermost layers of the drift chambers. The large multiple scattering occurs despite the fact that the silicon wafers used for the CCDs were thinned from 580 μm (the industry standard) to 200 μm. (2) The time necessary to read out the VXD is large compared to every other time in the readout stream as well as to the cycling time of the SLC. This occurs because all the pixels on a CCD are read out serially.

To construct the VXD, eight CCDs are wire bonded to an alumina mother card. This assembly is known as a "ladder." The CCDs are mounted on alternating sides of the ladder such that there is no gap in active area along the length of the ladder. The total active area per ladder is 9 mm $\times$ 100 mm. The ladders are then mounted on a support structure — machined from a single block of instrument grade beryllium — which arranges the ladders into four concentric barrels. The two inner barrels are made of thirteen ladders each while the two outer barrels are made of seventeen ladders each. The barrels are staggered and paired up into two logical layers such that there is no gap in azimuthal coverage. (See figures 2.4 and 2.5.) Any charged particle traversing the VXD should deposit charge in at least two CCDs allowing us to reconstruct its path. A significant fraction of tracks ($\sim 30\%$) will deposit charge in three CCDs thus allowing us to confirm the VXD internal alignment. The overall solid angle covered by the VXD is 75% of 4π. There are a total of 60 ladders, consisting of 480 CCDs or 106,814,400 pixels total.

It is interesting to compare SLD's VXD with the best vertex detector at the LEP experiments, ALEPH's VDET.[41] The VDET uses double–sided silicon microstrips to provide full x, y and z information about tracks. It has two layers with the microstrip assemblies ("faces") tilted away from the normal to allow each layer to be shingled to provide full azimuthal coverage with $\sim 5\%$ overlap. The beampipe has an outer radius of 5.5 cm and the two layers of detectors have average radii of 6.3 cm and 10.7 cm. The strip pitch is 25 μm and the readout pitch is 100 μm. The strips on the

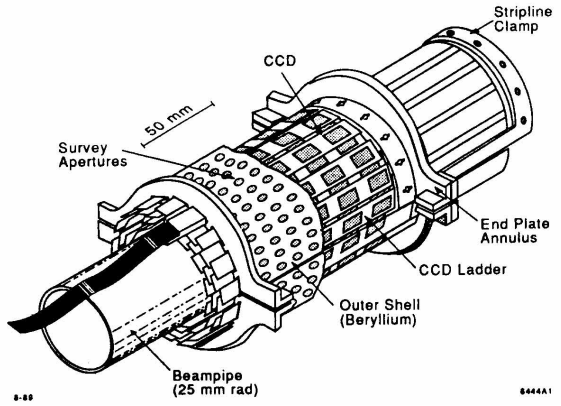

Figure 2.4: Artist's drawing of the VXD.

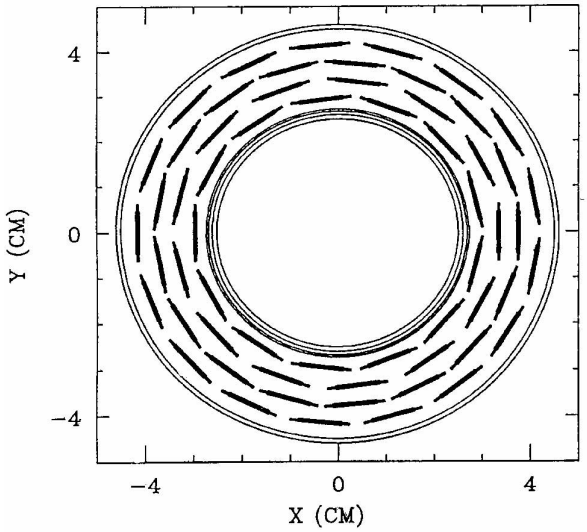

Figure 2.5: Cross–section of the VXD.

z–side are 51.2 mm long while the strips on the ϕ–side are twice as long. Figure 2.6 is a schematic diagram of this detector drawn to the same scale as figure 2.5. Note that the VXD's active components can fit inside ALEPH's beampipe.

In order to minimize dark current and electronic noise, the entire VXD is kept at $-80°$C. Since the pixels are "dumb"* the entire VXD only dissipates 12W. This heat can easily be removed by flowing across the VXD nitrogen gas that has just boiled off

* *Smart* devices contain logic to determine if they contain significant data and hence must be read out. *Dumb* devices must be read out every time, but contain no extraneous logic, hence the power usage is minimal.

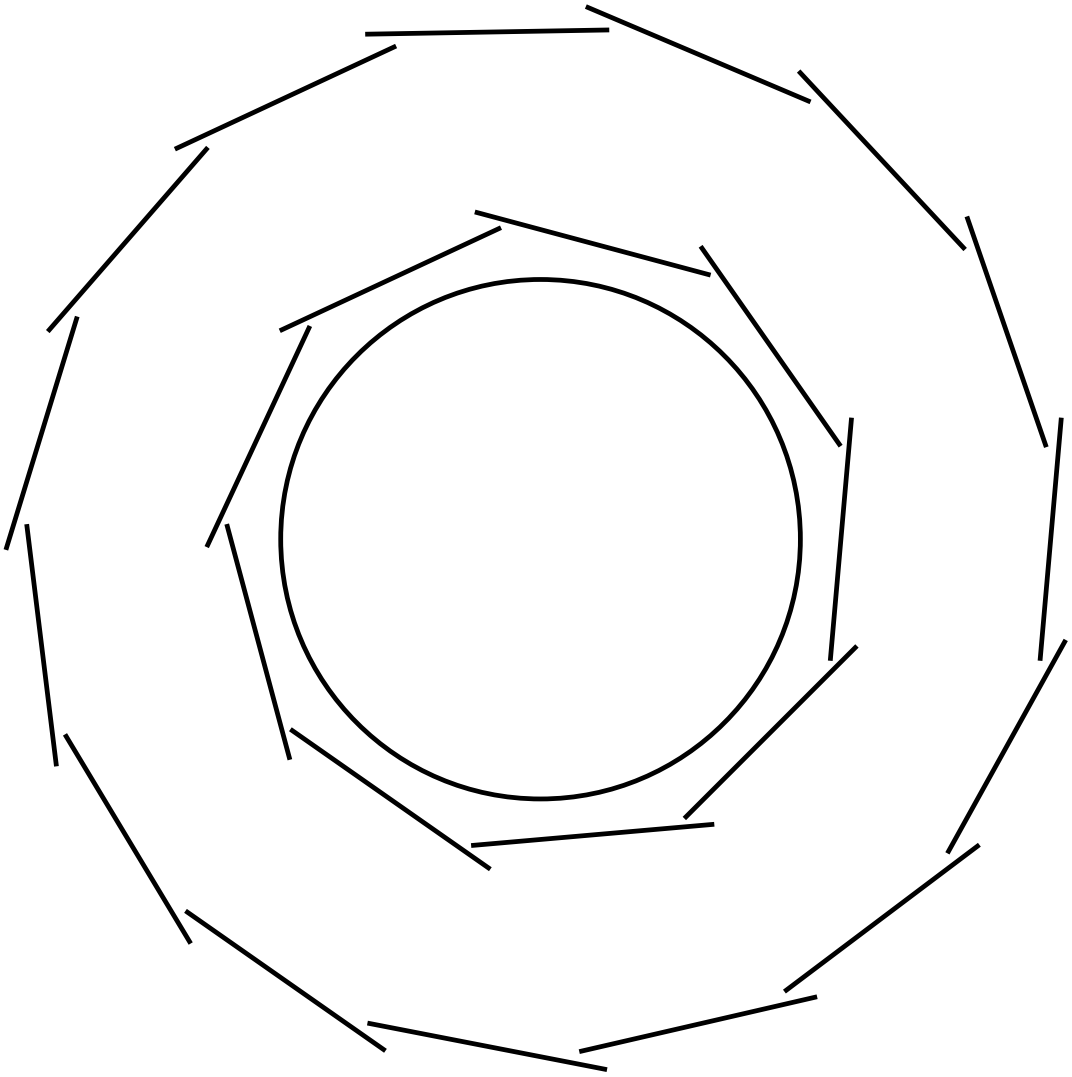

Figure 2.6: Schematic cross–section of ALEPH's new vertex detector.

liquid nitrogen. A polyurethane foam cryostat surrounds the VXD, insulating other portions of SLD from the boil–off nitrogen. Multiple scattering from the nitrogen and cryostat is essentially negligible.

It would be impossible to have a readout line for each pixel. The CCDs are designed to be read out in a serial fashion, using x and y clock pulses to order the pixel outputs over a single coaxial cable. This readout scheme reduces the number of necessary readout lines to 480, but reading out $\sim 220,000$ pixels through a single cable

takes roughly 160 ms, equivalent to 19 beam crossings at 120 Hz. Pixels with negligible charge deposition are suppressed in the data acquisition electronics, typically leaving only 0.01% of the pixels ($\sim 10k$).

For this run there were 2 dead ladders, 1 inefficient ladder, 2 dead CCDs and 3 inefficient CCDs. The remaining 94% of the VXD is fully functional and reliable.[46] The xy and rZ uncertainties at high p_t can be extrapolated from the miss distances of muons from $Z^0 \rightarrow \mu^+\mu^-$ events (see fig. 2.7):[47]

$$\sigma_{xy} = 15.7\,\mu\text{m} \tag{2.1}$$

$$\sigma_{rZ} = 46.5\,\mu\text{m} \tag{2.2}$$

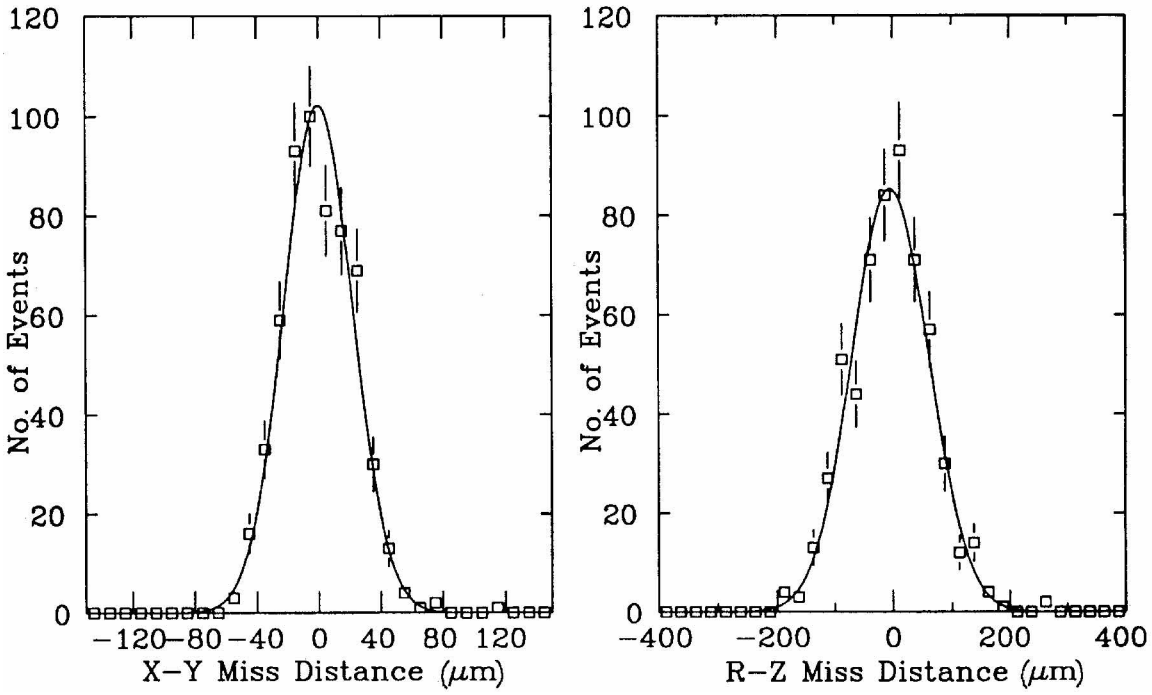

Figure 2.7: Muon–pair miss distances.

2.2.1.2 Drift Chambers

Tracking in the central region is done by the central drift chamber (CDC). The forward and backward regions are instrumented with endcap drift chambers (ECDCs). All

of the chambers operate with the same technology. The endcap drift chambers were still being commissioned during this run, thus this analysis does not use any data from them. Their absence has little impact here as there is little overlap between the VXD and the ECDCs.

The CDC occupies the volume from 20 to 100 cm in radius and -100 to $+100$ cm in z around the interaction point. It is designed to provide drift resolution of $\lesssim 100\,\mu$m which translates to a momentum resolution of $\sigma_p/p \leq 1.3\times10^{-3}\cdot p$ where p is in GeV/c. The measured drift resolution is shown in figure 2.9. The CDC is optimized to have minimum radiation thickness while still providing this resolution. The thicknesses are: inner wall, 0.009 X_0; wires, 0.020 X_0; gas, 0.006 X_0; outer wall, 0.018 X_0. The total thickness is only 0.053 X_0. Note that, unlike the VXD, much of the CDC material comes after the tracking measurements are made.

There are ten concentric superlayers, each with eight sense wires for a total of eighty layers. Four of the superlayers are axial and six are stereo, with a stereo angle of ±41 mrad (see table 2.1). The cell width at the middle of each layer is ~ 59 mm which leads to a total number of 640 cells. Both sides of all sense wires are instrumented so that the z position can be determined by charge division ($\sigma(z) \simeq 1.8$ mm). The small–angle stereo layers provide a precise measurement of the polar angle ($\sigma(\theta) \simeq 2$ mrad). Azimuthal angle can be measured to ~ 1 mrad.

The design of a basic cell is shown in figure 2.8.[43] Twenty–two guard wires and two dummy sense wires shape the electrostatic field surrounding the (instrumented) sense wires. Twenty–seven field wires complete the field shaping for the entire cell. The finite length of showers generated by primary ionization creates a "dead band" surrounding each track. Because the drift cell is left–right ambiguous there is also a dead band on the side opposite to the track, reflected over the sense wires. If the sense wires were aligned radially this reflected dead band would cause a significant amount of tracking inefficiency. By tilting the cell 5° from the radial direction this reflected dead band is tilted 10° from radial and the tracking inefficiency is greatly reduced.

The field and guard wires are 152 μm diameter copper–beryllium strung at 400 g tension. The sense wires (instrumented and dummy) are 25 μm diameter tungsten

Superlayer	Orientation	N_{cells}	R_{center} (mm)
1	A	28	261.80
2	U	36	339.50
3	V	44	413.50
4	A	52	487.50
5	U	60	563.50
6	V	68	637.50
7	A	76	712.50
8	U	84	788.01
9	V	92	862.50
10	A	100	937.50
		total=640	

Table 2.1: Arrangement of layers in the CDC.
Key: A=axial, U=positive stereo, V=negative stereo.

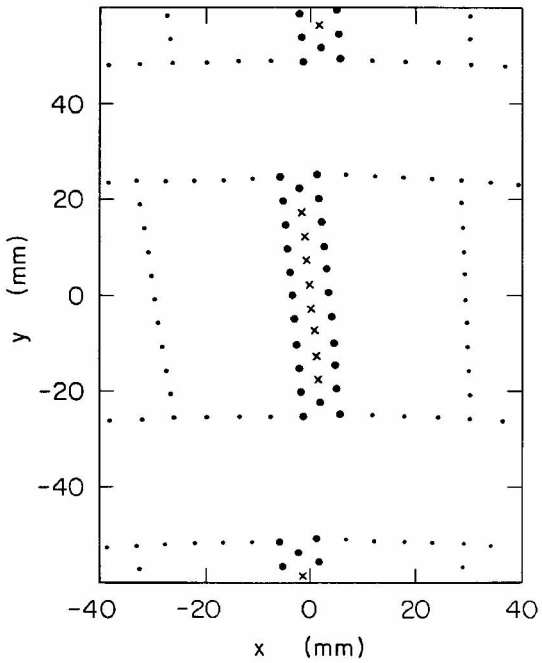

Figure 2.8: Design of the CDC basic cell.
Key: × = sense wire, • = guard wire and · = field wire.

strung at 100 g tension and they have a resistance of 300 Ω. The field wires are strung individually, but the sense and guard wires are first located in a plastic plug, then strung as a unit. Stringing as a unit not only simplifies construction, but it also generates a more reliable relative placement of the sense and guard wires in the cell. Approximately two hundred different voltages are required, ranging from ground to −7 kV. The average drift field is 0.13 kV/mm.

The gas used in the drift chambers is a mixture of 74.7% CO_2, 21% Ar, 4% isobutane and 0.3% H_2O maintained to ±0.15%. Contamination of oxygen is kept below 20 ppm and both the pressure (1 atm) and temperature (20°C) are closely tracked. This gas mixture has a drift speed of $\sim 9\,\mu$m/ns at our electric field value and is in a linear regime for easier corrections. The largest drift in a cell is ∼ 30 mm hence signals will be spread out over 3.3 μs. A typical track leaves sixteen primary electrons which are amplified to a signal of 3×10^6 electrons.[43, sec. 5.2]

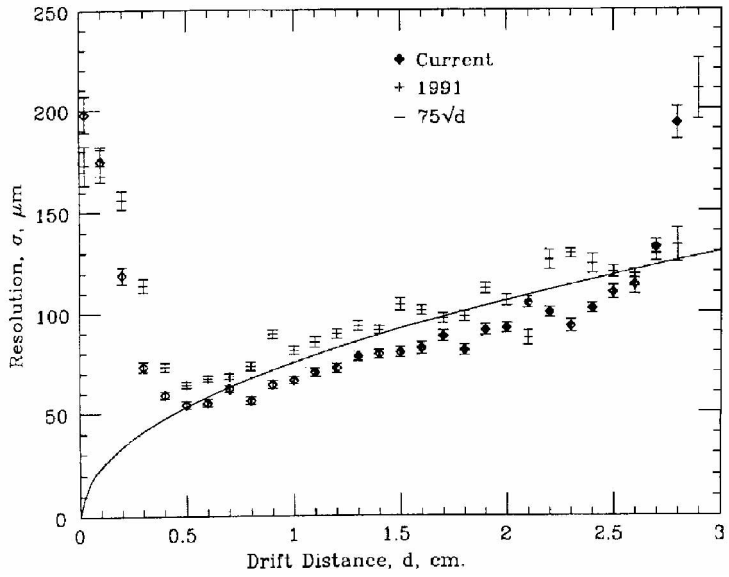

Figure 2.9: CDC point resolution as a function of drift distance.

Figure 2.9[48] shows the local resolution† of hits found on CDC track segments near the radial direction. The analysis done with 1992 data agrees well with the curve expected from diffusion. The increases near the cell boundaries are also expected. In

† Residual between measured hit and fitted track segment.

the linear region ($0.5\,\mathrm{cm} < d < 2.5\,\mathrm{cm}$) the average local resolution is $68\,\mu\mathrm{m}$.

2.2.2 Particle Identification

The SLD uses many subsystems for particle identification. For hadrons, particle identification is done primarily in the Čerenkov Ring Imaging Detectors (CRIDs). The CRIDs are also essential for identifying electrons and muons at low momentum. At high momentum, electrons are identified by a calorimetric analysis of their shower profile, and muons are identified by their large penetration depth.

The technology used in the CRIDs posed a great engineering challenge during the design and construction phases of the SLD. Two radiators generate Čerenkov photons and a set of mirrors guide and focus them to the same set of drift boxes. Inside a drift box the photons are photoconverted, and the resulting electrons drift to a multiwire proportional chamber (MWPC). (See figures 2.10 and 2.11.) In this manner the ring of Čerenkov photons can be reconstructed, and — given the momentum — the mass of the particle can be determined. The design goal is π/K/p separation up to 30 GeV/c and e/π separation up to 6 GeV/c.

One of the Čerenkov radiators is a thin (10 mm) tray of liquid C_6F_{14}. The high index of refraction of the liquid ($n = 1.277$ at 6.5 eV) allows for π/K/p separation from $\sim$0.2 to 6 GeV/c. Since the drift box is close to the liquid radiator, no focusing is needed. The other radiator is a gaseous mixture of 70% C_5F_{12} and 30% N_2 which occupies $\sim$ 45 cm on the other side of the drift box.[‡] With an index of refraction only slightly above one, the gas radiator provides for high momentum particle separation (2.6 to $\sim$30 GeV/c). Spherical mirrors reflect and focus the cone of Čerenkov photons generated in the gas radiator, forming a ring on the far side of the drift box. Gas rings typically have a radius of 2.5 cm, while liquid rings are typically 17 cm in radius and are spread out over several drift boxes. Both types of rings typically have ten detected photoelectrons.

Both sides of the drift boxes and one side of the liquid radiator trays have windows made of fused silica quartz which is almost transparent to the ultra–violet Čerenkov

[‡] This gas also occupies the gap between the liquid radiator and the drift box, but this fact is not significant for data reconstruction.

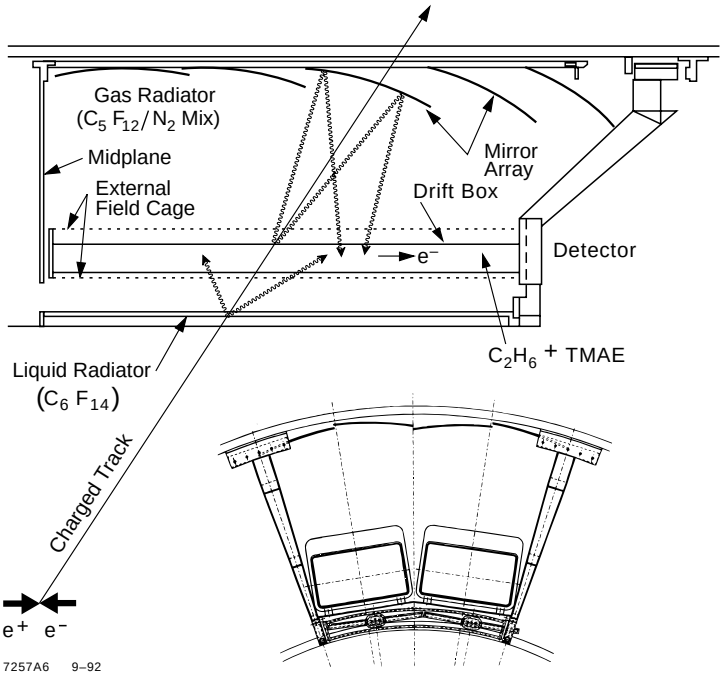

Figure 2.10: Schematic diagram of the barrel CRID.

photons. A fine cage of wires completely surrounding the drift boxes generates the electrostatic drift field. A coarse cage of wires surrounds the fine cage in order to reduce edge effects. High purity ethane flows through the drift boxes with a 0.1% admixture of TMAE to carry out the photoconversion. Oxygen and water, the main contaminants, are kept below 0.5 ppm and 5 ppm respectively by a complicated filtration system. During the run, it was discovered that the ethane supply was contaminated with sulfur. When a nickel filter was introduced to remove this contaminant, the drift velocity dropped (see fig. 2.12). It is believed that this filter is introducing a 0.25% admixture of CO_2 into the ethane.[50]

A single plane MWPC at the end of the drift boxes detects single electrons. The wire number gives one direction, the timing of the signal gives another and charge division along the wire provides the third. The anode wires are 7 μm diameter resistive carbon fibers with a pitch of 3.175 mm.

An extensive Xenon flashlamp/fiber optic system calibrates the drift boxes. The flashlamp is triggered on every beam crossing, and fiber optics distribute the resulting

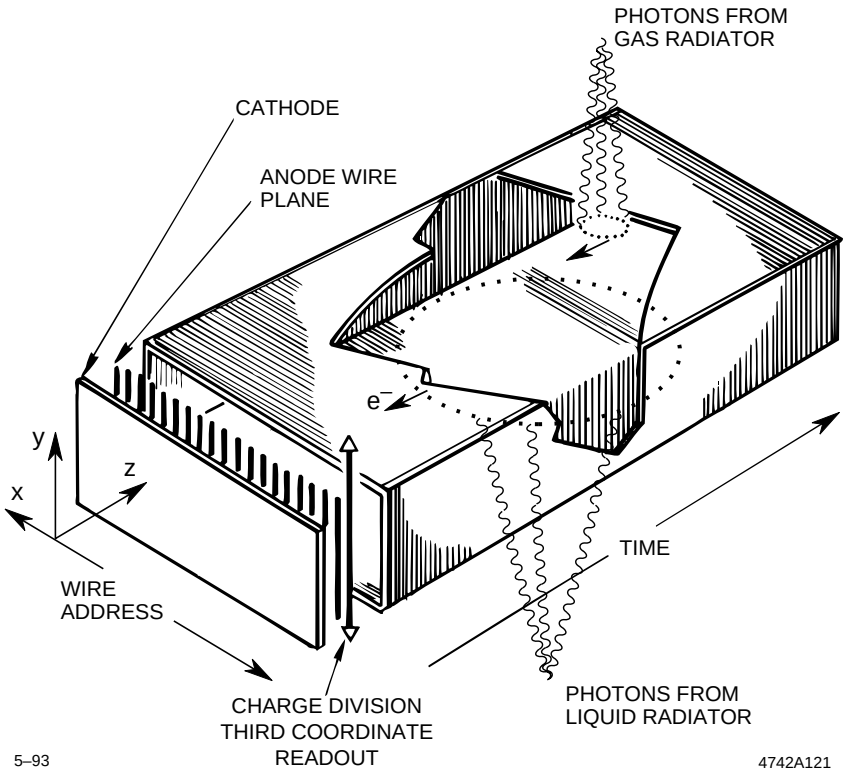

Figure 2.11: CRID readout technology.

UV light to various fiducial points on each drift box. Fibers normal to the drift box at several drift distances monitor the drift velocity. Fibers inclined 45° from normal calibrate the charge division. These and other fibers measure electron trajectories over the entire drift box. Although the flashlamp intensity is set such that a photoelectron is generated only 10% of the time at each fiducial point, calibration pulses result in about 5% of the CRID data in events written to tape. The large volume of data from calibration pulses is necessitated by the extensive variation in drift velocity (see figure 2.12) and by the need for well–calibrated electron trajectories. The drift velocity variations could cause position errors of 20 mm, compared to the design uncertainty of 1 mm.[49]

The endcap CRID was not implemented for this run, but will be implemented for future runs. It does not contain a liquid radiator, but the gas radiator and its associated optics are the identical to the barrel CRID.

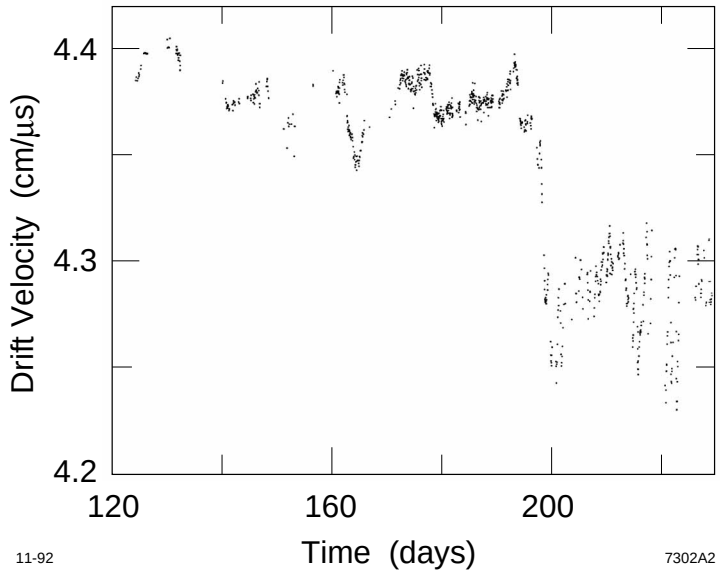

Figure 2.12: Measured drift velocity in the barrel CRID over the 1992 data run.

Results from CRID data taken during the 1992 run are shown in figure 2.13.[50] The top plot shows the Čerenkov angle as a function of momentum from liquid radiator rings. The π, K and p bands are clearly visible. The bottom plots are momentum slices from the top plot with the π, K and p peaks indicated. Note that the 1.0 GeV/c slice is below threshold for protons.

2.2.3 Calorimetry

The SLD's calorimetry system is a hybrid design which combines high–resolution lead and liquid argon and full ($\sim 7\lambda$) hadronic calorimetry without necessitating an overly large (*i.e.* expensive) magnet coil. The calorimeter inside the magnet is the Liquid Argon Calorimeter (LAC), and the calorimeter outside the magnet is the Warm Iron Calorimeter (WIC). The luminosity monitoring system (see section 2.2.4) serves as a calorimeter at very small angles.

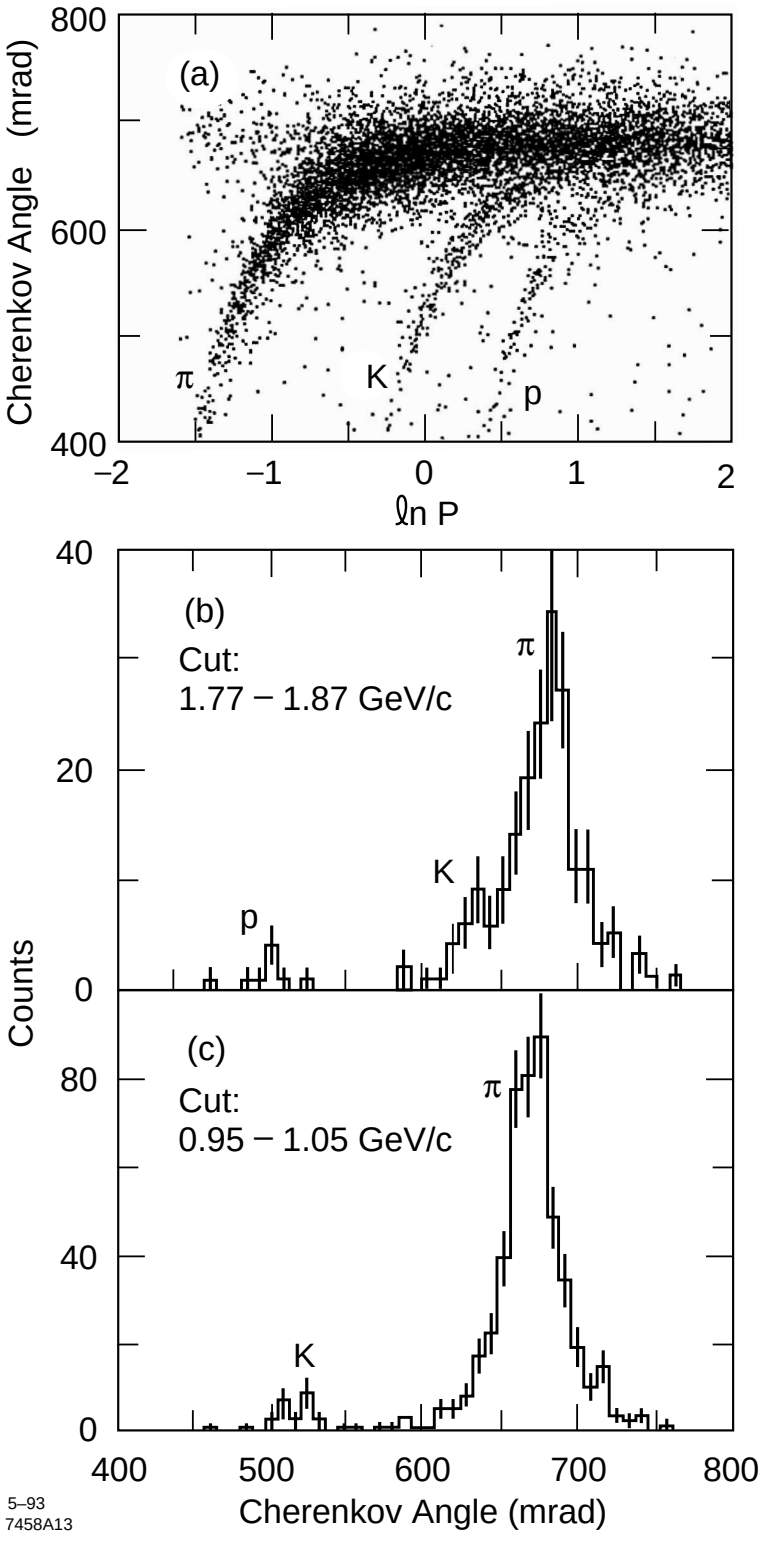

Figure 2.13: Results from CRID during 1992 data run.

2.2.3.1 LAC

The LAC is a sampling calorimeter consisting of planes of lead (as an absorber) separated by liquid argon. The liquid argon collects charges deposited by charged particles generated in the shower. The total collected charge is proportional to the energy of the incident particle. The sampling fraction per layer is constant over the entire LAC. A small global correction must be made for the purity of the argon, but interchannel calibration depends solely on external electronics and hence should be repeatable to within 0.5%. Liquid argon was chosen for this reason and since, unlike scintillators, it is not susceptible to radiation damage.

The LAC was constructed in three distinct cryostats: barrel and two endcaps, but it is operated as a single unit. Each piece is subdivided into four longitudinal sections. The two inner sections are finely segmented ($\Delta\theta = 36$ mrad and $\Delta\phi = 33$ mrad) into projective towers in the transverse direction for electromagnetic (EM) calorimetry. Two outer sections are coarsely segmented for hadronic (HAD) calorimetry (2×2 EM towers per HAD tower).[51]

In the electromagnetic layers, the lead sheets are 2.0 mm thick, while in the hadronic layers they are 6.0 mm thick. The argon gap is 2.75 mm for all layers. A unit cell consists of a plane of lead at ground, an argon gap, a plane of lead at high voltage and another argon gap. The arrangement of layers is shown in table 2.2.

longitudinal division	cells	X_0	λ	thickness (in mm)
EM 1	8	6.03		
EM 2	20	15.08		
subtotal	28	21.13	0.84	266
HAD 1	13	—	1.00	
HAD 2	13	—	1.00	
subtotal	26	—	2.00	455
total	54	—	2.84	721

Table 2.2: Arrangement of layers in the Liquid Argon Calorimeter.

With over 21 radiation lengths instrumented in the the electromagnetic section, showers up to 50 GeV are well contained. The resolution of electromagnetic showers

is $\sigma_E/E = 15\%/\sqrt{E}$ as measured by Bhabha electrons. (See figure 2.14.) The hadronic section adds an additional 2λ of instrumented material inside the magnet coil. Combined with the EM section, about 85% of typical hadronic showers should be contained within the LAC.

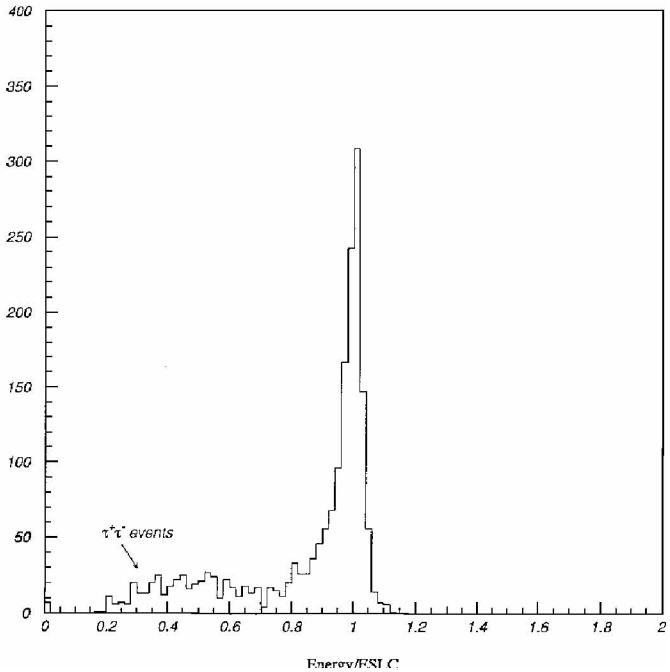

Figure 2.14: Energy of Bhabha electron showers in the barrel LAC, normalized by the SLC beam energy. Tail on low energy side comes from $Z^0 \rightarrow \tau^+\tau^-$ background events.

2.2.3.2 LAC Energy Scale

The standard energy scale for the LAC is used for minimum ionizing particles (MIPs) such as muons. In the electromagnetic section, 1 ADC count corresponds to 2.04 MeV, while in the hadronic section, 1 ADC count corresponds to 5.41 MeV. Electrons and hadrons are less efficient at depositing energy visible to the LAC by factors of 0.7 and 0.5 respectively. Thus, if an energy cluster is determined in later processing to be from an electron or from a hadron, its energy is corrected accordingly. (See table 2.3.[53])

Energy Scale	ADC counts per GeV	
	Electromagnetic	Hadronic
MIP	489	185
$e^{\pm}$	342	130
hadron	245	93

Table 2.3: LAC energy scales.

2.2.3.3 Warm Iron Calorimeter

The WIC is a coarse calorimeter, a muon detector and the magnet return. Hadronic showers are primarily measured in the LAC — only the tail of the showers (about 15%) leave the LAC. The showers will loose some energy in the 0.5λ of the magnet, but the rest of the shower will be measured by the WIC. Cathode pads read out energy deposition while Iarocci tubes crossed with cathode strips record muon hits.

The WIC is composed of alternating layers of iron and streamer tubes/readout sheets. There are fourteen layers of iron plates, each 5 cm thick. The iron is magnetized in the direction parallel to the wires such that some momentum measurement can be made. The streamer tubes are made of graphite–coated extruded PVC plastic. Individual channels are 9 mm $\times$ 9 mm and have a 100 μm diameter beryllium–copper wire held in the center. Each unit holds eight tubes which are ganged together. The gas used in the streamer tubes is 88% CO_2, 9.5% isobutane and 2.5% argon.[54]

Electrode sheets located above and below the streamer tubes are used for readout. The sheets are made from copper–clad fiberglass cut to the desired pattern. Strips run parallel to the wires, and rectangular pads continue the projective tower geometry of the hadronic layers of the LAC ($\Delta\theta$ = 72 mrad and $\Delta\phi$ = 66 mrad). On layers seven and fourteen, an extra layer of streamer tubes and two layers of transverse strips (perpendicular to the wires) provide for two–dimensional readout. The pads are ganged together into two depth segments, read out as an analog signal and later digitized. There are approximately 8600 pad channels. The strips are read out individually for a total of $\sim 80,000$ channels.

The WIC covers a solid angle of 99.2% of 4π. The design resolution for hadronic

showers in the WIC (alone) is $\sigma_E/E = 80\%/\sqrt{E}$. Combined with the LAC information, hadronic showers are measured to $\sigma_E/E = 64\%/\sqrt{E}$.[55]

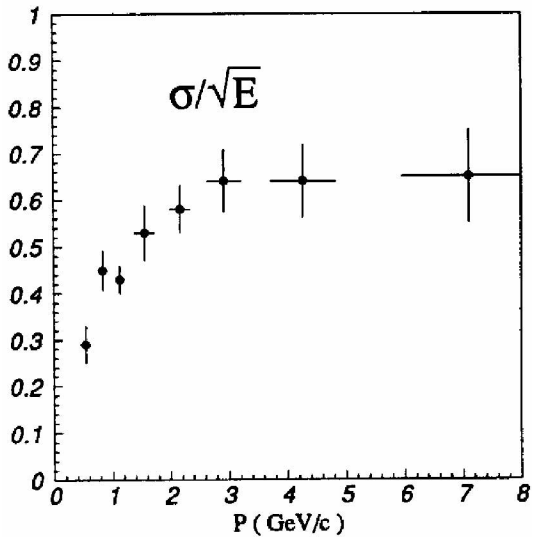

Figure 2.15: Energy resolution of hadrons in the SLD calorimetry system.

2.2.3.4 Medium Angle Silicon Calorimeter

The angular region below the endcap LAC and above the luminosity monitor (see section 2.2.4) is covered by the Medium Angle Silicon Calorimeter (MASiC). The MASiC is a silicon–tungsten sampling calorimeter with angular coverage of $68 < \theta < 190$ mrad. The MASiC has 10 sampling layers each of which is $1.74X_0$ deep. The layers are ganged together into two sections: EM1 is the first three layers ($5.22X_0$) and EM2 is the other seven ($12.18X_0$). The tower structure is approximately projective and fits in with the LAC and LMSAT towers. Each tower covers ~ 36 mrad in θ and $11.25°$ ($22.5°$ for two inner rings) in ϕ.[56]

2.2.4 Luminosity Monitor

The luminosity monitor/small angle tagger (LMSAT), a specialized calorimeter, provides a luminosity measurement independent of accelerator parameters. The LMSAT is a sampling calorimeter with silicon detectors and tungsten radiators. Like the

SLD's other calorimeters, it has an approximate projective tower geometry with each tower covering ~ 9 mrad in θ and 11.25° (22.5° for inner two rings) in ϕ. The angular coverage is $28 < \theta < 65$ mrad. The readouts for each tower are ganged together into two longitudinal sections. Section EM1 is $5.5X_0$ thick and section EM2 is $15.6X_0$ thick, for a total instrumented depth in excess of $21X_0$. The LMSAT contains $> 99.5\%$ of a 45 GeV electromagnetic shower with energy resolution of 3%.

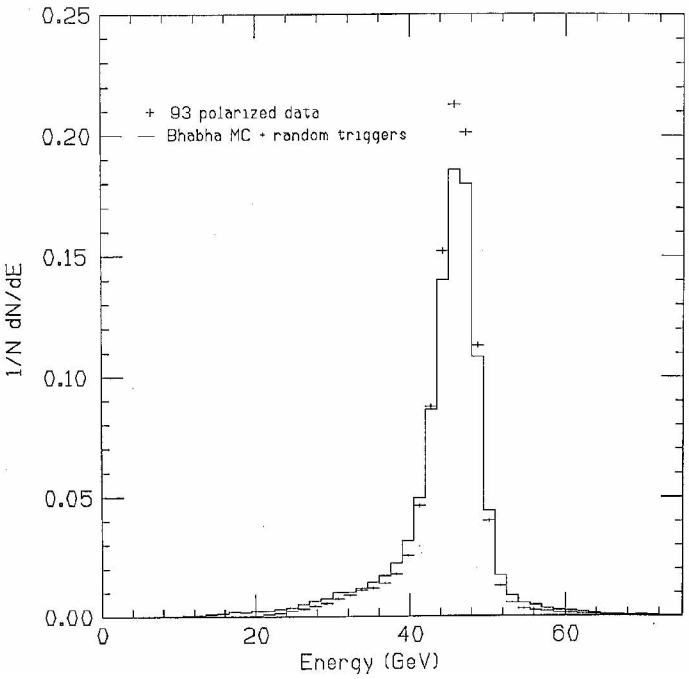

Figure 2.16: Measured energy of Bhabha electrons in the LMSAT.

The small angle Bhabha scattering ($e^+e^- \to e^+e^-$) cross–section into the LMSAT acceptance (σ_{eff}) can be precisely calculated since it is dominated by t–channel photon exchange. The integrated luminosity can then be calculated:

$$\int \mathcal{L}dt = \frac{n_{\text{eff}}}{\sigma_{\text{eff}}} \tag{2.3}$$

where n_{eff} is the sum of Bhabha events that fall within a tight fiducial plus one–half of those that fall within a loose fiducial (but outside the tight fiducial). With this method, calorimeter misalignment effects cancel to first order.[57]

2.3 Data Acquisition

The SLD data acquisition (DAQ) system[58] takes advantage of SLC's low beam crossing rate of 120 Hz by multiplexing and digitizing the data and making a trigger decision in the 8.3 ms between beam crossings. Low–level multiplexing greatly simplifies the output data path and hence reduces the cable plant. The DAQ system will be discussed in three parts: front–end electronics, Fastbus and mainframe computer.

2.3.1 Front–End Electronics

The front–end electronics is mounted on the detector as close as possible to the detector elements. In some cases, low–level signal cables can be completely eliminated by mounting the electronics directly on the feedthroughs. The front–end electronics is responsible for amplifying, shaping, sampling and multiplexing the analog signals. Then it must digitize the signals and pipe them to FASTBUS via optical fibers. Most of the front–end is implemented in custom–made hybrid integrated circuits.

2.3.1.1 Vertex Detector

Much of the vertex detector front–end electronics is built into the CCD chips. Given the proper set of drive pulses, a CCD will move the charges deposited on each pixel to an output node where the pixels can be read out in a serial stream. There are three sets of drive pulses: (i) *Reset* sets the output node to a standard voltage. (ii) *I shift* moves all the charges in the CCD's imaging (active) area down by one row. The bottom–most row moves into the readout register. (iii) *R shift* moves the charges in the readout register over by one column. The end–most pixel's charge is summed into the output node. The readout sequence for each row is: reset, I shift and then 385 R shifts. The sequence must be repeated for all 578 rows to read out the entire VXD. The reset and I shift pulses are generated by a Fastbus VDP module (see section 2.3.2.1), but the R shift pulses are only triggered by the VDP; they are generated by a local R driver on the ladder. The local generation is necessary because each R shift is a series of three fast ($\sim$ 100 ns) pulses during a regulated 540 ns period. The Reset and

I shift pulses are much slower ($\sim 2\,\mu$s). The readout sequence is synchronized across the entire VXD.

The output node is read out by an on–chip source follower with capacitance, $C \simeq 0.12\,$pF $\Rightarrow$ $1\,\mu$V/electron. A bipolar circuit boosts the signal enough to get it out of the cryostat. Once out of the cryostat, local preamplifiers drive the signal through long (25m) coaxial cables to the Fastbus system. This setup requires only one preamp and one cable per $\sim 220,000$ pixels. Since the drive pulses are fairly large (~ 10V), they could interfere with other detector elements. We therefore suspend the VXD readout for a few hundred microseconds around each beam crossing.[45]

2.3.1.2 Wire Subsystems

All of the wire readout subsystems (CDC, ECDC and CRID) use similar front–end electronics. Both ends of each sense wire are treated as separate channels, and in the reconstruction stage charge division determines the z–position. The drift chamber electronics are all mounted on mothercards which connect directly to a group of sense wire cells. Since the CDC superlayers have different radii of curvature, unique mothercard layouts were designed for each superlayer. The CRID electronics is also mounted directly on the sense wires, but the layout of each drift box is identical.

The drift system preamplifier hybrid allows all eight sense wires in a single drift cell to be processed in a single package. The gain resistor is laser trimmed to assure uniformity of channel gain. The calibration substrate includes a precision calibration source and a digital hit trigger system. The trigger system provides a bit pattern of hit wires[§] which can be used in the trigger logic. In order to cope with the avalanche gain of single photoelectron signals, the CRID preamplifier is designed as a single channel hybrid with rapid recovery from large overload signals.

Eight channels of preamplifier output are sent to a high–speed analog waveform sampler called the Hybrid Analog Memory Unit (HAMU). The HAMUs sample each waveform 512 times and hold them until the digitizer is ready for them. At a clock speed of 119 MHz, each sample is 8.4 ns long for a total sampled length of $4.3\,\mu$s.

[§] Those wires that exceed a programmed threshold.

Up to eight HAMUs are multiplexed together to be digitized by one analog–to–digital (A/D) converter. The A/D stage takes $\sim 2\,\mu$s per conversion. Hence, to read out an eight cell CDC mothercard takes $8 \times 8 \times 512 \times 2\,\mu\text{s} \simeq 66$ ms.

2.3.1.3 Calorimeters

All of the calorimetric subsystems (LAC, WIC pads, MASiC and LMSAT) use similar front–end electronics. For the LAC, the electronics is packaged in aluminum cylinders ("top hats") and mounted directly on the feedthrough flanges.[51] The WIC pad electronics is mounted outside the detector in VME crates. The MASiC and LMSAT electronics are mounted behind those detectors in order to prevent the electronics from shadowing any other subsystem.

The signal from each calorimeter tower is read out through a set of three hybrid integrated circuits. The first hybrid protects the data chain from large current spikes due to high voltage discharges in the tower. The second hybrid contains a preamplifier, a pulse shaper, an output driver and a calibration circuit for each channel. The calibration circuit can inject a known amount of charge (laser trimmed to 1/4% accuracy) into the preamplifier. The third hybrid is an analog storage and multiplexing circuit known as a Calorimeter Data Unit (CDU).[59] The CDUs shape and amplify each of 16 channels at gains of $\times 1$ and $\times 8$. Then the CDUs sample the 32 signals at their baseline and their peak. The 64 resulting analog outputs are strobed out in a serial data stream. A separate analog–to–digital board contains A/D converters, each of which receives the output of up to eight CDUs. The signals are digitized to twelve bits at $3.2\,\mu$s per conversion. One parity bit and three framing bits are added, and then the signals are multiplexed onto optical fibers to Fastbus. The WIC differs from this scheme in that its CDU hybrids shape 32 channels at unity gain.[60]

2.3.1.4 Muon Tracker

The muon tracker uses a custom designed CMOS chip to discriminate and multiplex four channels of WIC strips. The front–end card uses four hybrid boards, each of which contains preamplifiers (gain of 50) and two of these custom chips. Thus, each front–end card can read out 32 strips. The cards are daisy–chained together (typically

10 cards per chain), and up to ten daisy–chains are connected to a splitter board. Each splitter board contains a twelve–bit D/A converter to set the threshold voltage, an independent A/D converter to check the threshold and some combinatoric logic to form trigger signals.[61]

2.3.2 Fastbus

The Fastbus system receives the digital signals from the front–end and is responsible for calibration, zero suppression and some signal processing. The Fastbus portion of the data acquisition system uses over 400 Motorola 68020 microprocessors with a computing power of $\sim$ 1 GIPS.[62] There are seven racks of Fastbus crates located in a counting house on top of the SLD. Each of the racks contains four crates, but only three are used for DAQ — the first crate in each rack is dedicated to monitoring and controlling that rack. This is necessary to protect the several million dollars worth of electronics from the $\sim$ 5kW put out by the power supplies per rack. Each subsystem has its own set of unique Fastbus cards, but all subsystems use the following cards: Aleph Event Builders (AEBs)[63] coordinate all of the slave activity within the subsystem and send event information across subsystems. AEBs contain one 68020 CPU with 256 kBytes of buffering memory and have their own unique operating system. Timing and Control Modules (TCMs) provide timing signals to the front–end electronics and the data acquisition modules. All of the signals are derived from a site–wide 119 MHz clock. The TCMs also send various control signals to the front–end electronics.

2.3.2.1 Vertex Detector

As discussed above, the CCDs of the vertex detector need drive pulses for their readout. These drive pulses are created by a custom Fastbus module, the vertex drive power (VDP) module. Each VDP can handle two ladders, 30 VDPs are in use plus a system control module to handle overall timing. A vertex amplifier bias (VAB) module receives, amplifies and shapes the analog signals. Then a vertex data acquisition (VDA) module digitizes the signals, suppresses the zero channels and does

some cluster processing. The VAB modules are all gated off during the R shift pulses in order to avoid interference. Zero suppression removes $\sim$ 99.99% of the channels, reducing the data to a manageable size (about 80 kBytes). The VDA combines pixels into 3×3 kernels around a trigger pixel. This process simplifies later data processing (*e.g.*, finding centroids), but the serial style of readout necessitates storing large amounts of data (three full rows). Each VAB and VDA modules can handle one ladder, 60 of each are in use. The full readout time of 160 ms ($\sim$ 19 beam crossings) is dominated by the length of the R shift sequence. In order to minimize background accumulation, the VXD is read out continuously, and only the 578 rows after each SLD trigger are saved.

2.3.2.2 Wire Subsystems

The drift chambers and the CRIDs use Waveform Sampling Modules (WSMs) to digitize the signals from the wires and then to extract physics data from the waveform. A custom designed Digital Correction Unit (DCU) uses an eight–segment piecewise linearization to correct each bucket for pedestal offsets, gains, nonlinearities, etc. The DCU also suppresses empty buckets away from the signal. WSMs are also equipped with 68020 CPUs to process the waveform and extract data such as the leading edge time and the integrated charge. Each WSM contains four DCUs and four microprocessors, each with an associated memory. The CDC, with 10,240 channels, requires 40 WSMs.

2.3.2.3 Calorimeters

The Fastbus modules that receive the calorimeter data signals are Calorimeter Data Modules (CDMs). The CDMs and similar to WSMs in that they contain DCUs and 68020 CPUs. However, since there are only four samples per channel (not 512 time buckets) and there is no waveform processing to be done, the microprocessors can be utilized to form energy sums, make bit maps of hit towers and suppress empty channels. There are 32 CDMs for the 41,088 channels in the LAC. There are 2 CDMs for the 8640 channels in the WIC pads system.

2.3.2.4 Muon Tracker

The WIC Digital Readout Module (WICDRM) receives WIC strip data from the splitter boards. Each WICDRM contains one 68020 CPU and 256 kBytes of memory to demultiplex and to zero suppress WIC strip data from up to eight splitter boards. If necessary, the CPU can also correct for mismapped cables. Six WICDRMs handle all 90,000 channels.[61]

2.3.2.5 Trigger

A separate AEB is dedicated to making trigger decisions and to collecting the data for triggered events. All of the calorimeter data (including energy sums) is ready before the trigger decision needs to be made. Drift chamber reconstructions are not available, but a secondary path has been built into the front–end electronics which allows limited information from hit wires to be used in triggering. Through pattern matching in the z=0 plane, the trigger can determine if there are high–p_t tracks in an event.[43, 58]

2.3.3 Online Computing

The DAQ mainframe is a DEC VAX 8800. It handles the user interfaces with all aspects of SLD's running and either writes the data to tape locally or pipelines the data to SLAC Computing Service's automated tape handling silos.

Chapter 3

Monte Carlo Simulation

Simulating SLD data is a difficult task, one which would be essentially impossible using purely analytic techniques. Instead, we simulate data using a set of computer programs based on the Monte Carlo method. The Monte Carlo method is a stochastic approach where variables are selected at random — but according to rigid rules — such that in the limit of high statistics all the variable distributions closely approximate physical reality. The advantage of the Monte Carlo method is that for a given event, only one value of each variable is considered, rather than the entire allowed range. This makes the convolution of multiple functions a straightforward task.

This chapter discusses the hadronic event generator and detector simulator which combine to simulate $Z^0 \to q\bar{q} \to$ hadrons events recorded by SLD. We will call this set of programs the "Monte Carlo" (MC). Other event types, generated in a similar manner, will not be discussed here. Some additional simulation, which is needed on a run–by–run basis, is also discussed.

3.1 Event Generator

The JETSET 6.3 Monte Carlo program (created at the University of Lund, Sweden) generates physics events.[64] We can separate the hadronic event generation process into four phases, schematically illustrated in figure 3.1.[65, fig. 1]

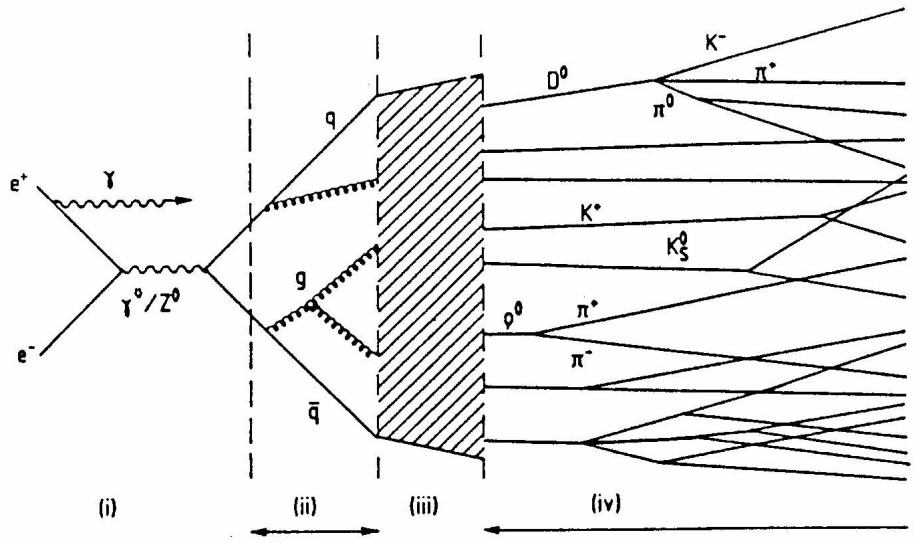

Figure 3.1: Schematic illustration of the event generation process.

(i) An electron–positron pair annihilates forming a Z^0 boson; the Z^0 decays into a $q\bar{q}$ pair.

(ii) The initial $q\bar{q}$ pair radiates gluons; the gluons radiate more gluons and generate more $q\bar{q}$ pairs; and so on. This forms a shower of partons (quarks and gluons).

(iii) The partons combine to form colorless hadrons.

(iv) Any unstable hadrons decay into the experimentally observed particles.

Phase (i) is well modeled by electroweak theory; hence its implementation in JETSET is straightforward. If we allow initial state Bremsstrahlung, then the $q\bar{q}$ invariant mass can be less than M_Z. All the parameters for this phase are based on the standard model.

In JETSET, phase (ii) uses a Parton Shower (PS) model based on the Leading Logarithm Approximation (LLA). The probabilities, $\mathcal{P}$, of $q \to qg$, $g \to gg$ and $g \to q\bar{q}$ branchings are given by the Altarelli–Parisi equations:[65, sec. 2.2.2]

$$\frac{d}{dt}\mathcal{P}_{a\to bc} = \int dz \frac{\alpha_s(Q^2)}{2\pi} P_{a\to bc}(z) \tag{3.1}$$

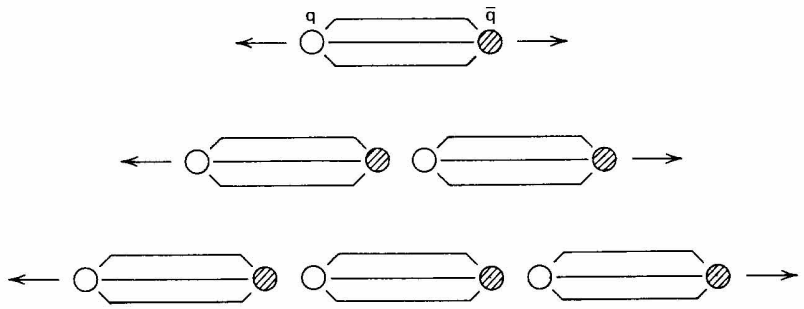

Figure 3.2: Jet formation in the string fragmentation model.

where $t \equiv \ell n(Q^2/\Lambda^2_{LLA})$ is the evolution parameter, z specifies the momentum sharing between the two daughters, and P are the Altarelli–Parisi splitting kernels:

$$P_{q\to qg} = \frac{4}{3}\frac{1+z^2}{1-z} \tag{3.2}$$

$$P_{g\to gg} = \frac{3[1-z(1-z)]^2}{z(1-z)} \tag{3.3}$$

$$P_{g\to q\bar{q}} = \frac{1}{2}[z^2+(1-z)^2] \tag{3.4}$$

The PS model requires two unknown parameters: a lower cutoff, Q_0, to specify the point below which partons cannot radiate and a version of the QCD scale, Λ_{LLA}.*

JETSET has several options for phase (iii); we use its string fragmentation model. The $q\bar{q}$ pair is linked by a color flux tube which stretches as the quarks move apart in space. In the stretching process, the quarks' kinetic energy converts to potential energy stored in the tube. We can parametrize this potential energy as $V(r) \simeq \kappa r$ where $\kappa \sim 1\,\mathrm{GeV/fm}$. When there is sufficient potential energy the tube breaks and creates another quark pair at the point of breakage (see figure 3.2[66]). Despite the additional quark mass, this two–tube configuration is energetically favorable. The quarks continue moving, further stretching the tubes and hence creating more quark pairs. This process continues until the quarks and color flux tubes form on–shell hadrons. The probability of a hadron taking energy fraction z is given by:

*Note that Λ_{LLA} is the leading logarithm approximation of the true (*i.e.*, infinite–order) QCD scale, Λ, and is not the same as the approximation in the $\overline{\mathrm{MS}}$ renormalization scheme, $\Lambda_{\overline{\mathrm{MS}}}$.

$$f(z) = z^{-1}(1-z)\exp\left[-\frac{b}{z}(m^2+p_t^2)\right] \tag{3.5}$$

where the constant $b = 0.7\ \mathrm{GeV}^{-2}$ is determined from fits to experimental data.

In phase (iv), all particles with short lifetimes ($c\tau \lesssim 1\,\mathrm{cm}$) decay according to explicitly specified branching ratios. Where possible, the branching ratios come from experimental measurements; otherwise they are approximated by theoretical estimates. The SLD collaboration has tuned the branching ratios to agree with the latest world averages[6] and recent results, especially in the area of B–physics.[67]

3.2 Detector Simulator

A second program, based on version 3.11 of the GEANT package[68] (developed at CERN), accounts for the interactions between the event particles and the material in the detector. Particles are tracked through a detailed geometric model of the SLD detector in order to assess accurately the material with which each particle comes in contact. GEANT simulates the effects of: energy loss, secondary decays, Bremsstrahlung, Compton scattering, multiple scattering, delta–ray production, gamma conversions, hadronic interactions, photoelectric interactions and positron annihilation.

Despite the great amount of time spent on the geometric model, some detector elements are not properly installed or are missing altogether from the simulation. The one significant mistake that we have found is the omission from the GEANT model of a 100 μm titanium liner inside the beampipe. This omission results in underestimation of the multiple scattering for nearly all particles. Also, we use GEANT's gaussian approximation for multiple scattering. This R_b analysis is very sensitive to the tails of the multiple scattering distribution, and we found the gaussian approximation to be insufficient for our purposes. (For further details see section 5.4.2.) GEANT 3.11 does have a Molière scattering routine, but it does not simulate low Z materials well. Since most of the SLD's inner material is beryllium, this routine is not significantly better than the gaussian approximation.[†][69]

[†] The Molière scattering routine has since been fixed, and in version 3.15 it performs much better than the gaussian approximation.

As GEANT tracks the particles through the detector, it creates the simulated hits using realistic detector resolutions. Whenever possible, the measured resolutions have been used. For the drift chamber, the charge division, drift time and momentum resolutions have all been implemented as measured.

3.3 Run–specific Processing

The detector elements which were not functional during part of the run (due to HV or readout electronics problems) are "turned off" in the Monte Carlo for the appropriate fraction of events. The runs where a given element is off are selected based on random numbers.

Background noise from random triggers is overlaid onto the Monte Carlo events to simulate beam–related backgrounds. The overlay is very important since these backgrounds have never been modeled well. During each year's running, the backgrounds fluctuate over a large range as SLC optimizes the electron and positron trajectories, and they also change significantly during down times as SLC makes hardware improvements. The beam–related backgrounds during the 1992 data run were significantly better than those during SLD's engineering run as well as MARK II's data run.

For the 1992 data run, we selected an overlay set of about 9000 random triggers which occurred within seconds of the hadronic triggers written to tape. The probability that any one of these random triggers is actually a hadronic Z^0 decay is negligibly small. For an average luminosity of 10 Z^0's per hour, the probability is:

$$\mathcal{P}_{(\text{rndm. Z})} = 10\frac{Z^0}{\text{hr}} \cdot \frac{1 \text{ hr}}{3600 \text{ sec}} \cdot \frac{1 \text{ sec}}{120 \text{ beam crossings}} = 0.0023\% \qquad (3.6)$$

Thus the probability that the overlay set of random triggers contains one hadronic Z^0 is only about 20%. The probability that the overlay set contains more than one hadronic Z^0 is negligible.

Chapter 4

Event Selection and Reconstruction

In any physics experiment, useful events must be recognized and stored for later analysis while non–useful events should be discarded. This is known as the *trigger* decision. As explained in section 2.3, the SLD makes a trigger decision between beam crossings, but the readout process can take many beam crossings to execute. To fully read out the CDC takes eight beam crossings during which no other events can be read out (so called *dead time*). The VXD takes even longer to read out, but it can continue taking data while an event is being read out (see sec. 2.3.2.1 for details). Because of this dead time and limited computer resources, some minimum standards must be set to determine which events will be written to tape. If these standards are too loose, the computer system will be swamped with uninteresting events while interesting events will be lost. However, if these standards are too restrictive, they will bias the written sample. Once the data is on tape, we have (almost) unlimited time to filter the events, to fully reconstruct the interesting events and to select those that are valuable for this analysis.

4.1 Trigger

Many different triggers were used during the 1992 data run. Since this was the SLD's first data run, the triggers were adjusted many times as we attempted to optimize them for event efficiency and background rejection. The five triggers that were implemented for the majority of the 1992 data run were:

Random Designed to monitor backgrounds, the random trigger fires on a beam crossing at a rate of $\frac{1}{20}$ Hz. All subsystems are read out.

Luminosity This trigger is designed to capture Bhabha events. It requires two back–to–back LMSAT towers to each have 10 GeV deposited in them. Since there is no tracking coverage in the LMSAT region, the tracking and CRID subsystems are not read out.

Energy The energy trigger only requires that the sum of the total energy in the LAC exceed 8 GeV.* However, to suppress backgrounds, only towers that exceed a "high" threshold are included in the sum. The "high" threshold is 125 MeV (60 ADC counts) in the electromagnetic sections and 650 MeV (120 ADC counts) in the hadronic sections. These are significantly higher thresholds than the readout thresholds of 16 and 65 MeV (8 and 12 ADC counts).[53]

The energy trigger is designed to collect a maximal number of events to be used in analyses which do not require tracking information (*i.e.* the left–right asymmetry). Since many events are missing tracking information — due to CDC high voltage trips and/or poor functioning of the ECDC's — the energy trigger only reads out the calorimeter subsystems.

Tracking The tracking trigger requires two or more "fast" tracks in the CDC with an opening angle greater than 20°. There is no explicit energy requirement, but in order to be recognized by the Fastbus pattern recognition, a track must have $p_t > 180$ MeV. [43, sec. 9.3.3] All subsystems are read out.

*Standard energy scale. See section 2.2.3.2 for more details.

Hadron The hadron trigger is a logical AND of the energy trigger and the tracking trigger (modified to require only one track). Nearly all of the tracking and energy triggers also satisfied the hadron trigger. All subsystems are read out.

The combined triggering and selection efficiency for $Z^0 \to q\bar{q}$ events is at least 92%.[52] However, this estimate includes events where the energy trigger is set, but where neither the tracking nor the hadron triggers are satisfied. In these events tracking information is not read out, hence these events are not useful for this analysis. Since this analysis uses the ratio of numbers of events, the trigger efficiency for useful events cancels and we do not need to know what it is. The trigger bias towards different quark flavors is very small and can be neglected in comparison to the event selection bias which will be discussed later.

4.2 Filter

After the data is written to tape it passes through an offline filter program designed to separate the events by trigger type and to discard bad events. The filter does some reconstruction, such as energy clustering and pedestal subtraction, but it does not do a full reconstruction. Only events that pass a filter are fully reconstructed. For this analysis we use the dataset referred to as HAD92P, which contains energy and hadron triggers that pass the hadronic filter. Other datasets are made for tracking triggers (μ–pairs), luminosity triggers (Bhabha events) and random triggers (backgrounds). Hadronic events that are of questionable quality are investigated "by hand" and physicists determine whether or not to retain them.

The requirements of the hadronic filter are: (i) Large total energy in the LAC (using the readout thresholds), $E_{\rm LAC} > 14\,{\rm GeV}$. (ii) Small energy in the endcap WIC, $E_{\rm WIC} < 11\,{\rm GeV}$. This removes events which trigger due to background muons. (iii) Reasonable energy imbalance, $E_{\rm imb} < 0.9$, and sphericity, $S < 1.0 - E_{\rm imb}$, where $E_{\rm imb}$ is the energy asymmetry between the two hemispheres defined by the plane perpendicular to the sphericity axis. The sphericity axis is the axis which minimizes the quantity $S = \frac{3}{2}\left[\sum_j (p_{j\perp})^2 / \sum_j (p_j)^2\right]$ where j runs over all clusters in the calorimeter. This cut is designed to remove backgrounds such as beam–gas and beam–wall

interactions.

The remaining event sample is mostly hadronic Z^0 decays, but it also contains a significant number of τ–pair and wide–angle Bhabha events and a small number of junk events. To eliminate these backgrounds and to select appropriate events, this analysis uses a set of event selection cuts (described in section 4.4). These cuts do require full reconstruction of the events.

4.3 Event Reconstruction

After hadronic events are filtered out, they are fully reconstructed. This analysis only uses tracking information; hence the reconstruction of calorimetric and particle identification information will not be described.

4.3.1 Track Reconstruction

The hits in the CDC are combined within their cell to form vectored hits, and then the vectored hits are attached to form charged tracks. The multiple scattering within the CDC active volume is fairly small and may be safely approximated. The hit pixels in the VXD were already clustered into kernels by the VDA modules (see sec. 2.3.2.1). Now, tracks are extrapolated to the VXD and we attempt to link kernels with tracks. The search area in the VXD is defined by the track parameter uncertainties and the approximate multiple scattering uncertainty. If any VXD clusters are linked to a track, the track is recalculated using the Billior method[70] which takes into account the detailed geometry and its associated multiple scattering error. The Billior method is very time consuming, but it does provide better track fits when there is much intervening material. The vectored hits and kernels are removed from their respective lists before the next track is fit.

The number of hit pixels arising from data tracks per event is fairly small, of order 350, compared to a total occupancy of $\sim 10,000$ pixels. The majority of the background hits come from X–ray conversions and up–stream tracks parallel to the beam which accumulate during the 19 beam crossings that it takes to read out the

VXD. Electronic noise is not negligible, contributing roughly 500 background pixels per event. Cluster shape can remove a significant fraction of the backgrounds, since perpendicular tracks, such as data tracks, generally leave clusters that fit within a 3×3 kernel. Parallel tracks, such as SLC–generated muons, usually leave highly elongated clusters — often hundreds of pixels by three pixels. The mislinking fraction for high momentum tracks (> 1 GeV/c) is about 0.5%. For low momentum tracks the search area is less well defined and the mislinking fraction rises to about 4%.[46]

4.3.2 Interaction Point Reconstruction

The SLC interaction point has an RMS cross–section of $\sim 2.2\,\mu\text{m} \times 2.2\,\mu\text{m}$ with a length of $\sim 650\,\mu\text{m}$. SLC has an intricate network of feedforward devices to maintain such narrow beams in collision and to stabilize the IP position. We track the IP using hadronic Z^0 events recorded in SLD. Using samples composed of about ten events measured over a period of less than three hours, we fit the x and y position of the primary vertex to the small impact parameter tracks (at least 50). In the 1992 data run we had 447 samples, all with errors in the range of $\sigma_x, \sigma_y \simeq 10 - 15\,\mu\text{m}$. This range of error agrees well with the σ_{IP} derived from muon pair and Bhabha events: $\sigma_{\text{IP}} = 11\,\mu\text{m}$.[38] The z position must be determined from each event separately. We calculate the point of closest approach (POCA) of each track to the line defined by $x = x_{\text{IP}}$ and $y = y_{\text{IP}}$. z_{IP} is defined as the mean of the z–component at the POCA for each track. According to the Monte Carlo, this definition differs from the true z_{IP} by roughly a gaussian of width near $30\,\mu\text{m}$.

4.3.3 Jet Finding

The initial b–quark momentum direction can be approximated by the axis of the jet formed by its hadronization and decay products. Therefore we divide each event into jets using the JADE algorithm.[71] This algorithm first defines each track to be an individual cluster with energy determined assuming a massless particle. The algorithm then loops over all pairs of clusters and calculates a scaled invariant mass

squared for each pair:

$$y_{ij} \equiv \frac{M_{ij}^2}{E_{\rm vis}^2} = \frac{2E_iE_j(1-\cos\theta_{ij})}{E_{\rm vis}^2} \tag{4.1}$$

The pair with the lowest y_{ij} is combined into a single cluster by adding their four–momenta together. The invariant masses are then recalculated and the procedure repeats until all clusters have masses $y_{ij} > y_{cut}$. The clusters that remain are defined as jets. A higher value of y_{cut} leads to more two–jet events while a lower value of y_{cut} leads to more many–jet events. For this analysis we use $y_{cut} = 0.02$, which gives roughly equivalent numbers of two– and three–jet events.

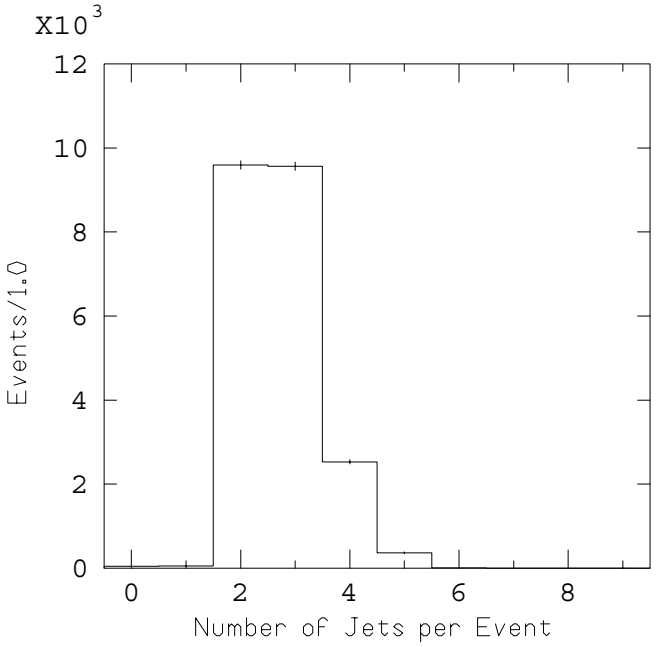

Figure 4.1: Number of jets per hadronic Monte Carlo event with $y_{cut} = 0.02$.

The event thrust axis is also calculated at the same time. The thrust axis, $\hat{t}$, maximizes the quantity $T = \sum_j(\vec{p}_j \cdot \hat{t})/\sum_j |\vec{p}_j|$ where j runs over all charged tracks.

4.3.4 Impact Parameter Determination

The three–dimensional impact parameter, b, is calculated for each track by minimizing the distance from the IP to the helix which describes the track:

$$X(\beta) \;=\; a\sin\beta\cos\phi + a(1-\cos\beta)\sin\phi + \rho\cos\phi_x \tag{4.2}$$

$$Y(\beta) = a\sin\beta\sin\phi - a(1-\cos\beta)\cos\phi + \rho\sin\phi_x \quad (4.3)$$

$$Z(\beta) = a(\tan\lambda)\beta + Z_0 \quad (4.4)$$

where ρ, ϕ_x and Z_0 define the initial track position, ϕ and λ define the direction of the track's initial momentum and a is the helix radius. The distance from the IP to the track is given by:

$$I(\beta) = \sqrt{(X(\beta)-x_{\rm IP})^2 + (Y(\beta)-y_{\rm IP})^2 + (Z(\beta)-z_{\rm IP})^2} \quad (4.5)$$

This distance is minimized at $\beta = \beta_0$ where:

$$\beta_0 = \frac{-\rho\cos(\phi-\phi_x) + x_{\rm IP}\cos\phi + y_{\rm IP}\sin\phi + (z_{\rm IP}-Z_0)\tan\lambda}{a\sec^2\lambda} \quad (4.6)$$

hence $b \equiv I(\beta_0)$. The expected uncertainty in the impact parameter, σ_b, is determined by propagating the track's error matrix to the point of closest approach (POCA) and projecting it along the vector from the primary to the POCA. This is combined in quadrature with the error on the IP projected along the same vector.

In order to eliminate tracks which miss the IP due to detector resolution we assign each track's impact parameter a sign. We attribute positive sign to those tracks which cross their associated jet's axis in front of the IP and thus could have been a decay product of a particle moving along that jet axis. We attribute negative sign to those tracks that cross their jet's axis behind the IP. Rather than attempting to compute the crossing point we look at the angle between the jet axis and the vector from the IP to the POCA (see fig. 4.2). If this angle is less than 90° (positive dot product) the impact parameter is called positive. If this angle is greater than 90° (negative dot product) the impact parameter is called negative.

4.4 Hadronic Event Selection

Events that do not contain full tracking information are removed from the event sample. In most cases this was due to high voltage trips in the CDC, although in some cases there were failures in the VXD readout electronics. In addition, several cuts (summarized in table 4.1) are imposed on the sample in order to eliminate $Z^0 \to \tau^+\tau^-$

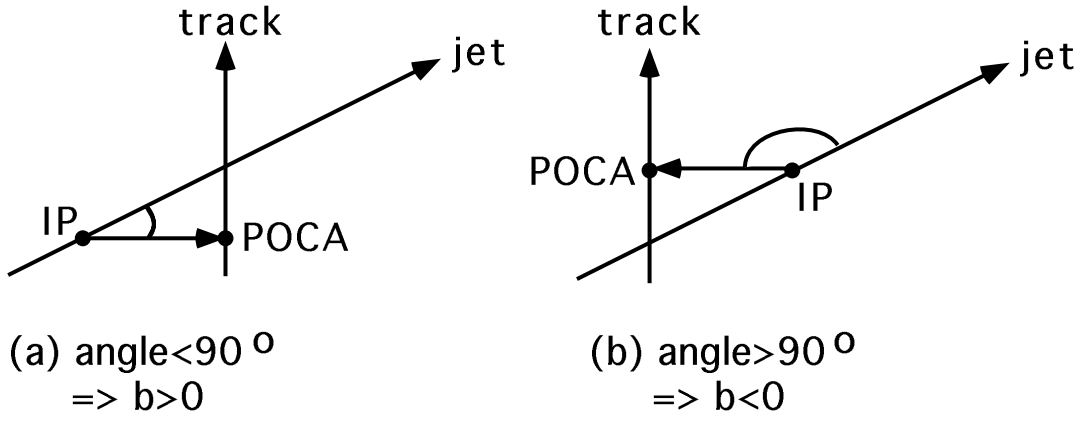

Figure 4.2: Examples of tracks with (a) positive and (b) negative impact parameters.

Event Quality	Cut Value
Visible energy from tracks	$E_{vis} \geq 18.0$ GeV
Thrust axis well inside CDC	$\lvert\cos(\theta_{\rm thrust})\rvert \leq 0.71$
Many tracks	$N_{\rm trk} \geq 7$
Tracks with VXD links	$N_{\rm in} \geq 3$

Table 4.1: Event quality cuts.

events and other non–hadronic backgrounds. In this analysis, the visible energy is calculated from tracking information only, ignoring the calorimetry data. The cut on $E_{\rm vis}$ assures us that at least several of the tracks are stiff enough to reconstruct well. Requiring the thrust axis (defined above) to be well inside the CDC assures us that most of the tracks are within the tracking fiducial volume. The most significant cut is the minimum number of tracks. This cut eliminates the vast majority of τ–pair and WAB events which have a maximum of six tracks, exclusive of radiative tracks. We require that several tracks be *inner*, that is, composed of a CDC segment that is linked to VXD hits. During the 1992 data run, the SLD recorded 13,914 events, only 8,778 of which had full tracking information. The event cuts left only 5,764 $Z^0 \to q\bar{q} \to$ hadrons events for use in this analysis. Calorimetric analyses have identified 10,437 events as being Z^0 decays[†] — 10,224 of which have good polarization

[†] The non-Z^0 events are about 2000 wide–angle Bhabha events and about 1500 "trash" events. The "trash" events include spurious triggers, beam–related backgrounds, partial events, etc.

measurements — with a background measured to be 209 ± 73 events.[72, 73]

Some of the interesting event properties are shown in the following figures. In each case, the real data is plotted as $\diamond$ over a histogram of the (hadronic) Monte Carlo. For each event property there are two figures. The left–hand figure contains all events that have some CDC and VXD information; the right–hand figure contains only those events that pass the event selection. Figure 4.3 shows the number of charged tracks and the number of inner charged tracks. In both of these figures it can be seen that the event cuts successfully remove low multiplicity backgrounds and bring the data and the Monte Carlo into agreement. Section 5.4.1 corrects for the systematic shift visible in the inner track plots. Figure 4.4 shows the visible energy and the thrust angle. The backgrounds primarily removed by the visible energy cut are $Z^0 \to \mu^+\mu^-$ and $Z^0 \to \tau^+\tau^-$.

4.5 Event Displays

Figures 4.5 and 4.6 show two different views of event 1762 from run 13652. In both, the event is viewed along the beam (z) axis. In the first view, the CDC is shown with the raw hits, vectored hits and reconstructed tracks visible. The noise level in this event is typical and can be seen from the number of raw hits that are not vectored. The set of vectored hits that are visible in the bottom center are not reconstructed into a track since such a track would miss the beamline by tens of centimeters. In the second view, only the hit CCDs in the VXD are shown, along with the VXD hits and the reconstructed tracks. The IP is clearly visible as well as evidence for several separated vertices.

Figures 4.7 and 4.8 show two different views of event 2703 from run 13685. The first display is the z–axis VXD closeup, as above. The second display is also a VXD closeup, but the viewpoint is rotated 90° to an axis transverse to the beam. In both views, the IP is visible and one separated vertex is obvious.

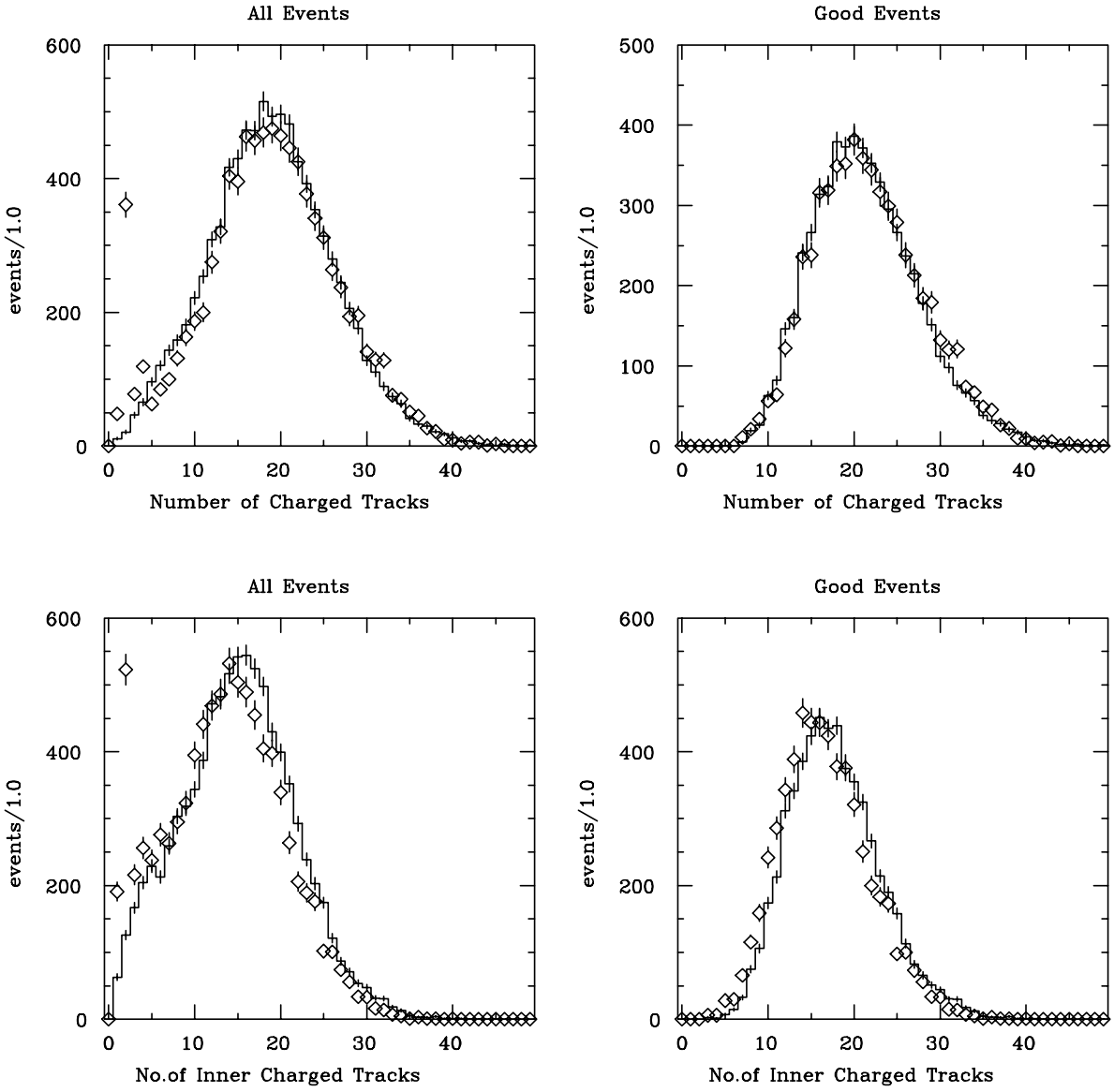

Figure 4.3: Number of charged tracks and number of inner charged tracks per event. Data ($\diamond$) over uncorrected Monte Carlo (histogram).

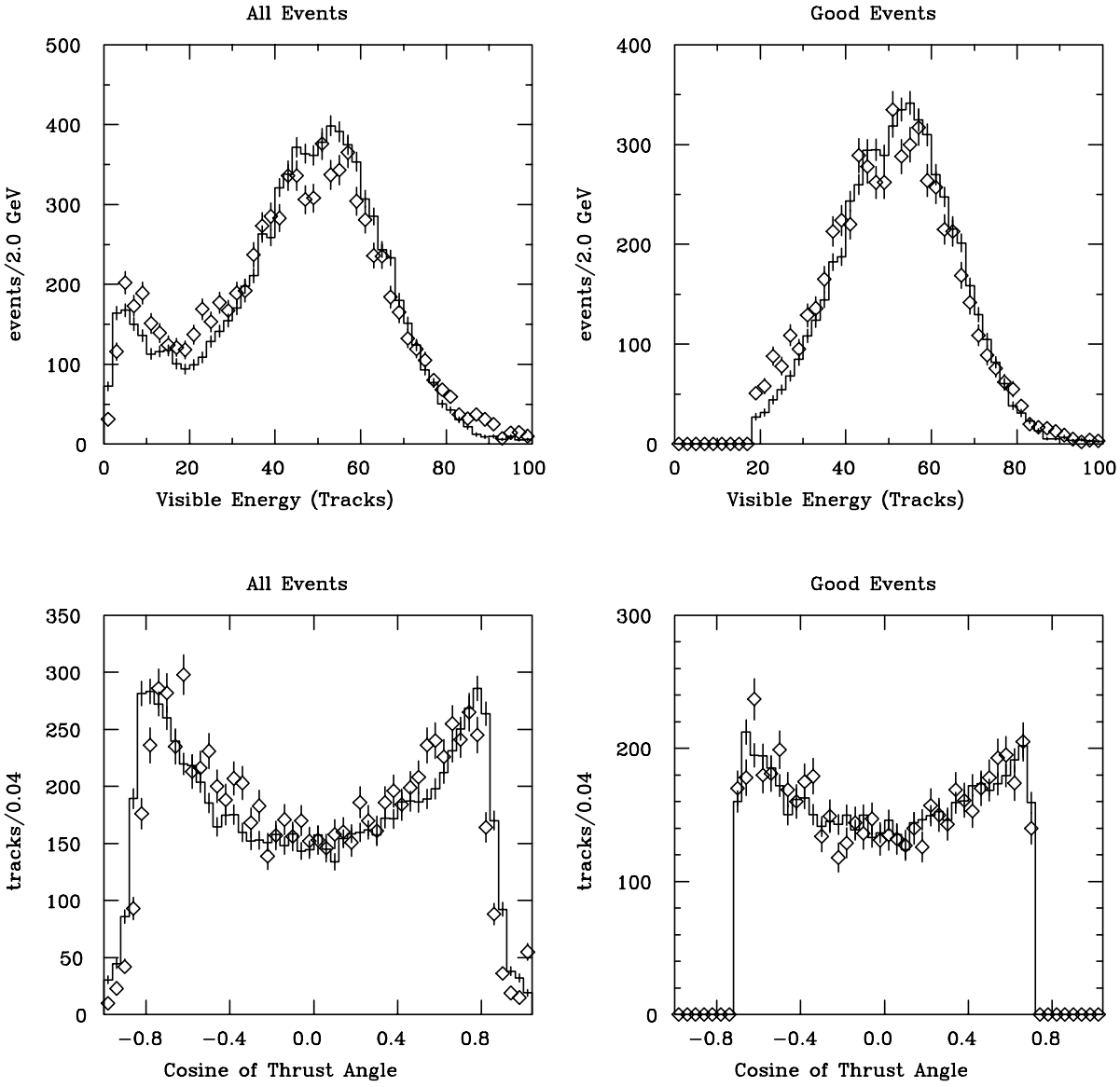

Figure 4.4: Visible energy from tracks and cosine of thrust angle.
Data ($\diamond$) over uncorrected Monte Carlo (histogram).

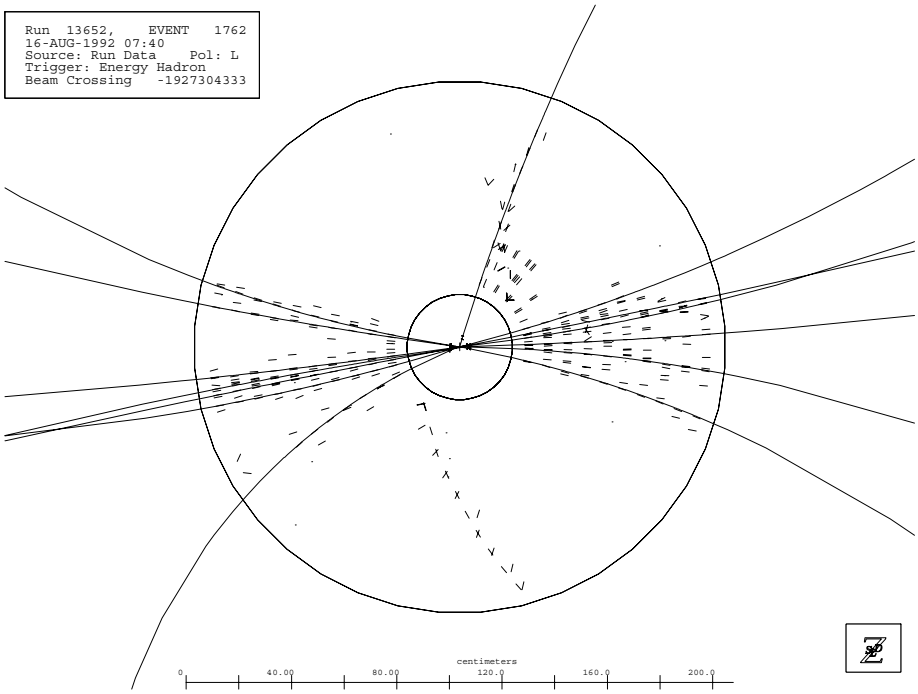

Figure 4.5: Event display looking along the z–axis at the raw CDC hits, vectored CDC hits and reconstructed tracks.

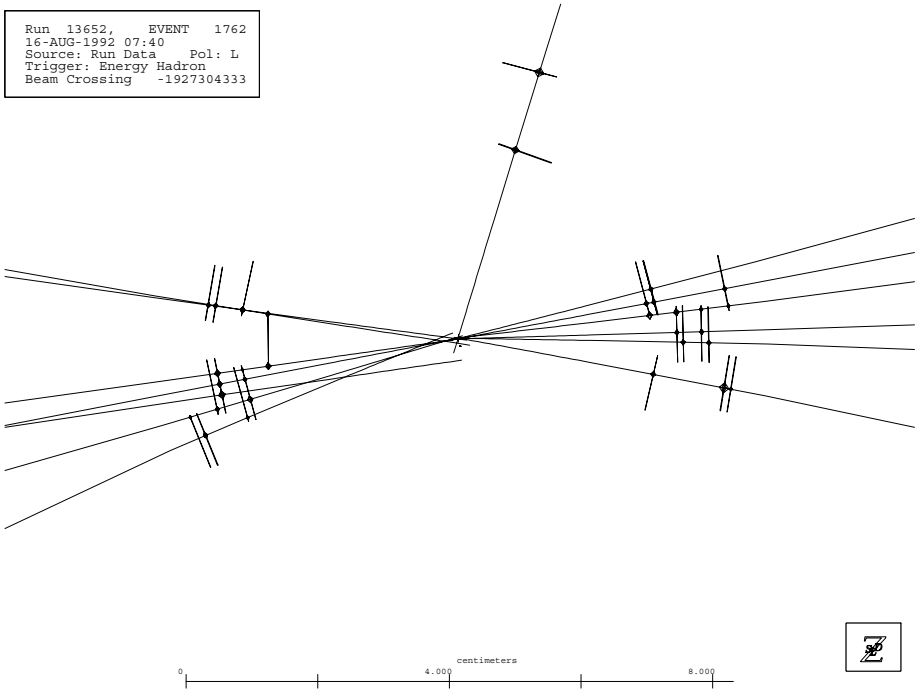

Figure 4.6: Event display looking along the z–axis at the VXD hits and reconstructed tracks.

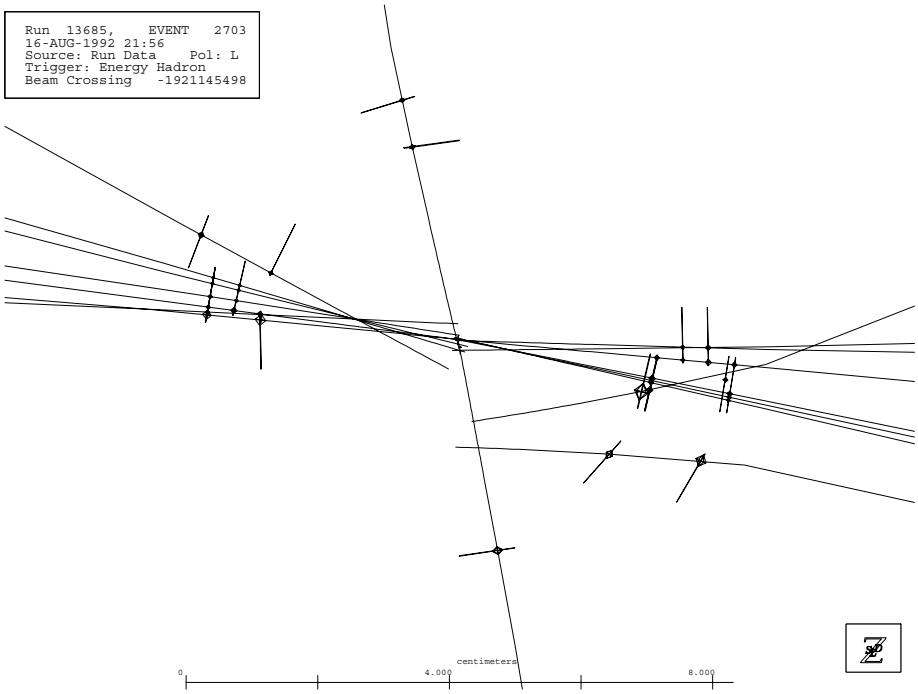

Figure 4.7: Event display looking along the z–axis at the VXD hits and reconstructed tracks.

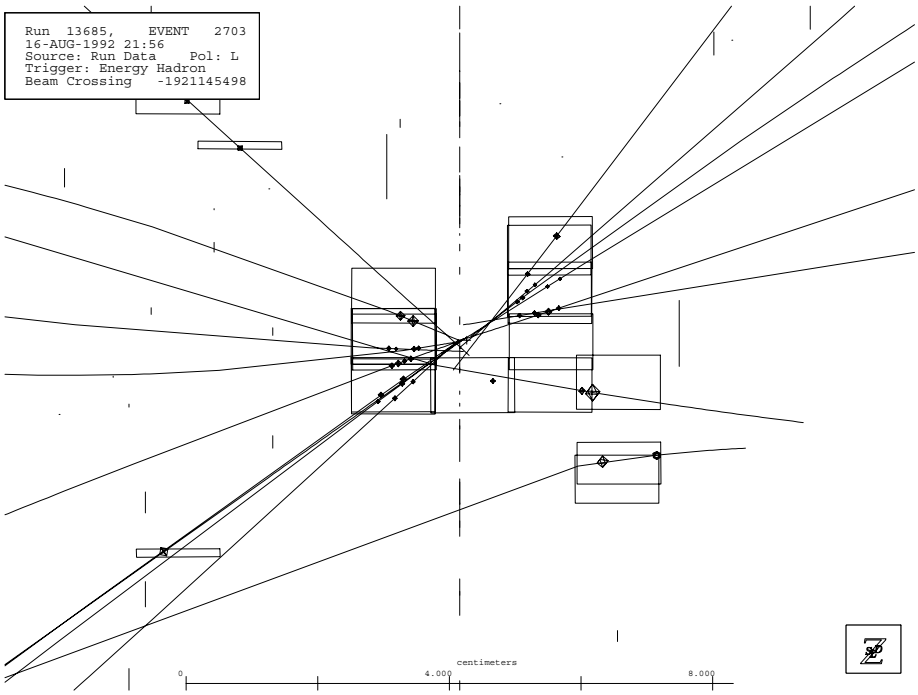

Figure 4.8: Event display looking along the x–axis at the VXD hits and reconstructed tracks.

Chapter 5

Data Analysis

In this chapter, the technique used to distinguish $Z^0 \to b\bar{b}$ events from other hadronic events will be discussed. This chapter will also describe the determination of R_b. Also covered will be corrections to the Monte Carlo and backgrounds. Understanding the corrections and the backgrounds is critical to the accurate determination of R_b.

5.1 Analysis Technique

To tag $Z^0 \to b\bar{b}$ events we calculate the three–dimensional impact parameter (b) for all well–measured tracks. On average, $Z^0 \to b\bar{b}$ events have many tracks with large impact parameters while all other types of events do not. This distinction is primarily due to the relatively long lifetime of B hadrons ($c\tau \approx 435\,\mu$m) and to their large boost ($\beta\gamma \sim 8$) in the lab frame. In addition, many of the final state particles from $Z^0 \to b\bar{b}$ events come from cascade D meson decays and hence have effective lifetimes of $\tau_{eff} \sim \tau_B + \tau_D \;\Rightarrow\; c\tau_{eff} \sim 600\,\mu$m. Our main background comes from charmed hadrons produced directly in $Z^0 \to c\bar{c}$ events. Direct D mesons are very difficult to remove as they also have large lifetimes ($c\tau_{D^\pm} \simeq 325\,\mu$m and $c\tau_{D^0} \simeq 125\,\mu$m)) and a comparable boost. The rationale underlying the use of a three–dimensional impact parameter rather than a more conventional two–dimensional impact parameter is inherent in the three–dimensional nature of SLD's superb vertex detector. The intrinsic resolution of the VXD is roughly $5\,\mu$m in all three directions; the failure

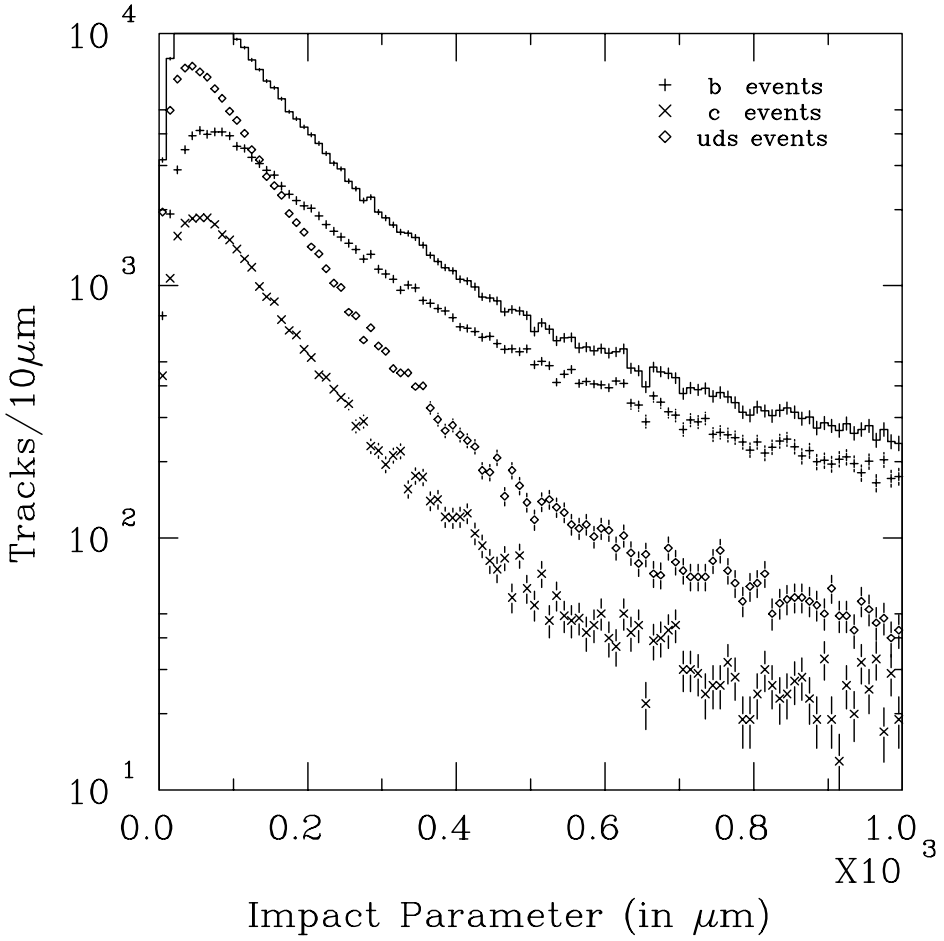

Figure 5.1: Impact parameter distribution for various event types from the Monte Carlo.

to use one dimension would result in a tremendous loss of information. In practice, the resolution is limited by alignment, which is worst in the z–direction. Figure 5.1 shows the Monte Carlo distribution of impact parameters for various event types. Note that the relative normalization of b– to c– to uds–events is given by the minimal standard model expectations, $R_b = 0.22$ and $R_c = 0.17$. Also, we have not attempted to remove long–lived backgrounds such as $\mathrm{K}^0_\mathrm{s}(c\tau \simeq 2.7\mathrm{cm})$, $\Lambda^0(c\tau \simeq 7.9\mathrm{cm})$ or photon conversions.

Before using the impact parameters in tagging, we want to factor out the known measurement uncertainties. Therefore we also calculate an expected uncertainty in the impact parameter (σ_b). In two dimensions this uncertainty can be parametrized

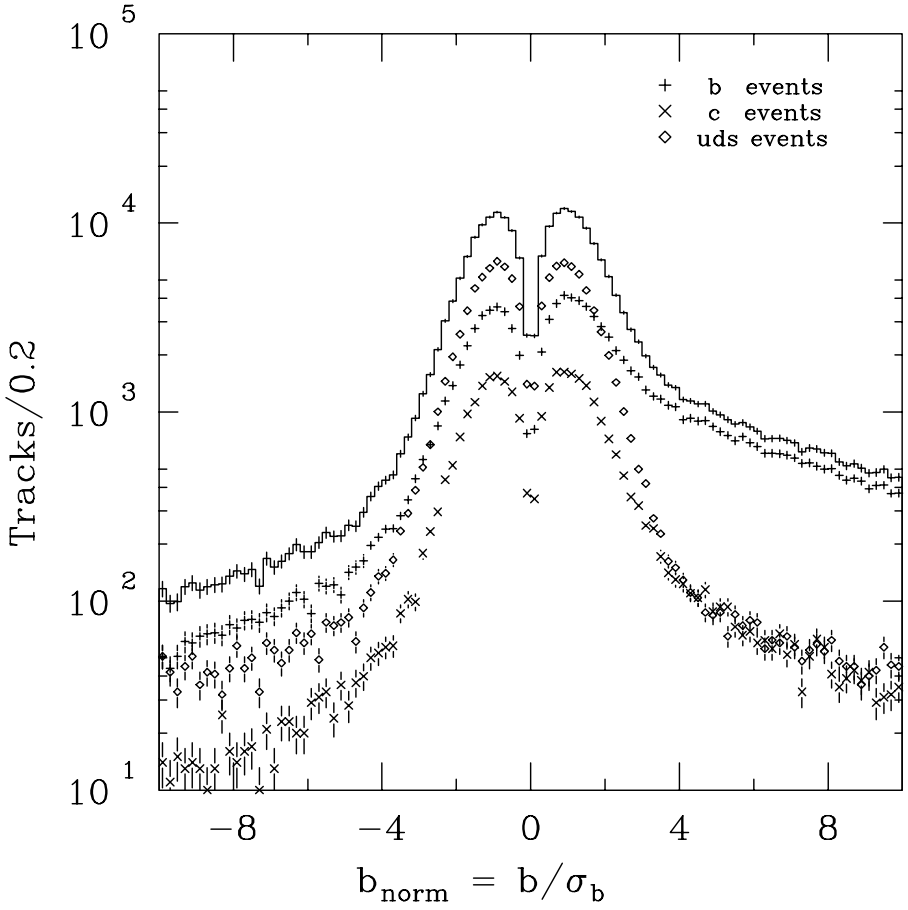

Figure 5.2: Normalized impact parameter distribution for various event types from the Monte Carlo.

as:

$$\sigma_{\rm b}^{xy} = \sqrt{(13\,\mu{\rm m})^2 + \frac{(70\,\mu{\rm m})^2}{p^2\cos^3\theta}} \tag{5.1}$$

where p is in GeV.[38] In three dimensions the formula is more complicated, but it exhibits similar behavior, approaching infinity as $p \to 0$ and approaching a constant as $p \to \infty$. The tagging is done with the normalized impact parameter:

$$b_{\rm norm} \equiv b/\sigma_b \tag{5.2}$$

which expresses the significance of this track missing the primary vertex. Figure 5.2 shows the Monte Carlo distribution of normalized impact parameters, with the distributions normalized in the same manner as the previous figure.

The $Z^0 \to b\bar{b}$ tag chosen is to count the number of high impact parameter (HIP) tracks per event. Those events which have at least the required number of HIP tracks are tagged as being $Z^0 \to b\bar{b}$ events. We define HIP tracks as those whose significance (normalized impact parameter) exceeds the significance cut. Thus defined, HIP tracks have a very high probability of not originating from the primary vertex; several HIP tracks implies the existence of at least one separated vertex. There is a large area in parameter space where the cuts are stringent enough to remove the majority of $Z^0 \to c\bar{c}$ events, but not so strong as to have a low $Z^0 \to b\bar{b}$ efficiency. $Z^0 \to c\bar{c}$ events remain the largest background.

5.2 Extraction of R_b

If this technique were perfectly efficient and perfectly pure, then R_b would be simply the ratio of the number of events tagged to the number of hadronic events. Unfortunately this is not the case. R_b is defined by:

$$R_b \equiv \frac{N_b}{N_b + N_c + N_{uds}} \tag{5.3}$$

where the N_q are the number of $Z^0 \to q\bar{q} \to$ hadrons events in the data sample. If we assume that our sample is purely hadronic, then we measure the total number of hadronic events:

$$N_{\rm tot} = N_b + N_c + N_{uds} \tag{5.4}$$

We also measure the total number of tagged events:

$$T_{\rm tot} = T_b + T_c + T_{uds} \tag{5.5}$$

We can define the tagging efficiencies as:

$$\epsilon_q \equiv T_q/N_q \qquad \Rightarrow \qquad T_q = \epsilon_q N_q \tag{5.6}$$

hence:

$$T_{\rm tot} = \epsilon_b N_b + \epsilon_c N_c + \epsilon_{uds} N_{uds} \tag{5.7}$$

If we assume that we can determine the three tagging efficiencies from the Monte Carlo, then we have two equations with three unknowns. We can eliminate the remaining unknown by using the measured value of R_c:[74]

$$R_c \equiv \frac{N_c}{N_b + N_c + N_{uds}} = 0.17 \pm 0.017 \tag{5.8}$$

We also use the definition:

$$R_{uds} \equiv \frac{N_{uds}}{N_b + N_c + N_{uds}} \equiv 1 - R_b - R_c \tag{5.9}$$

$$\begin{aligned}
\Rightarrow T_{\rm tot} &= \epsilon_b R_b (N_b + N_c + N_{uds}) + \epsilon_c R_c (N_b + N_c + N_{uds}) && (5.10)\\
&\quad + \epsilon_{uds}(1 - R_b - R_c)(N_b + N_c + N_{uds}) \\
\Rightarrow \frac{T_{\rm tot}}{N_{\rm tot}} &= \epsilon_b R_b + \epsilon_c R_c + \epsilon_{uds}(1 - R_b - R_c) && (5.11)\\
\Rightarrow \frac{T_{\rm tot}}{N_{\rm tot}} &= (\epsilon_b - \epsilon_{uds}) R_b + (\epsilon_c - \epsilon_{uds}) R_c + \epsilon_{uds} && (5.12)\\
\Rightarrow (\epsilon_b - \epsilon_{uds}) R_b &= \frac{T_{\rm tot}}{N_{\rm tot}} - (\epsilon_c - \epsilon_{uds}) R_c - \epsilon_{uds} && (5.13)
\end{aligned}$$

Therefore:

$$R_b = \frac{\frac{T_{\rm tot}}{N_{\rm tot}} - (\epsilon_c - \epsilon_{uds}) R_c - \epsilon_{uds}}{(\epsilon_b - \epsilon_{uds})} \tag{5.14}$$

Typical tagging efficiencies are: $\epsilon_b = 75\%$, $\epsilon_c = 20\%$ and $\epsilon_{uds} = 2.5\%$. Note that we have assumed: (i) The event selection is unbiased. This assumption is discussed in detail in section 6.2.3. (ii) Backgrounds in the hadronic event sample are negligible. This assumption is discussed in detail in section 5.5. (iii) Tagging efficiencies are well modeled in the Monte Carlo, after corrections. This assumption is checked by comparing the R_b's calculated over a reasonable range of cuts (see fig. 6.4). Since each set of cuts leads to a different — but consistent — set of ϵ_q, the quality of the corrected Monte Carlo is measured by the flatness of R_b as a function of the cuts. This type of analysis cannot measure R_b to the 1% level: to do that one must measure the efficiencies with the data.

5.3 Track Selection

This analysis depends heavily on good track reconstruction. Since the SLD track reconstruction algorithm is optimized for efficiency, rather than for purity, we must remove tracks with questionable quality. The cuts applied to individual tracks are listed in table 5.1. For good events, an average of 12.5 tracks per event pass these cuts.

Track Quality	Cut Value
Quality of fit for CDC track	$\chi^2/dof \leq 5.0$
Number of CDC hits on track	$N_{hit} \geq 40$
$\sqrt{x^2+y^2}$ of first hit in CDC	$R_{CDC} \leq 40$ cm
Transverse momentum	$p_t > 0.010$ GeV/c
Impact parameter	$b \leq 0.3$ cm
Error on impact parameter	$\sigma_b \leq 250\,\mu$m
Z at point of closest approach	$Z \leq 1.0$ cm

Table 5.1: Track quality cuts

The first three cuts look only at the drift chamber segment of the tracks. Cutting on χ^2 per degree of freedom at five significantly improves the agreement with the Monte Carlo (see fig. 5.3). The CDC can make up to 80 measurements per track starting at $R = 20$ cm. We require 40 or more hits to reduce the number of "stub" tracks formed by vectored hits in only a few layers or at large $|\cos\theta|$ (see fig. 5.4). There is still some disagreement at the high end of the distribution (see fig. 5.5). This disagreement is probably related to the unmodeled tracking inefficiency discussed in section 5.4.1. Tracks that start in the middle of the CDC are often caused by K^0_s or Λ^0 decays, photon conversions or kinked tracks (from nuclear interactions or δ–rays). The information derived from the first few superlayers is critical for VXD linking; hence we eliminate tracks that start further than 40 cm from the beamline. The agreement with the Monte Carlo is reasonably good (see fig. 5.6).

The p_t cut is nominal, and it is duplicated by the σ_b cut. The cut on impact parameter is designed to remove background tracks such as K^0_s and Λ^0 decays and photon conversions as well as some mislinked tracks. These backgrounds have fairly flat distributions whereas the b tracks fall off rapidly. The cut on expected uncertainty

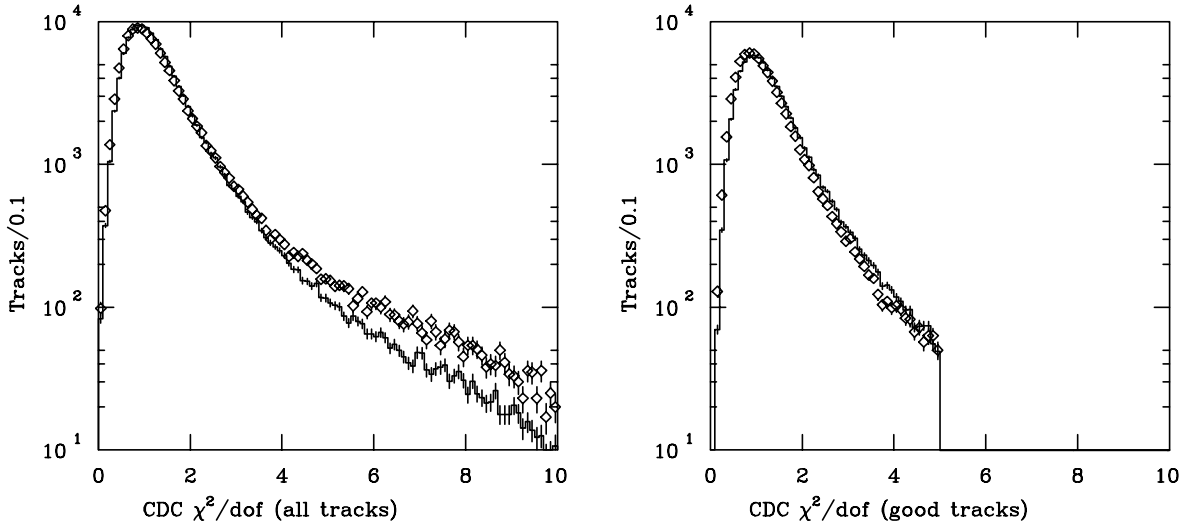

Figure 5.3: χ^2/dof of CDC track fit for all tracks (left) and those passing the track cuts (right). Data ($\diamond$) over Monte Carlo (histogram)

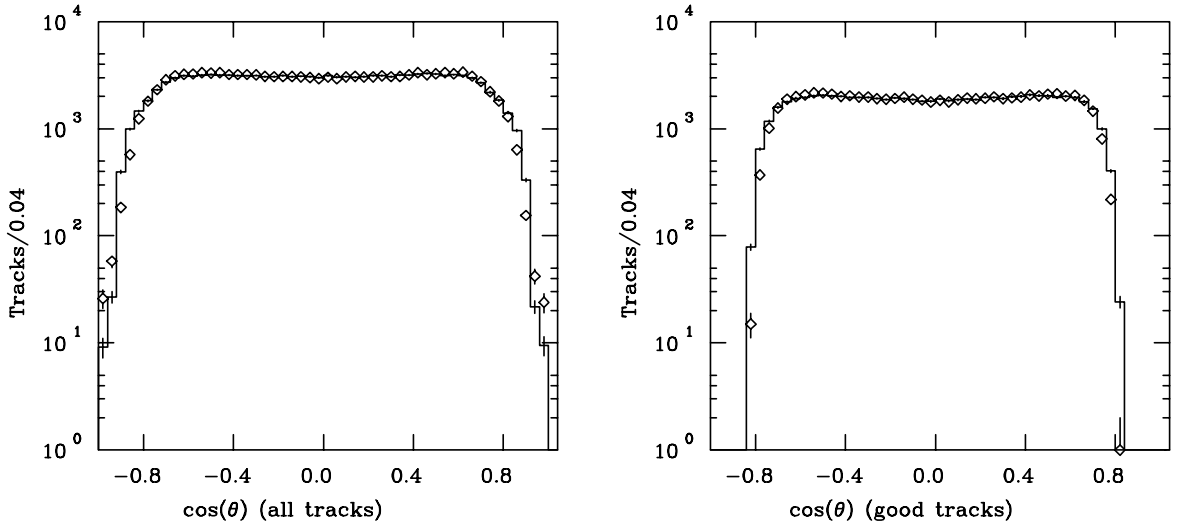

Figure 5.4: $\cos\theta$ for all tracks (left) and those passing the track cuts (right). Data ($\diamond$) over Monte Carlo (histogram)

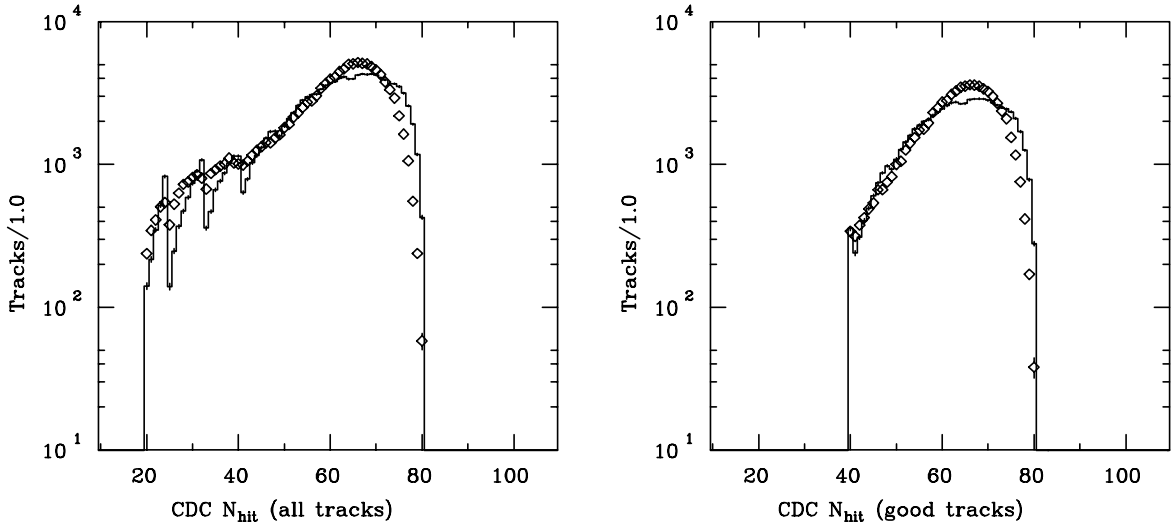

Figure 5.5: Number of CDC hits per track for all tracks (left) and those passing the track cuts (right). Data ($\diamond$) over Monte Carlo (histogram)

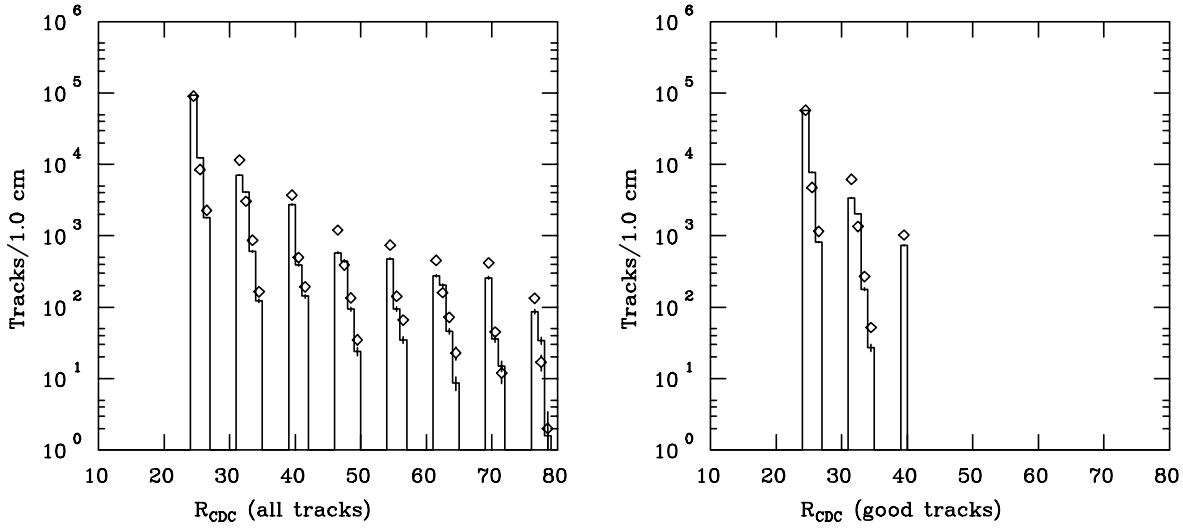

Figure 5.6: R_{CDC} for all tracks (left) and those passing the track cuts (right). Data ($\diamond$) over Monte Carlo (histogram)

in the impact parameter (σ_b) is primarily a cut on p_t, but it also removes some tracks which are poorly measured for other reasons. The Z cut is a holdover from the two–dimensional analysis and is entirely duplicated by the 3 mm cut on b.

5.4 Corrections to the Monte Carlo

As mentioned previously, the Monte Carlo is not perfect. Some of the imperfections are due to blunders, some are due to insufficiently accurate approximations, but most are due to unknown factors. As differences between data and Monte Carlo are tracked down, the Monte Carlo is improved to better simulate the data. However, discrepancies remain that are not understood and hence cannot be corrected in the Monte Carlo. In this section we attempt to adjust the Monte Carlo in an *ad hoc* manner to reduce or eliminate these discrepancies.

5.4.1 Tracking Efficiency

The overall track reconstruction efficiency in the CDC is measured to be 93% while the CDC–VXD linking efficiency is measured to be 96%.[48] These efficiencies are put into the Monte Carlo and the distribution of total number of reconstructed tracks per event in data and Monte Carlo are in good agreement. However, after the track selection procedure (see sec. 5.3), there are fewer good tracks per event in the data ($N_{\rm good}^{\rm data}$) than in the Monte Carlo ($N_{\rm good}^{\rm MC}$), as demonstrated in figure 5.7. This loss of tracks is related to the Monte Carlo's optimistic simulation of the CDC track quality, although this phenomenon is not understood in detail. In order to account for this effect, tracks are randomly discarded from the Monte Carlo according to the tracking efficiency, $\varepsilon_{\rm trk}$, which gives the best fit between the $N_{\rm good}^{\rm data}$ and $N_{\rm good}^{\rm MC}$ plots. This efficiency is determined by scanning through a range of $\varepsilon_{\rm trk}$ and computing the χ^2 at each scan point. A rough scan (see figure 5.8) indicates approximately where the best $\varepsilon_{\rm trk}$ is. Then a fine scan (see figure 5.9) around the approximate minimum pinpoints the proper $\varepsilon_{\rm trk}$ and its uncertainty. The results of the fine scan are:

$$\varepsilon_{\rm trk} = 90.5\% \pm 0.7\% \tag{5.15}$$

This value is in agreement with the rough scan, and varying the limits of the scan does not significantly change the results.

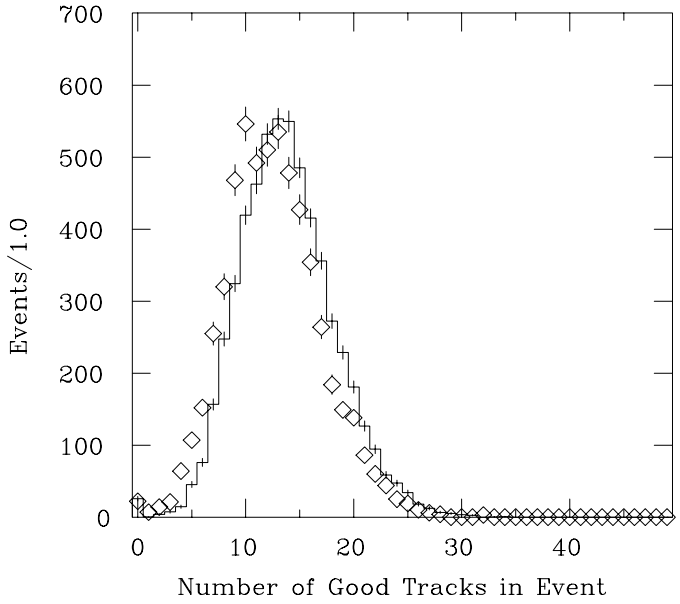

Figure 5.7: N_{good} for data ($\diamond$) over uncorrected Monte Carlo (histogram)

5.4.2 Tracking Resolution

The tracking resolution is not adequately modeled for our purposes. This is a combination of several factors including unrealistically small amounts of material in the GEANT model and the use of a gaussian approximation for multiple scattering. As a result, the tails of the impact parameter distribution are underestimated in the Monte Carlo (see fig. 5.13). Following the technique pioneered by Jacobsen,[75] we add *ad hoc* smearing to all Monte Carlo tracks in an effort to force agreement between the Monte Carlo and the data. The magnitude and shape of the smearing are determined by comparing the distribution of negative impact parameters* for the data and the Monte Carlo. We use tracks with negative impact parameters that are otherwise well–measured (so–called *good fakes*) since it is expected that these are primary tracks

*For details on how the impact parameters are given a sign, please see section 4.3.4.

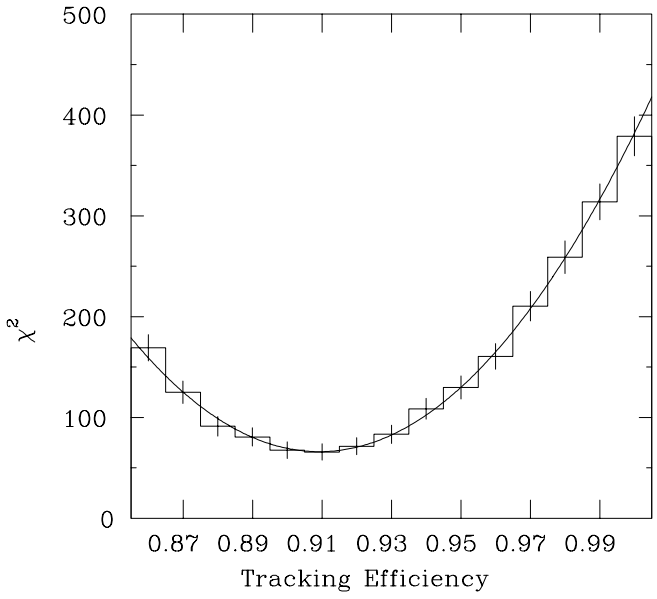

Figure 5.8: Rough scan to find $\varepsilon_{\mathrm{trk}}$

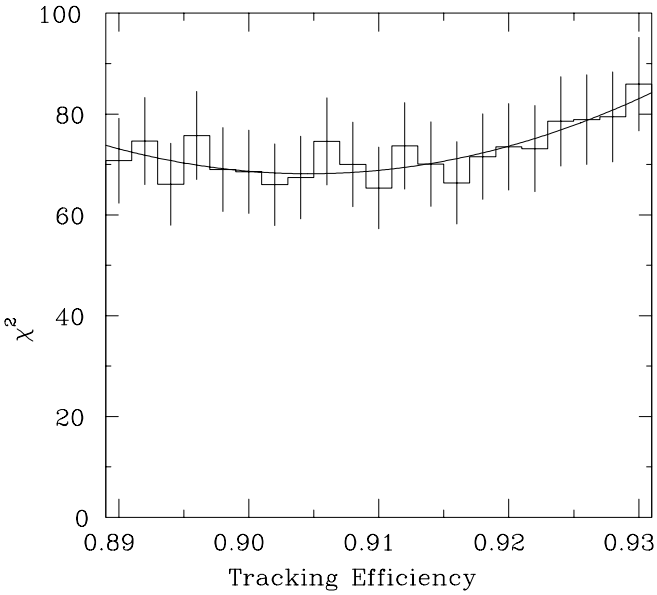

Figure 5.9: Fine scan to find $\varepsilon_{\mathrm{trk}}$

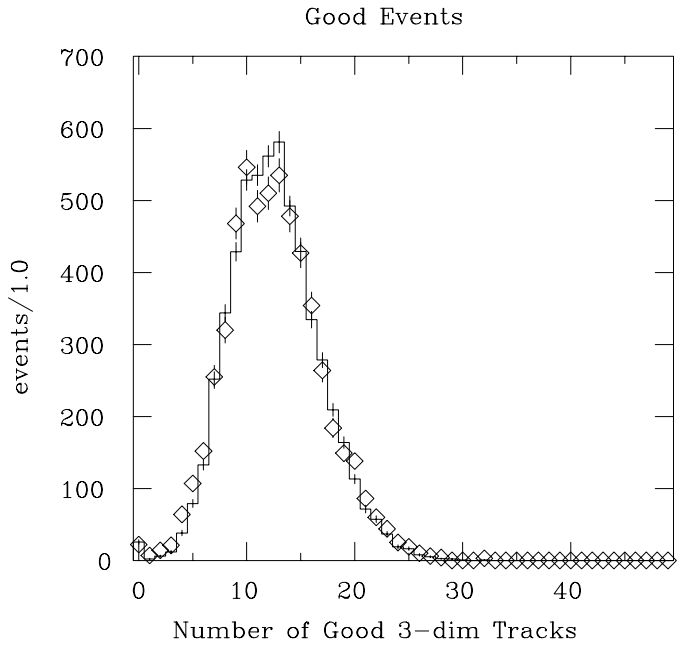

Figure 5.10: $N_{\mathbf{good}}$ for data ($\diamond$) over Monte Carlo (histogram) after correcting for $\varepsilon_{\mathbf{trk}}$

whose deviation from zero is entirely due to tracking resolution. This assumption has been studied and found true for the core and near tail of the distribution.[76] The far tail is dominated by tracks from heavy quark decay products.

There are two types of smearing that are needed to correct the tracking resolution. We apply a scale factor (S_b) to all tracks in order to adjust the mean (the width does not require correction). We also add a "large smear" to a few percent of the tracks which increases the size of the tail. The large smear distribution is the positive half of a gaussian with width σ_{lrg} and the fraction of tracks that receive a large smear is called ν_{lrg}. Since the tracking resolution is a strong function of p_t we divide the tracks into six ranges of p_t and optimize the smearing parameters for each range. We expect the parameters to change rapidly at low p_t but to remain fairly constant at high p_t, hence we chose narrower p_t ranges at the low end and wide ranges at the high end. The following p_t ranges are used: (1) $p_t \leq 0.5$ GeV/c, (2) $p_t \in (0.5, 1.0]$ GeV/c, (3) $p_t \in (1.0, 1.5]$ GeV/c, (4) $p_t \in (1.5, 2.0]$ GeV/c, (5) $p_t \in (2.0, 5.0]$ GeV/c and (6) $p_t > 5.0$ GeV/c. All six ranges contain approximately the same number of tracks.

When determining the smearing parameters it is convenient to divide the tracks

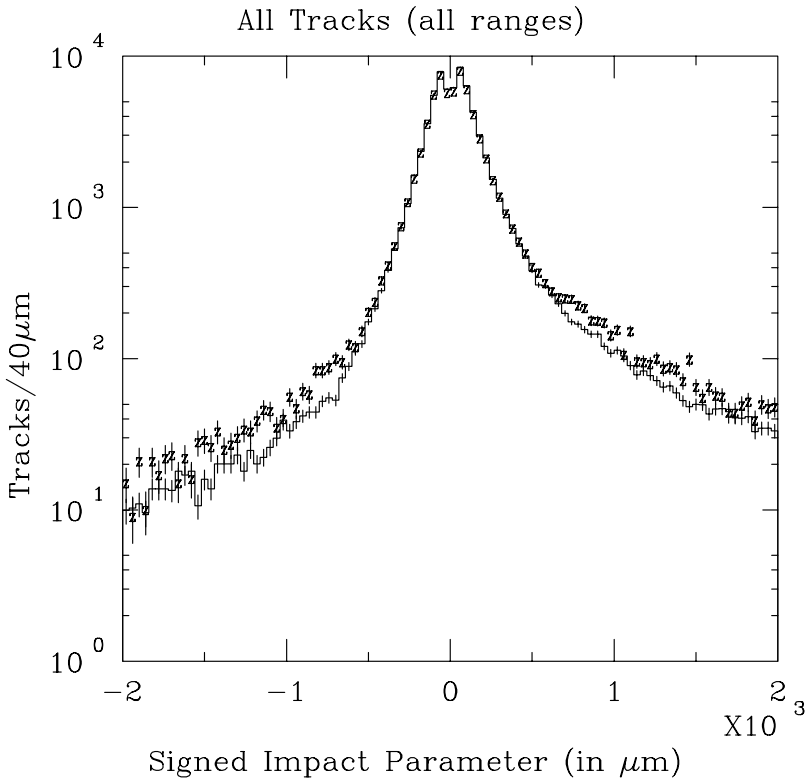

Figure 5.11: Signed impact parameter for all good tracks.
Data (Z) over uncorrected Monte Carlo (histogram).

within each p_t range once again. We define the *core* of the distribution to be the $\sim 80\%$ of the tracks with the smallest (unsigned) impact parameter. The *tail* is the rest of the tracks, excluding the $\sim 1\%$ with the largest impact parameter.

The core distributions for different p_t ranges (see fig. 5.14) demonstrate clearly the need for a scale factor. Such a scale factor would multiply the impact parameters in the Monte Carlo, shifting the distributions up or down. As these distributions represent the tracking resolution which is parametrized by the expected uncertainty in the impact parameter (σ_b), σ_b should also be scaled by the same factor in the Monte Carlo. Since σ_b is a calculated quantity rather than a measured one, the same scale factor should be applied to σ_b in the data.

The need for a scale factor is believed to come from GEANT's gaussian approximation of multiple scattering and our omission of some material from the GEANT model. On average, the gaussian approximation leads to a core impact parameter

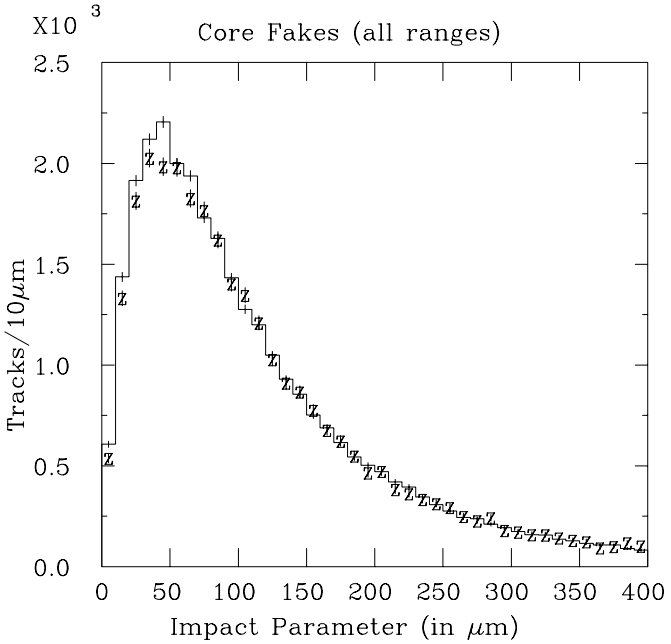

Figure 5.12: Impact parameter for core "good fake" tracks. Data (Z) over uncorrected Monte Carlo (histogram).

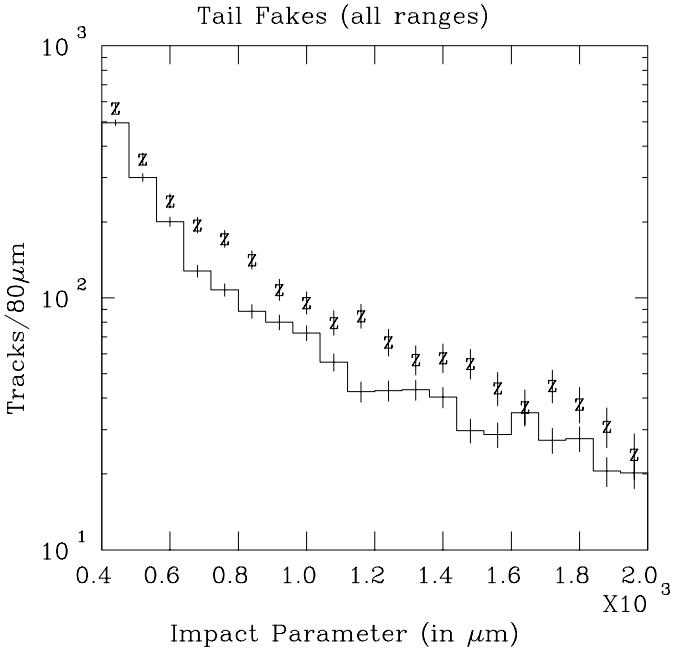

Figure 5.13: Impact parameter for tail "good fake" tracks. Data (Z) over uncorrected Monte Carlo (histogram).

distribution that is slightly high while the missing material leads to a distribution that is slightly low. This combination leads to an impact parameter distribution that has the correct core width on average (see fig. 5.12), but the distributions for different p_t ranges are slightly off.

Similarly, the tail distributions (see fig. 5.15) demonstrate the need for a large smear of some type, as the tail in the Monte Carlo is smaller than the tail in the data for all p_t ranges. This discrepancy is believed to come from the multiple scattering tail which is not accurately reproduced by GEANT's gaussian approximation and from misalignment in the VXD. Two other causes dominate the far portion of the tail: mislinked and interaction tracks. Mislinking of VXD hits to CDC tracks becomes problematic when several tracks "want" the same hit. Particles which undergo nuclear interactions or eject δ–rays also lead to linking problems.

Since the three parameters are correlated within each p_t range, it is important to maintain a uniform methodology in determining them. We find the least correlated parameter, S_b, first. Using the core distributions of good fake impact parameters, we scan across a range of S_b calculating the χ^2 between the data and the Monte Carlo for each value of S_b. Then the $\chi^2(S_b)$ distribution is fitted to a parabola (see fig. 5.16). Knowing the minimum and the error on the minimum of this parabola, the procedure is iterated, scanning a range of three sigma around the minimum. This process usually produces a good fit, but as a check another scan is performed at two sigma around this new minimum. The best S_b is that which gives the minimum χ^2, and its error is determined from the $\chi^2_{min} + 1$ points. No large smear is included in this procedure.

To determine the large smear parameters we do a similar procedure, however we must take the correlations between $\nu_{\rm lrg}$ and $\sigma_{\rm lrg}$ into account. Using the scale factor determined above, we scan across $\nu_{\rm lrg}$ for many values of $\sigma_{\rm lrg}$. At each point we calculate the χ^2 between the data and the Monte Carlo distributions of good fake impact parameters in the tail. Fitting the $\chi^2(\nu_{\rm lrg})|_{\sigma_{\rm lrg}}$ distribution gives the best χ^2 for that trial. Because $\nu_{\rm lrg}$ is typically a few percent, the statistical errors on χ^2 are sizable when we use the Monte Carlo information only once. We reduce these errors by repeating this procedure twelve times (with different random number seeds) for

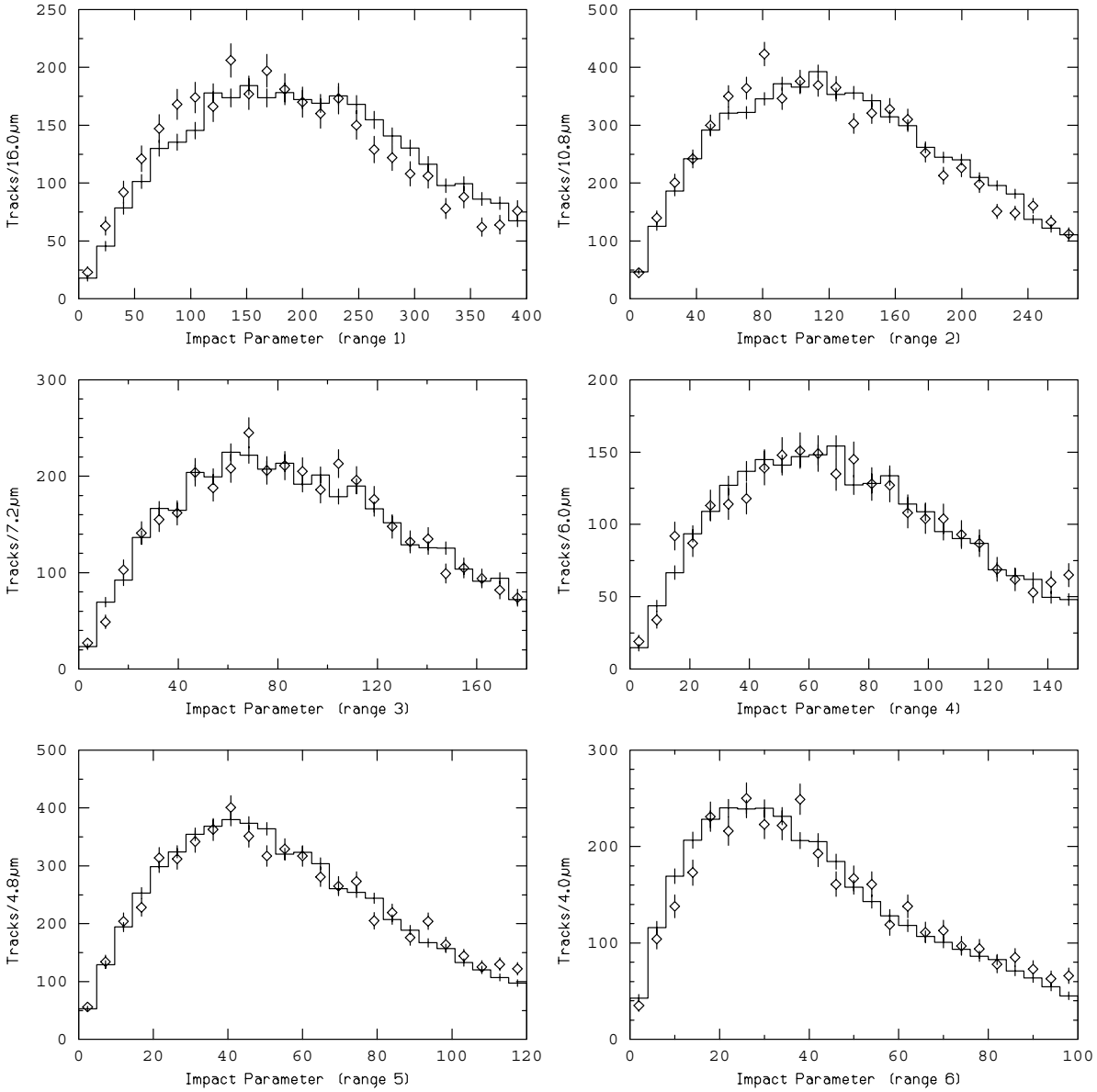

Figure 5.14: Core impact parameter distributions for all six p_t ranges
Data ($\diamond$) over uncorrected Monte Carlo (histogram).

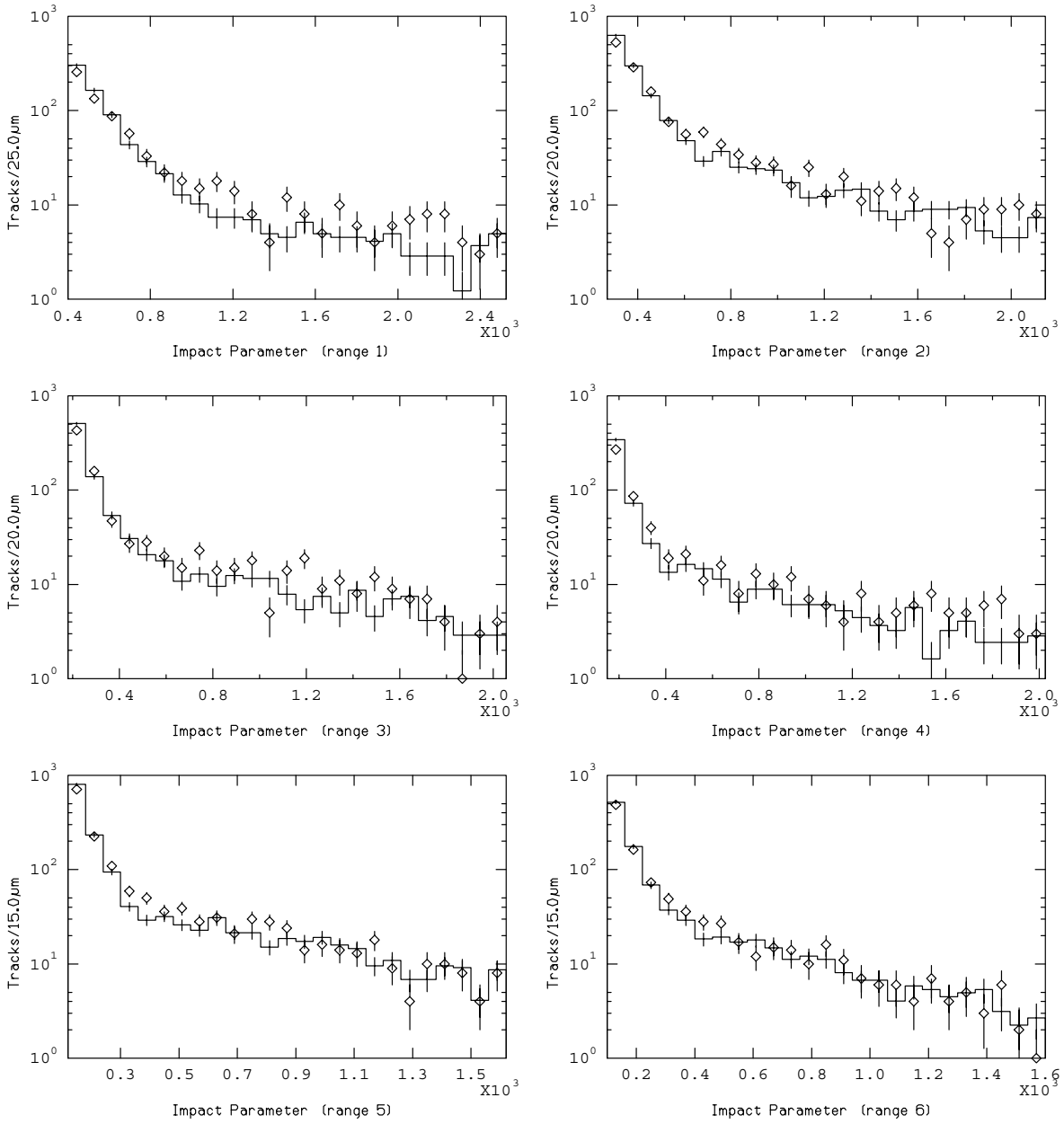

Figure 5.15: Tail impact parameter distributions for all six p_t ranges
Data ($\diamond$) over uncorrected Monte Carlo (histogram).

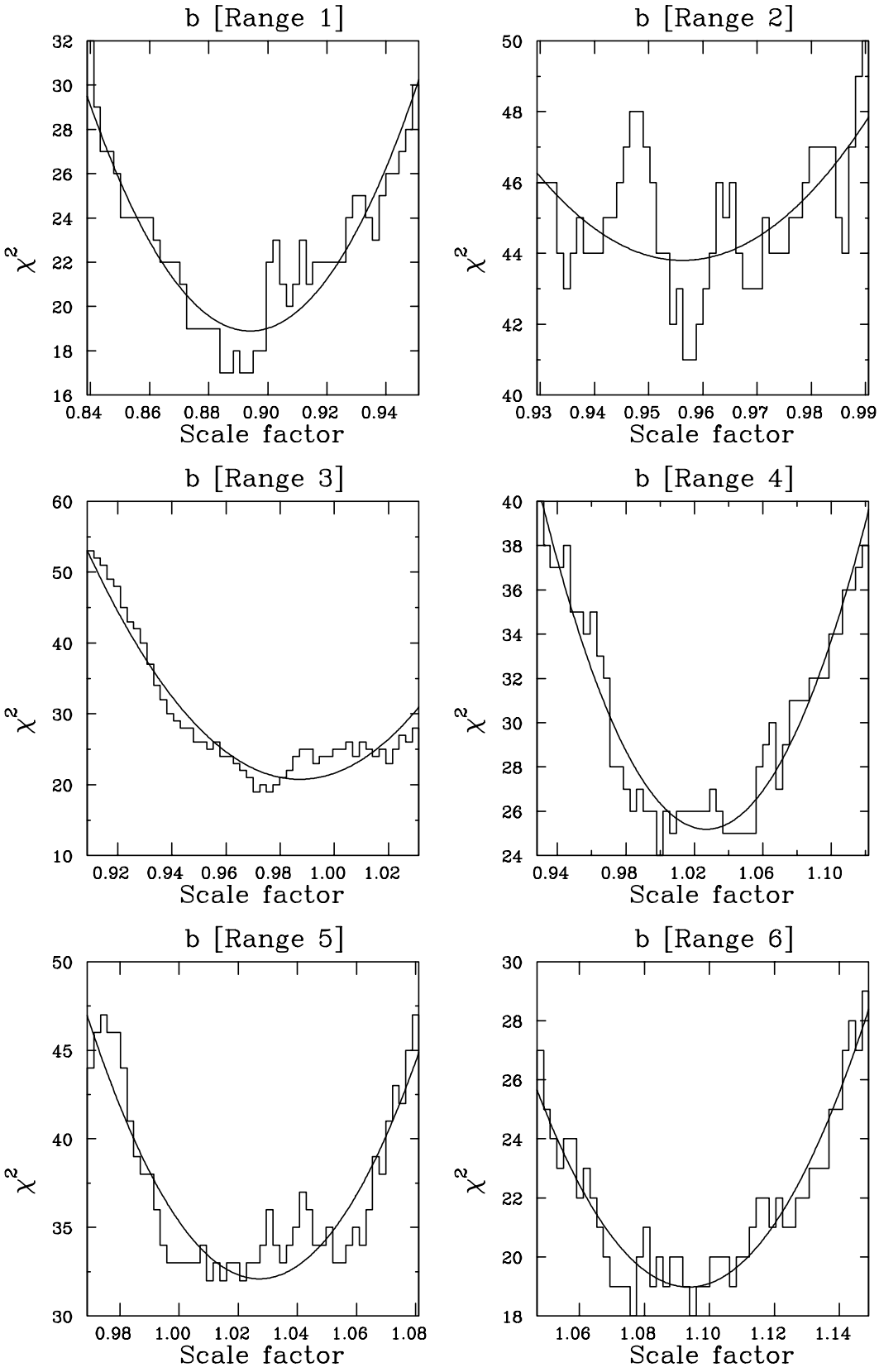

Figure 5.16: $\chi^2(S_b)$ distributions for all six p_t ranges.

each $\sigma_{\rm lrg}$ and averaging the best χ^2 from each trial. Note that the corresponding best $\nu_{\rm lrg}$ for each trial is allowed to float. In this manner we obtain a plot of $\langle \chi^2_{best} \rangle$ vs. $\sigma_{\rm lrg}$. Fitting this plot to a parabola determines the best $\sigma_{\rm lrg}$ parameter and its error. In all cases we investigate the minimum with a finer scan. Such investigation generally does not change the minimum $\sigma_{\rm lrg}$ by much. (See figures 5.17 through 5.22.) Then we scan across $\nu_{\rm lrg}$ at this best $\sigma_{\rm lrg}$. Again we average the best $\nu_{\rm lrg}$ over twelve different random number seeds, but the standard deviation of those trials is always small compared to their average error. The final results are listed in table 5.2.

p_t range	S_b	$\nu_{\rm lrg}$ (in %)	$\sigma_{\rm lrg}$ (in μm)
1	0.898 ± 0.015	5.06 ± 1.45	477 ± 120
2	0.956 ± 0.017	3.50 ± 0.88	478 ± 74
3	0.987 ± 0.014	2.35 ± 0.77	994 ± 278
4	1.029 ± 0.024	3.96 ± 0.97	1160 ± 287
5	1.027 ± 0.015	3.25 ± 0.66	427 ± 85
6	1.094 ± 0.018	2.63 ± 0.76	349 ± 80

Table 5.2: Parameters for tracking resolution corrections.

The smearing parameters that arise from these fits corroborate our assumptions as to the causes of the disagreement between data and Monte Carlo. The scale factor is well above unity for the highest p_t range, well below unity for the lowest p_t range and varies monotonically in between. At low momentum the multiple scattering term dominates. The core of GEANT's gaussian approximation is wider than the core of the real multiple scattering distribution, thus the scale factor must compensate by reducing the average impact parameter. At high momentum, the dominant factor is our omission of the titanium beampipe liner from the GEANT model, hence the scale factor must increase the average impact parameter accordingly. In the middle p_t ranges the two effects tend to cancel, so the scale factor is close to unity.

The large smear compensates for two problems. In the two lowest and two highest p_t ranges the dominant problem is the uncertainties in the ladder–to–ladder z alignment of the VXD, which are of order $400\,\mu$m. This leads directly to large smearing widths of about the same size. The fraction of tracks which require this large smear are greatest at low momentum and decrease with increased momentum, since at high

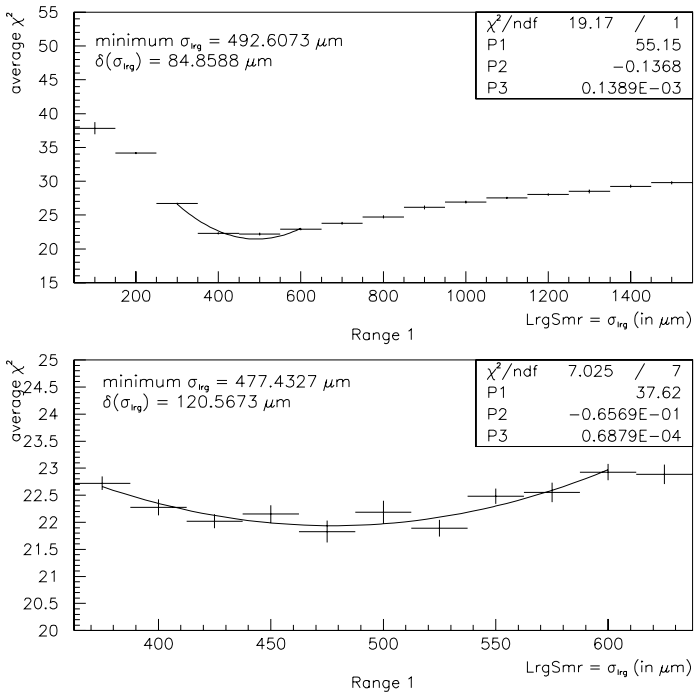

Figure 5.17: $\langle \chi^2 \rangle$ vs. σ_{lrg} distribution for $p_t \leq 0.5\,\mathrm{GeV}/c$.

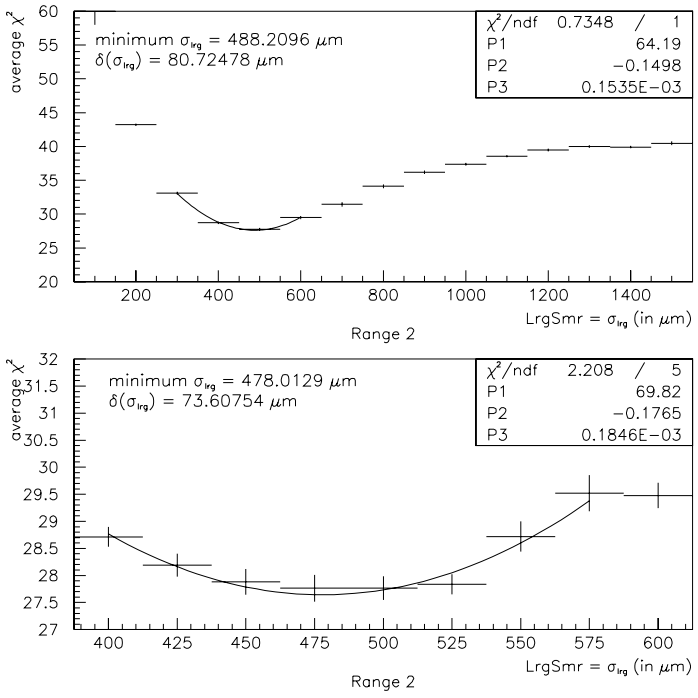

Figure 5.18: $\langle \chi^2 \rangle$ vs. σ_{lrg} distribution for $0.5 < p_t \leq 1.0\,\mathrm{GeV}/c$.

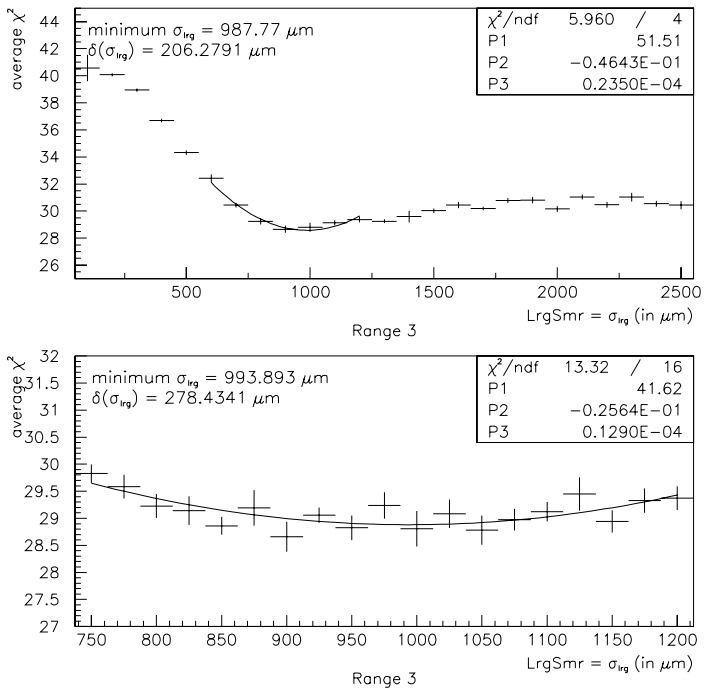

Figure 5.19: $\langle \chi^2 \rangle$ vs. σ_{lrg} distribution for $1.0 < p_t \leq 1.5\,\mathrm{GeV}/c$.

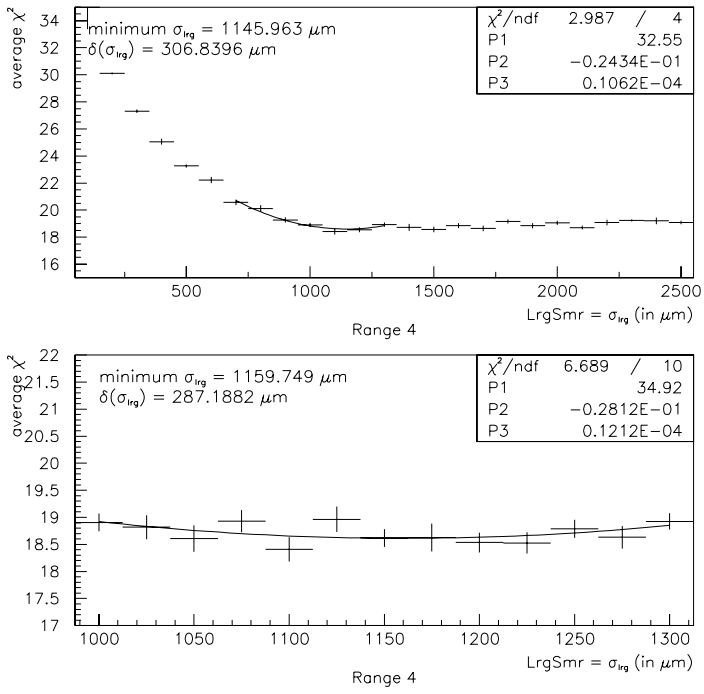

Figure 5.20: $\langle \chi^2 \rangle$ vs. σ_{lrg} distribution for $1.5 < p_t \leq 2.0\,\mathrm{GeV}/c$.

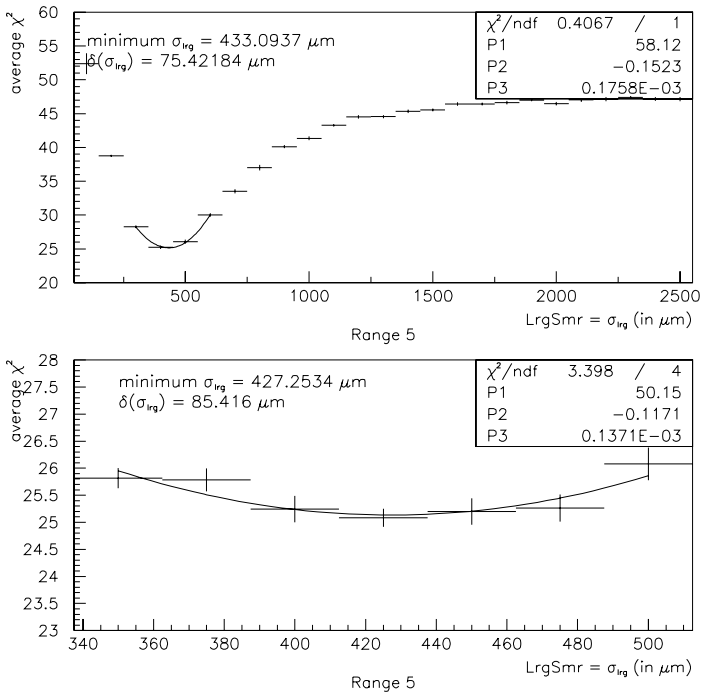

Figure 5.21: $\langle\chi^2\rangle$ vs. σ_{lrg} distribution for $2.0 < p_t \leq 5.0$ GeV/c.

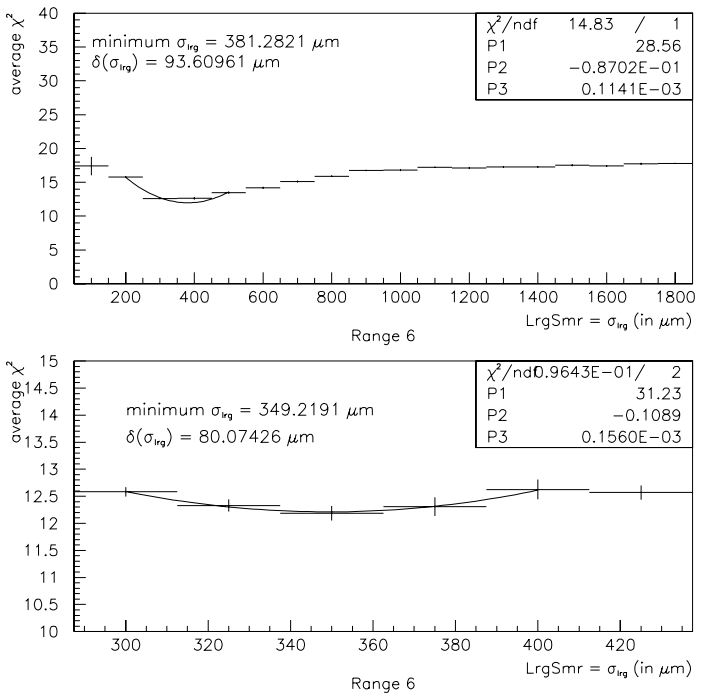

Figure 5.22: $\langle\chi^2\rangle$ vs. σ_{lrg} distribution for $p_t > 5.0$ GeV/c.

momentum hits on misaligned ladders tend to fall outside the search area for CDC–VXD linking and are discarded. In the middle two p_t ranges, the dominant problem is mislinked tracks. With mislinking, the miss distance is not clearly defined so we would expect the uncertainty on $\sigma_{\rm lrg}$ to be large.

5.5 Backgrounds

There are many physics processes other than $Z^0 \to q\bar{q}$ which could mistakenly be counted as hadronic Z^0 decays. These backgrounds can be classified into four groups: leptonic Z^0 decays, photon interactions, beam–related and cosmic ray. The hadronic event filter removes many of the backgrounds on the basis of energy imbalance. The event selection procedure removes nearly all of the rest by requiring seven charged tracks.

5.5.1 Leptonic Z^0 Backgrounds

The Z^0 boson has a large partial width into each lepton and neutrino species. While we are obviously not sensitive to the neutrino channels, we are sensitive to the $\ell^{\pm}$ channels. Both $Z^0 \to e^+e^-$ and $Z^0 \to \mu^+\mu^-$ events will be removed because of the track requirement, but some of the $Z^0 \to \tau^+\tau^-$ events will not be removed. To approximate how many $Z^0 \to \tau^+\tau^-$ events will contaminate our event sample, we generated a sample of $10,000$ $Z^0 \to \tau^+\tau^-$ events and subjected them to the same event selection process to which the hadronic Monte Carlo events are subjected. A total of 139 $Z^0 \to \tau^+\tau^-$ events passed the event selection and 18 of those were tagged as $b\bar{b}$ events. These numbers vary with the choice of track and significance cuts, but the variation is small compared with the statistical error.

In our data sample of $10,437$ $Z^0 \to q\bar{q}$ events we would expect $496 \pm 22_{(\rm stat.)} \pm 6_{(\rm Br)} = 496 \pm 23$ $Z^0 \to \tau^+\tau^-$ events.[†] In reality, we know that this is an upper limit since our data sample contains some non–hadronic background. Thus the number of

[†] Using the measured value of $\Gamma(Z^0 \to \tau^+\tau^-)/\Gamma(Z^0 \to q\bar{q}) = 4.76\% \pm 0.06\%$.[6]

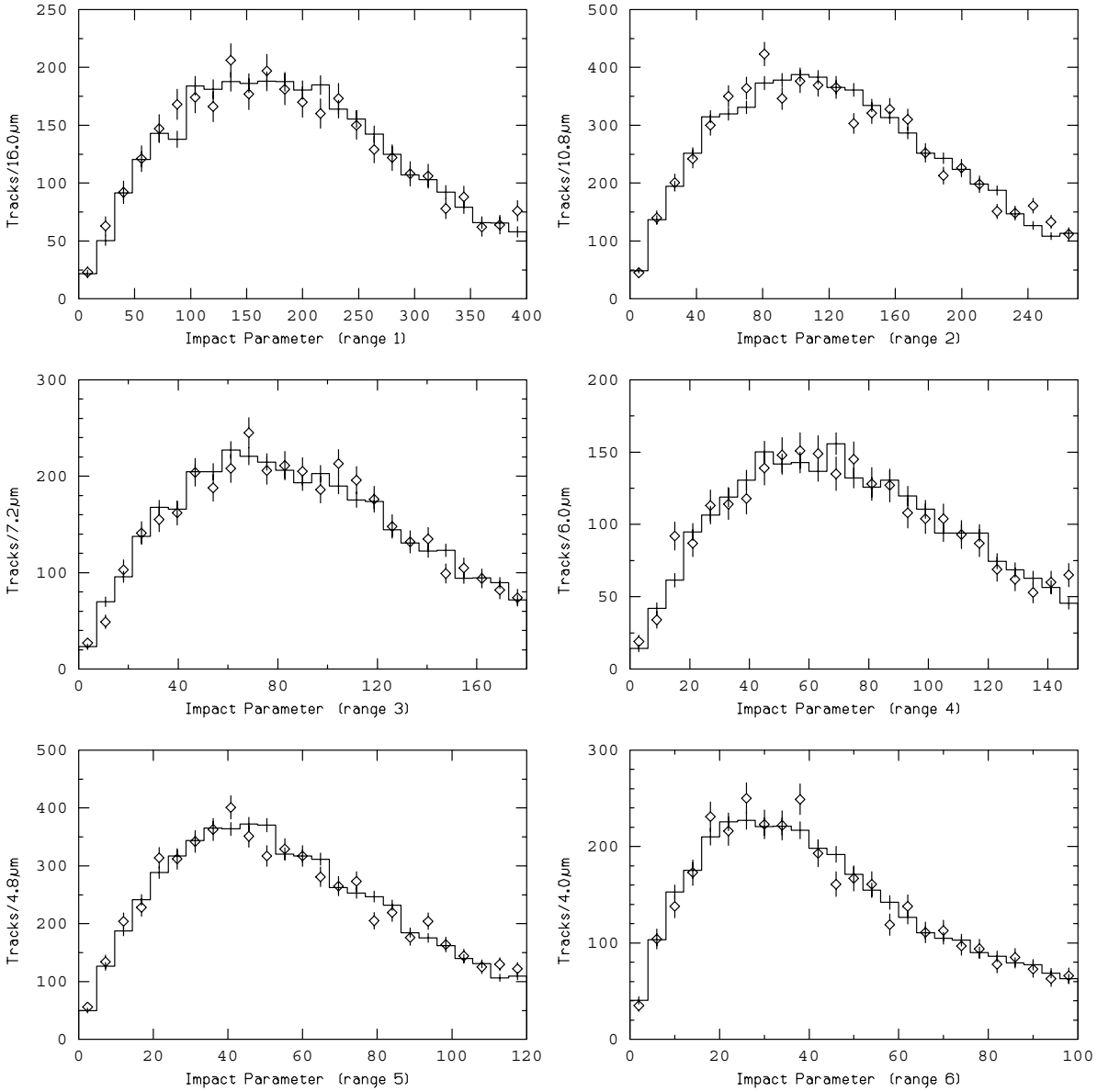

Figure 5.23: Core impact parameter distributions for all six p_t ranges
Data ($\diamond$) over smeared Monte Carlo (histogram).

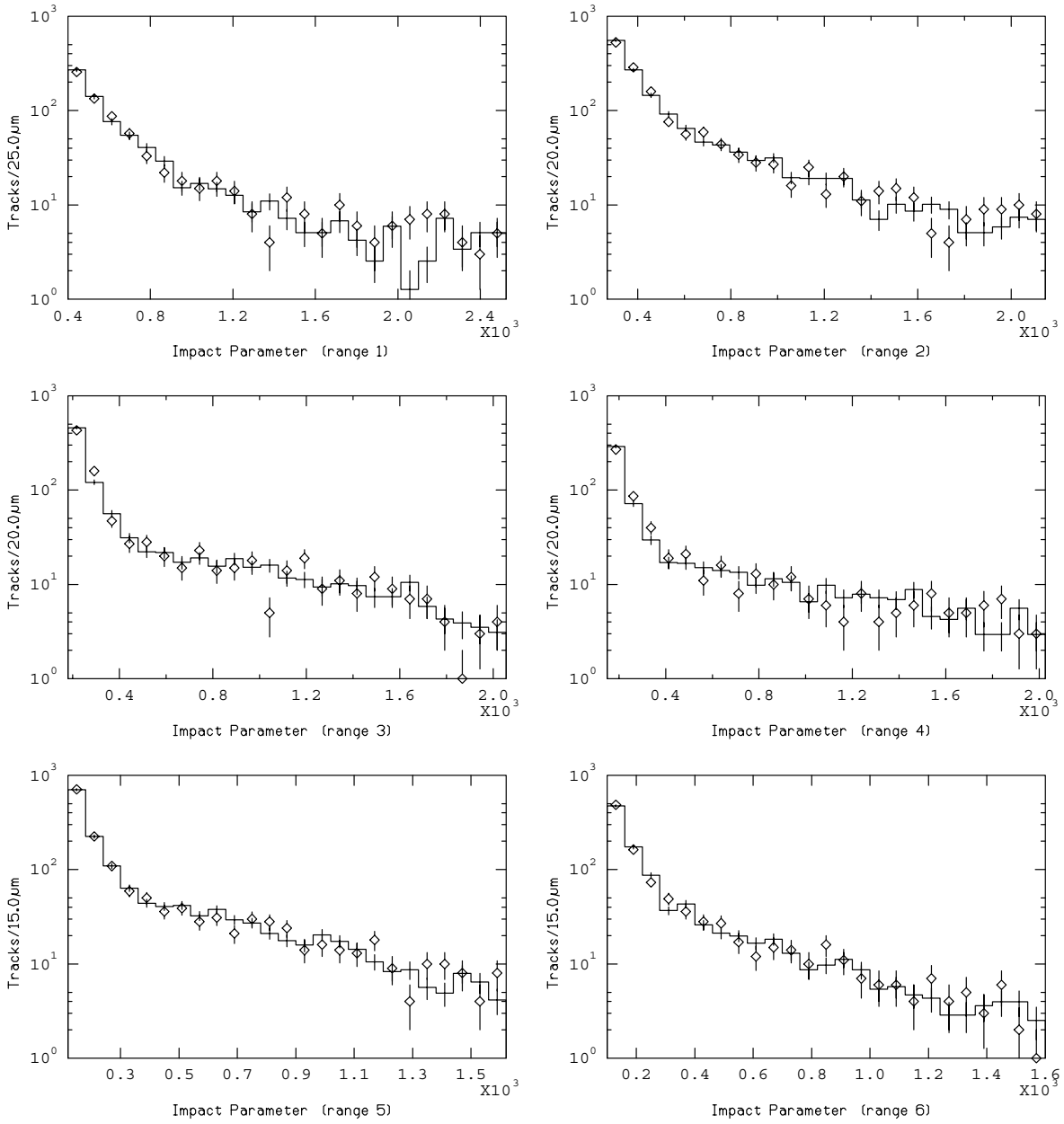

Figure 5.24: Tail impact parameter distributions for all six p_t ranges
Data ($\diamond$) over smeared Monte Carlo (histogram).

$Z^0 \to \tau^+\tau^-$ events passing the hadronic event selection is:

$$N_{\mathrm{back},\tau} \lesssim \left[\frac{139 \pm 12}{10,000}\right](496 \pm 23) = 6.9 \pm 0.7 \tag{5.16}$$

The number tagged as $b\bar{b}$ events is:

$$T_{\mathrm{back},\tau} \lesssim \left[\frac{18 \pm 4}{10,000}\right](496 \pm 23) = 0.9 \pm 0.2 \tag{5.17}$$

5.5.2 Photon Interaction Backgrounds

There are many $e^+e^- \to X$ processes that occur via photons. Bhabha scattering, "2γ" interactions and "$\gamma\gamma$" interactions all use t–channel photons. These $e^+e^- \to X$ processes have been studied[73] and found to be negligible. Very few of these events are balanced enough to pass the filter, and those events that pass the filter do not have enough tracks to pass the event selection. S–channel photons and the γ–Z^0 interference term lead to events that are indistinguishable from Z^0 decays, yet they should be considered background. At our energy ($\sqrt{s} = 91.55$ GeV), their effect is $\delta R_b/R_b = 0.07\%$.[77] We can safely neglect these backgrounds.

5.5.3 Beam–Related and Cosmic Ray Backgrounds

Beam–related backgrounds emanate from two major sources: muons produced upstream by SLC and beam–gas or beam–wall interactions in the SLD. The SLC muons can be neglected in this analysis since they are parallel to the beam and hence will not create CDC tracks. Beam–gas and beam–wall interactions are mostly eliminated by the energy imbalance cut. Ben–David and Park[73] expect 0.8 ± 0.7 events in our sample to consist of two simultaneous beam interactions which are sufficiently back–to–back to mock a Z^0 event. Similarly, a cosmic ray that showers and passes through the IP would mimic a Z^0 event. Ben–David and Park set an upper limit of 1.4 events of this type in our event sample.

All of the non–tau backgrounds add up to only a small fraction of the $Z^0 \to \tau^+\tau^-$ background.[‡] For this reason we will take the sum of all other backgrounds to be equal

[‡] This proposition is also supported by other analyses (*e.g.*, [78]).

to the number of $Z^0 \to \tau^+\tau^-$ background events with an error of 100%. Therefore the total backgrounds are:

$$N_{\rm back} \lesssim (2 \pm 1) N_{{\rm back},\tau} = 13.8 \pm 7.0 \quad (5.18)$$

$$T_{\rm back} \lesssim (2 \pm 1) T_{{\rm back},\tau} = 1.8 \pm 1.0 \quad (5.19)$$

5.5.4 Effect of Backgrounds

We must now adjust our equation for R_b (equation 5.14) to allow for background subtraction:

$$R_b = \frac{\frac{T_{\rm tot}-T_{\rm back}}{N_{\rm tot}-N_{\rm back}} - (\epsilon_c - \epsilon_{uds})R_c - \epsilon_{uds}}{(\epsilon_b - \epsilon_{uds})} \quad (5.20)$$

The systematic uncertainties on R_b from non–hadronic background events can be derived from this equation and are given by:

$$\sigma_{\rm Rb}(N_{\rm back}) = \sigma_{N_{\rm back}} \left[\frac{T_{\rm tot} - T_{\rm back}}{(N_{\rm tot} - N_{\rm back})^2 (\epsilon_b - \epsilon_{uds})} \right] \quad (5.21)$$

$$\sigma_{\rm Rb}(T_{\rm back}) = \sigma_{T_{\rm back}} \left[\frac{1}{(N_{\rm tot} - N_{\rm back})(\epsilon_b - \epsilon_{uds})} \right] \quad (5.22)$$

These uncertainties are small; even if we add them together assuming no correlation, the total is only:

$$\frac{\sigma_{\rm Rb}}{R_b}({\rm back}) = 0.20\% \quad (5.23)$$

Chapter 6

Results

This chapter presents the results of our R_b measurement. The statistical and systematic uncertainties associated with this measurement are also presented. Finally, the results are interpreted in terms of the minimal standard model and new physics.

6.1 R_b

R_b is calculated using equation 5.20. The data determines $\mathrm{T_{tot}}$ and $\mathrm{N_{tot}}$, while R_c is taken from other experiments. The Monte Carlo determines the efficiencies. Since there are fluctuations in the efficiencies due to the random number seed used in the smearing routine, it is necessary to average the efficiencies over many different seeds. Figure 6.1 shows the tagging efficiencies for the different quark species as functions of the significance cut for a three–track requirement. It is convenient to compare tagging methods by examining the b–tagging efficiency and the b–tagging purity. The three tagging purities are calculated based on the three tagging efficiencies, calculated R_b and previously measured R_c:

$$\Pi_q = \frac{\epsilon_q R_q}{\epsilon_b R_b + \epsilon_c R_c + \epsilon_{uds}(1 - R_b - R_c)} \tag{6.1}$$

Figure 6.2 shows the tagging purities as functions of the significance cut for a three–track requirement. Another way to analyze the effect of the cuts is to plot b–purity

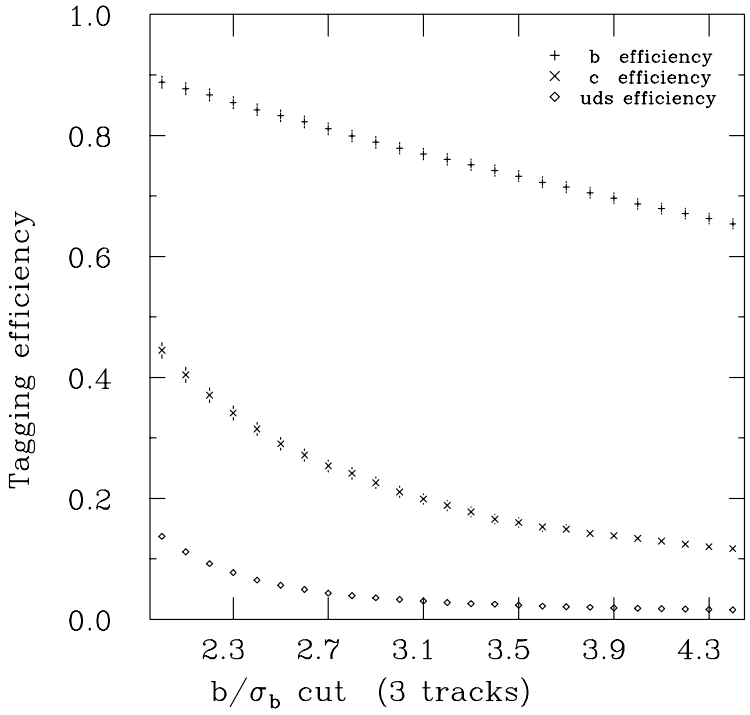

Figure 6.1: Tagging efficiencies from the Monte Carlo (MC stat. errors only).

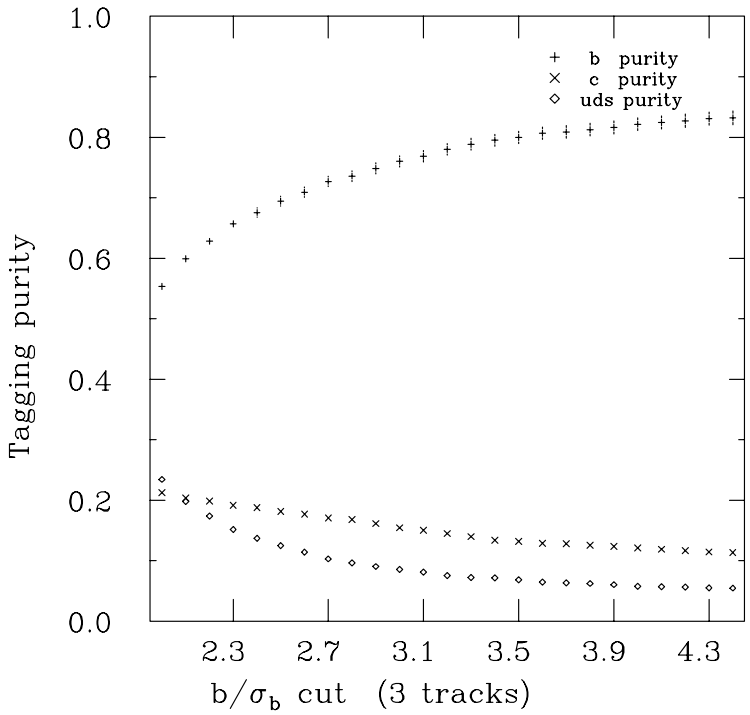

Figure 6.2: Tagging purities from the Monte Carlo (MC stat. errors only).

versus b–efficiency for a range of significance cuts and several different track requirements. This plot is shown in figure 6.3. In all cases the errors reported are entirely due to Monte Carlo statistics.

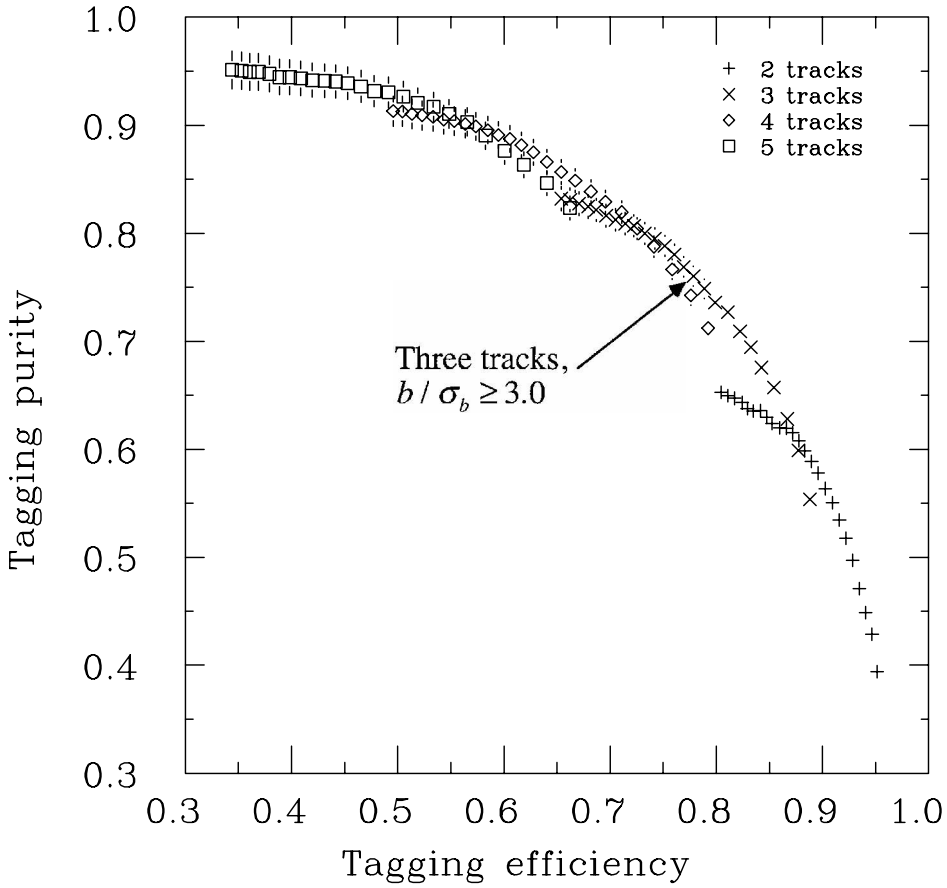

Figure 6.3: Π_b as a function of ϵ_b (MC stat. errors only). Different curves are from different track requirements, significance cut is the variable along each curve.

This analysis uses a significance cut of 3.0 and a three–track requirement because this point (indicated in fig. 6.3) is located on the "knee" of the Π_b *vs* ϵ_b plot.* As we shall see later in this chapter, the total error is minimized near that point. Using this choice of cuts we obtain:

$$N_{\rm tot} \;=\; 5764 \tag{6.2}$$

*As a rule of thumb, we expect the best result to be at the point where the product of these two quantities, $\Pi_b \cdot \epsilon_b$, is maximized.

$$T_{\rm tot} = 1338 \tag{6.3}$$

The tagging efficiencies here are:

$$\epsilon_b = 0.7785 \pm 0.0096_{\rm (MCstat)} \tag{6.4}$$

$$\epsilon_c = 0.2107 \pm 0.0090_{\rm (MCstat)} \tag{6.5}$$

$$\epsilon_{uds} = 0.0329 \pm 0.0019_{\rm (MCstat)} \tag{6.6}$$

The b–purity is:

$$\Pi_b = 0.7601 \pm 0.0093_{\rm (MCstat)} \tag{6.7}$$

Using these values, the background determined in section 5.5 and R_c from equation 5.8, we obtain:

$$R_b = 0.2270 \tag{6.8}$$

Figure 6.4 shows the value of R_b calculated over a sensible range† of the significance cut using several different track requirements. We can see that a variation of the significance cut does not lead to large variations in R_b. Similarly, a variation of the track requirement does not change R_b by more than one standard deviation.

The statistical error can be explicitly calculated using a binomial distribution, since the tagging is a Bernoulli process:

$$\sigma_{\rm Rb}({\rm stat}) = \frac{1}{\epsilon_b - \epsilon_{uds}} \cdot \sqrt{\frac{\left(\frac{T_{\rm tot}}{N_{\rm tot}}\right)\left(1 - \frac{T_{\rm tot}}{N_{\rm tot}}\right)}{N_{\rm tot}}} = 0.0075 \tag{6.9}$$

$$\Rightarrow \frac{\sigma_{\rm Rb}}{R_b}({\rm stat}) = 3.30\% \tag{6.10}$$

The contribution from $N_{\rm back}$ and $T_{\rm back}$ is negligible. We assume that the event selection procedure is unbiased. The systematic error introduced by this assumption will be discussed in section 6.2.3.

† Below a significance of ~ 2.0 the sample is dominated by uds events and tells us little about R_b. Above a significance of ~ 4.5 the far tail dominates the R_b measurement. Since the far tail is not understood and does not have enough statistics to be properly corrected for, significance cuts above 4.5 are not useful.

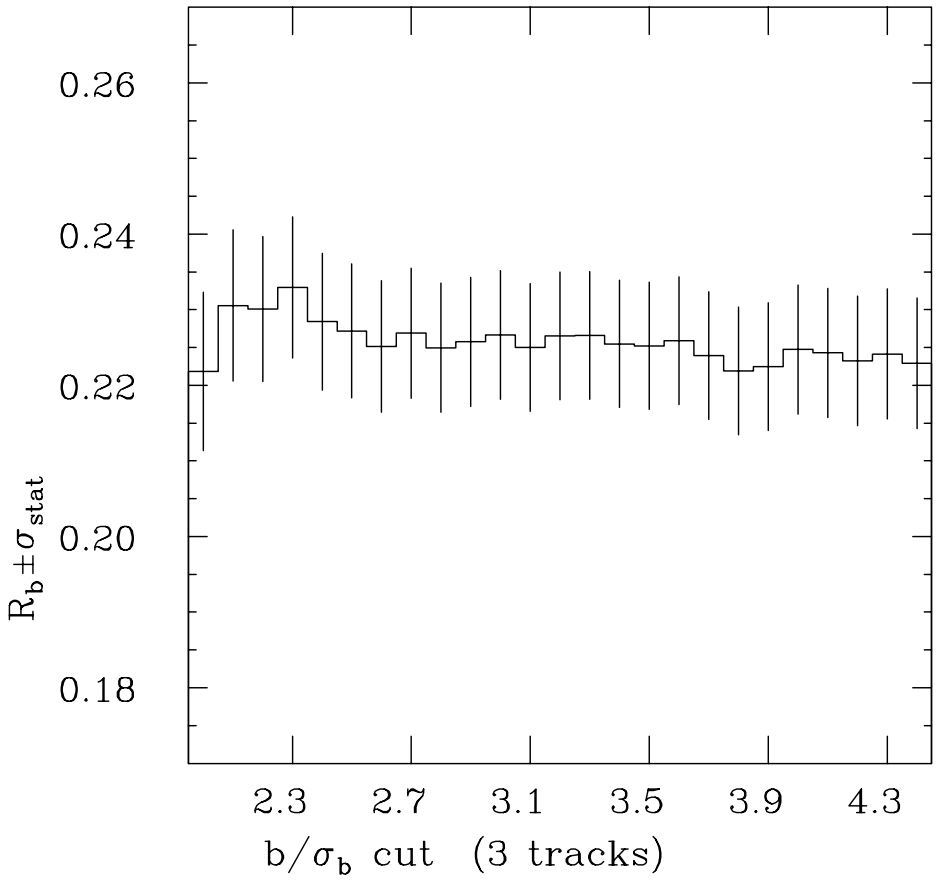

Figure 6.4: R_b as a function of significance cut.
Total error for three–track requirement is shown.

Our Monte Carlo sample is about $23,000$ $q\bar{q}$ events and about $7,000$ $b\bar{b}$ events. The error on R_b due to these limited Monte Carlo statistics can be derived from the R_b formula:

$$\sigma_{\mathrm{Rb}}(\mathrm{MCstat}) = \frac{1}{(\epsilon_b - \epsilon_{uds})}\sqrt{{R_b}^2\sigma^2_{\epsilon_b} + {R_c}^2\sigma^2_{\epsilon_c} + (1 - R_b - R_c)^2\sigma^2_{\epsilon_{uds}}}$$
$$= 0.0039 \quad (6.11)$$
$$\Rightarrow \frac{\sigma_{\mathrm{Rb}}}{R_b}(\mathrm{MCstat}) = 1.72\% \quad (6.12)$$

The error due to choice of random number seed for the smearing routine is negligible since we have averaged over 100 trials. The standard deviation of the mean

is:

$$\sigma_{\mathrm{Rb}}(\mathrm{MCseed}) = 0.00017 \tag{6.13}$$

$$\Rightarrow \frac{\sigma_{\mathrm{Rb}}}{R_b}(\mathrm{MCseed}) = 0.075\% \tag{6.14}$$

thus we shall ignore this error.

The error from uncertainty in R_c is technically a physics systematic error, but it can be explicitly calculated:

$$\sigma_{\mathrm{Rb}}(R_c) = \left|\frac{\epsilon_c - \epsilon_{uds}}{\epsilon_b - \epsilon_{uds}}\right| \sigma_{\mathrm{Rc}} = 0.0040 \tag{6.15}$$

$$\Rightarrow \frac{\sigma_{\mathrm{Rb}}}{R_b}(R_c) = 1.79\% \tag{6.16}$$

6.2 Systematic Error

Systematic uncertainties on the R_b measurement fall into two broad categories: detector resolution and physics modeling.

6.2.1 Detector Resolution

The SLD is modeled well in our Monte Carlo. However, the simulation never corresponds exactly to reality, and the Monte Carlo must be improved constantly in order to produce increasingly accurate approximations of reality. For this analysis, the standard SLD track reconstruction was not sufficient to model the impact parameters and we had to add *ad hoc* smearing.[‡] The uncertainties in this procedure contribute directly to the uncertainty in R_b. Each of the three smearing variables is calculated (with uncertainties) for each of the six smearing ranges, resulting in eighteen smearing parameters.[§] For each parameter, the analysis is repeated twice, once increasing the parameter by one sigma, the second time decreasing it by the same amount. We then find the RMS average deviation in R_b for each parameter. We make the assumption that all the parameters are uncorrelated; hence we can compute the

[‡] See section 5.4.2.

[§] See table 5.2.

total systematic uncertainty by adding all the errors in quadrature. The tracking efficiency is also a detector resolution parameter. Its effect is calculated similarly and included in the sum. A plot of the detector resolution errors for a three–track requirement is shown in figure 6.5. For a significance cut of 3.0 and a three–track requirement, the errors are given in table 6.1 To properly interpret these errors it is necessary to know the size of the full corrections from each variable. The scale factor leads to a small ($\sim$ 1.9%) effect, but it is not known better than 50%. The large smearing leads to a 9.2% correction, and the large smear parameters are known to about 10%. The additional tracking inefficiency is a 10.9% effect, and it is also known to about 10%.

Systematic	Absolute Error	Fractional Error
S_b	0.0026	1.15%
$\nu_{\rm lrg}$	0.0022	0.98%
$\sigma_{\rm lrg}$	0.0008	0.34%
$\varepsilon_{\rm trk}$	0.0019	0.86%
Total	0.0040	1.77%

Table 6.1: Detector resolution errors.

6.2.2 Physics Modeling

Not all of the Monte Carlo's input parameters are significant to this analysis. Moreover, many of them affect the same observable which has been tuned to the measured value. Therefore, we choose a limited set of parameters (some observable, some not) to investigate as physics modeling errors. For example, the average charged track multiplicity for $B\overline{B}$ pairs is known to about 0.5 tracks/event. The branching ratios for the various B_s^0 decay modes are not known to any significant degree. Instead of varying all of the B_s branching ratios in an effort to vary the charged multiplicity, we use a simple weighting method to adjust the average multiplicity.

The parameters used in this manner are: the Peterson fragmentation parameter for b quarks ($\varepsilon_{\rm B}$), the similar parameter for c quarks ($\varepsilon_{\rm C}$), the average charged track multiplicity for $B\overline{B}$ pairs and the B lifetime. One could easily add more parameters to this list, but the tuning of the Monte Carlo leads to correlations between most of the

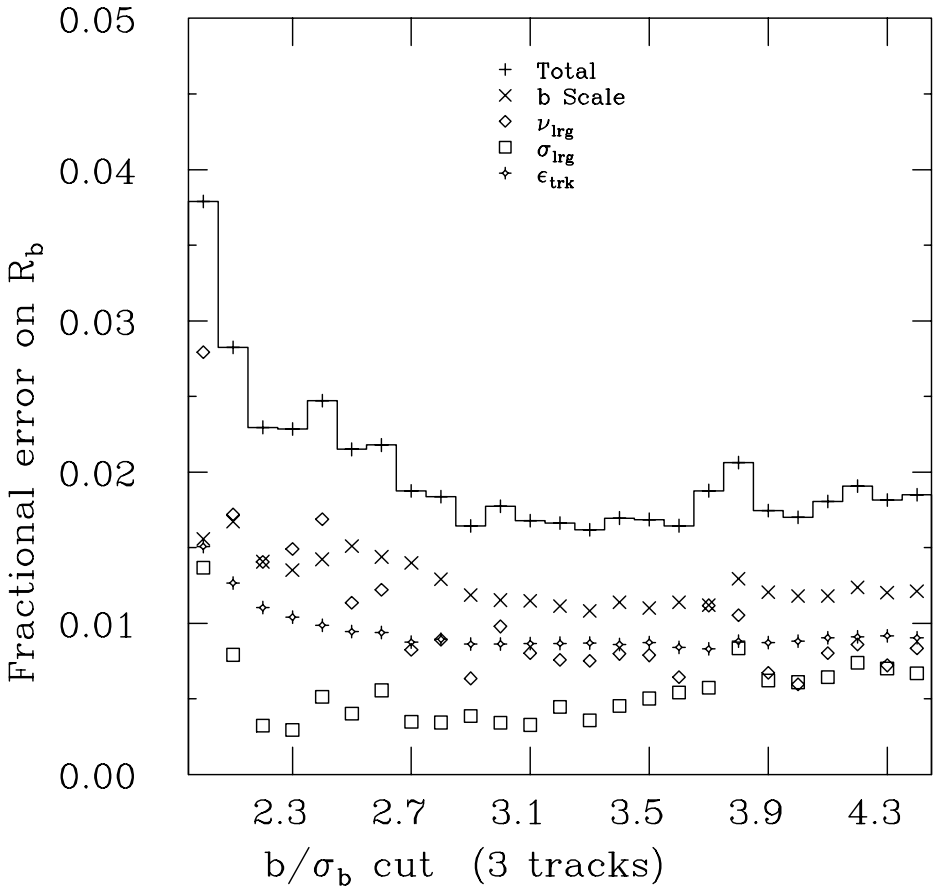

Figure 6.5: Detector resolution errors as a function of significance cut.

parameters in the Monte Carlo. Investigation of many parameters would necessitate accounting for their correlations. By using fewer parameters and ignoring any possible correlations, we hope to obtain an error that is not grossly overestimated.

The weighting routine looks at observables in each event and determines the probability that an event with identical observables would have occurred if the Monte Carlo had been run with one of the above parameters adjusted. This is accomplished in a resonable amount of computer time by making two approximations: (i) All the observables that are compared are investigated at the generator level, relieving us of the need to fully simulate and reconstruct all of the events. (ii) The observables are binned into bins of moderate size. For the B lifetime, an exact weight can be calculated, as the generated lifetime and the desired lifetime are known.

As an example, take a $c\bar{c}$ event that contains two primary charmed hadrons of energy 21.3 GeV and 27.8 GeV. The probability that a hadron with energy between 20 and 22 GeV would be created if the Peterson fragmentation parameter were low, $\varepsilon_C = 0.03$ (instead of the tuned value, 0.06), is 0.8917. The similar probability for a hadron with energy between 26 and 28 GeV is 1.0018. Therefore, this event has a weight of $0.8917 \times 1.0018 = 0.8933$ for "hard $c\bar{c}$ fragmentation," indicating that this event is less likely to occur if ε_C were low. Similarly, the "soft $c\bar{c}$ fragmentation" weight is $1.0596 \times 0.9673 = 1.0250$. Since this event contains no b hadrons, the other weights are all unity.

The systematic effect of the uncertainty in R_c can be calculated explicitly from the formula for R_b, hence that uncertainty has already been discussed and will be treated as a separate error. A plot of the physics modeling errors for a three–track requirement is shown in figure 6.6. For a significance cut of 3.0 and a three–track requirement the errors are given in table 6.2.

Systematic	Variation	Absolute Error	Fractional Error
b fragmentation	$\varepsilon_B = 0.006^{+0.005}_{-0.003}$	0.0038	1.69%
c fragmentation	$\varepsilon_C = 0.06 \pm 0.03$	0.0009	0.40%
B multiplicity	$\langle N_{trk} \rangle \pm 0.5$	0.0046	2.01%
B lifetime	$\tau_B = 1.45 \pm 0.10$ ps	0.0028	1.25%
Total		0.0067	2.94%

Table 6.2: Physics modeling errors.

The systematic error arising from our choice of algorithm for determining jets and our choice of jet size parameter (y_{cut}) is small and will be neglected.¶ This proposition is supported by other analyses (*e.g.*, [39]) and we will not cover it in detail. The average total multiplicity for hadronic Z^0 decays leads to another systematic error, but it can be neglected when compared to the $Z^0 \to b\bar{b}$ average multiplicity systematic error. Several alternate B decay models have been tried with our standard tuned Monte Carlo. In each case the resulting ϵ_b has been within error of the standard

¶This assumes that the data and Monte Carlo jet finding is done with the same algorithm and parameters and that the smearing parameters are also determined with the new jets. The smearing parameters (and resultant tagging efficiencies) can change significantly with different jets, but the resulting R_b remains stable.

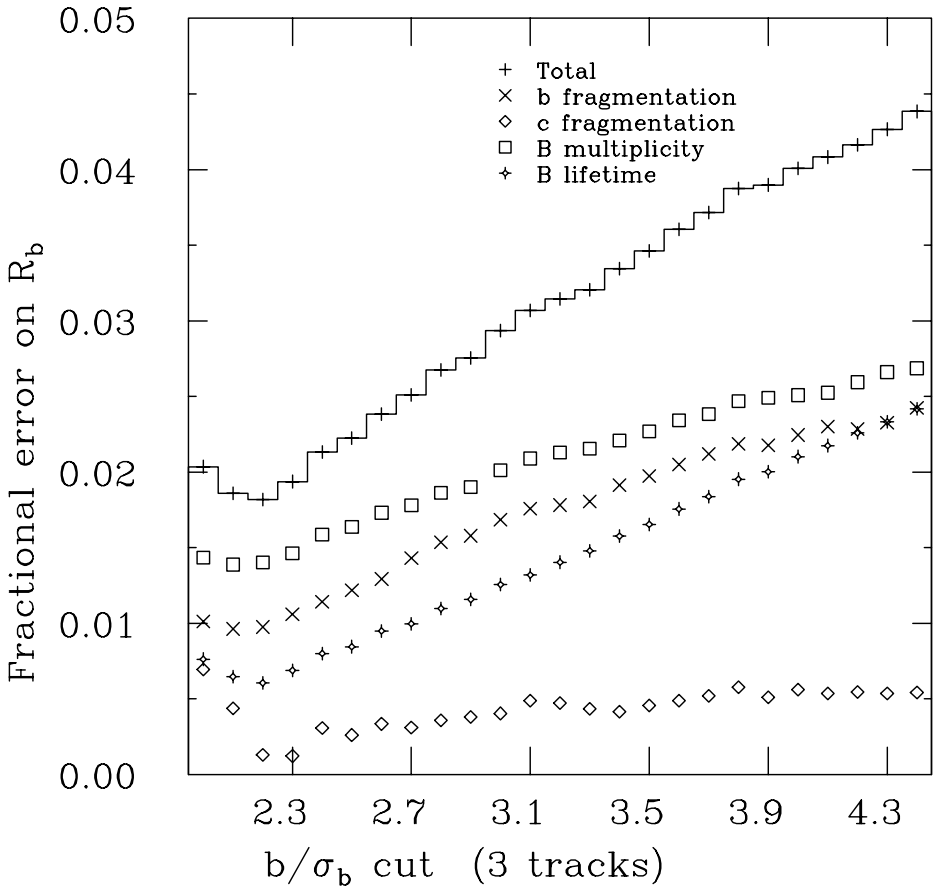

Figure 6.6: Physics modeling errors as a function of significance cut.

value. This suggests that our tuned Monte Carlo is representative of the world average knowledge of B decays and that the errors discussed above are reasonable.

6.2.3 Event Selection Bias

The procedure for event selection could be biased towards one quark flavor. If this were the case it would be necessary to add a correction factor to the R_b formula to compensate for the bias. Let us define the true b–to–hadron ratio as:

$$\frac{\Gamma(\mathrm{Z}^0 \to b\bar{b})}{\Gamma(Z^0 \to \mathrm{Hadrons})} \equiv \tilde{R}_b \equiv \frac{\tilde{Z}_b}{\tilde{Z}_b + \tilde{Z}_c + \tilde{Z}_{uds}} \tag{6.17}$$

where the $\tilde{Z}_q$ are the true number of $\mathrm{Z}^0 \to q\bar{q}$ events created by SLC.

We can then define a correction factor, κ, such that:

$$\tilde{R}_b = \kappa R_b = \kappa \frac{N_b}{N_b + N_c + N_{uds}} \tag{6.18}$$

where the N_q are the true number of $Z^0 \to q\bar{q}$ events that are written to tape and pass the event selection criteria.

If we assume that the SLD's data–to–tape efficiency and the overall trigger efficiency are both flavor–independent for hadronic events, the only remaining bias is specific to our event selection cuts. We define the event selection efficiency $\alpha_q = N_q/\gamma\tilde{Z}_q$ where the flavor–independent efficiencies are included in γ. We can estimate the α_q from the Monte Carlo, with the number of events passing the selection criteria as N_q and the number generated as $\gamma\tilde{Z}_q$.

$$\alpha_b = \left(\frac{8512}{16820}\right) = 0.506064 \pm 0.005485 \tag{6.19}$$

$$\alpha_c = \left(\frac{2589}{5176}\right) = 0.500193 \pm 0.009830 \tag{6.20}$$

$$\alpha_{uds} = \left(\frac{8924}{17604}\right) = 0.506930 \pm 0.005366 \tag{6.21}$$

$$\kappa = \left[R_b + \frac{\alpha_b}{\alpha_c}R_c + \frac{\alpha_b}{\alpha_{uds}}R_{uds}\right]^{-1} \tag{6.22}$$

$$\Rightarrow \kappa = 0.999047 \pm 0.011224 \qquad \Rightarrow \kappa = 0.999 \pm 0.011 \tag{6.23}$$

6.3 Total Error

The errors that depend on the significance cut and track requirement are shown in figure 6.7 for a three–track requirement. Figures 6.8 and 6.9 show the same errors for two– and four–track requirements. The minimum error is approximately at a significance cut of 3.0 on the three–track requirement plot, so we choose to use that cut and requirement. The total errors are shown in table 6.3 for this significance cut and track requirement.

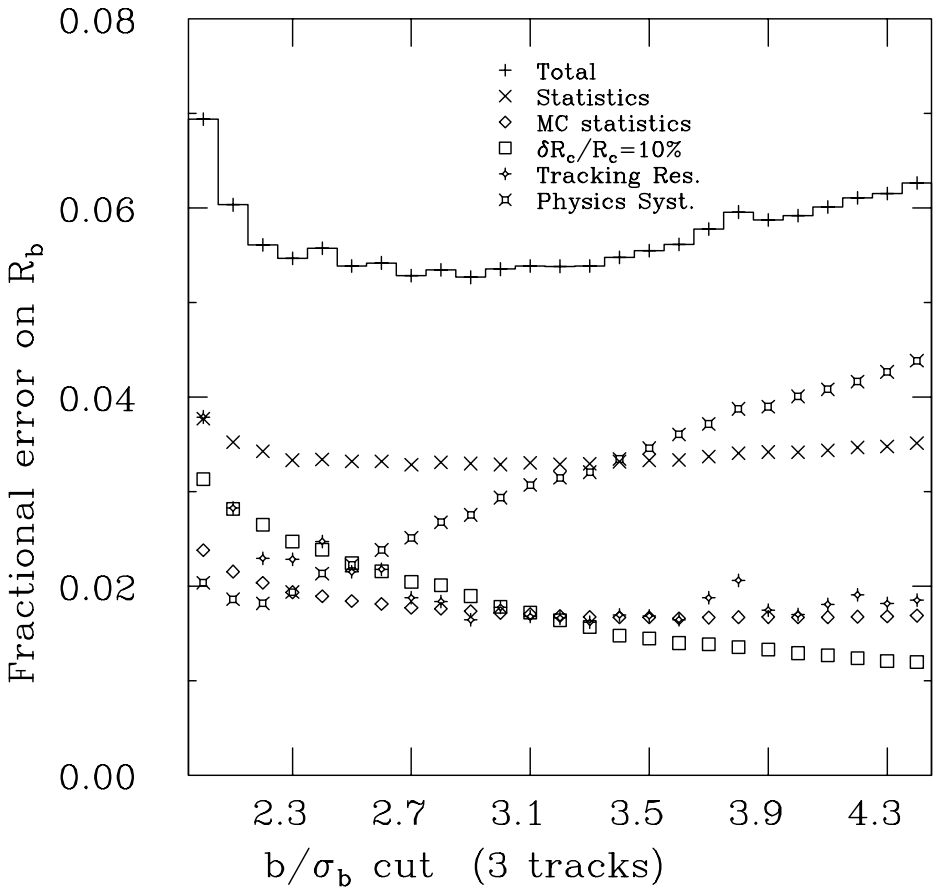

Figure 6.7: Total error as a function of significance cut for a three–track requirement.

Error	Absolute Error	Fractional Error
Statistics	0.0075	3.30%
Monte Carlo Statistics	0.0039	1.72%
Physics Systematics	0.0067	2.94%
R_c Uncertainty	0.0040	1.79%
Detector Resolution	0.0040	1.77%
Background	0.0004	0.20%
Event Selection Bias	0.0025	1.12%
Total	0.0124	5.46%

Table 6.3: Total errors.

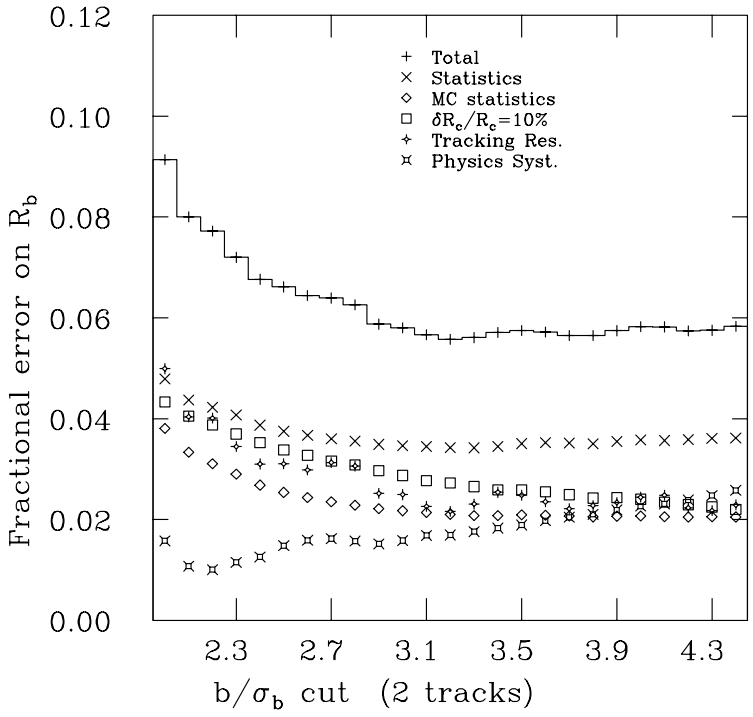

Figure 6.8: Total error as a function of significance cut for a two–track requirement.

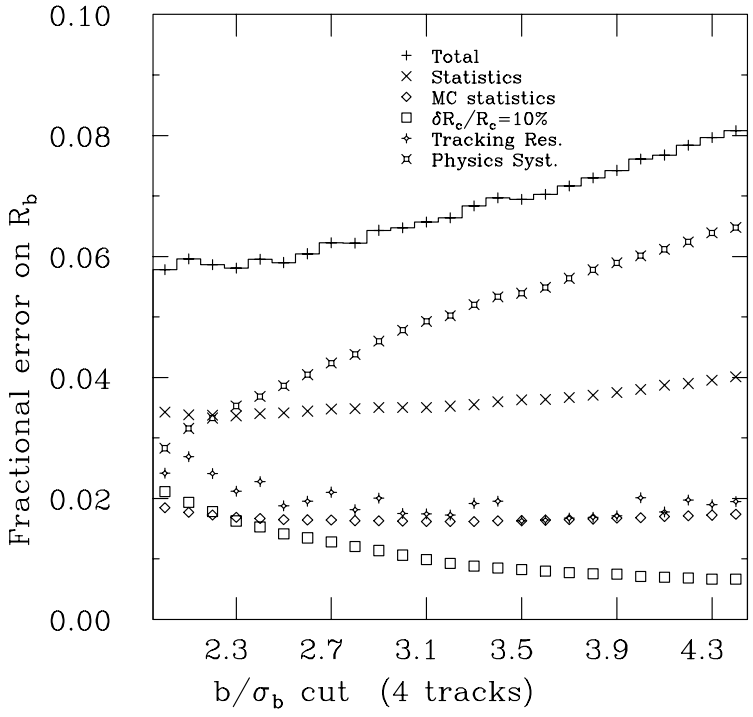

Figure 6.9: Total error as a function of significance cut for a four–track requirement.

6.4 Conclusions

We have measured the b/hadron branching fraction ratio:

$$R_b = 0.2270 \pm 0.0075_{(\text{stat.})} \pm 0.0091_{(\text{syst.})} \pm 0.0040_{(R_c)} \quad (6.24)$$

$$\Rightarrow R_b = 0.227 \pm 0.012 \quad (6.25)$$

This measurement is in agreement with the MSM and the world average. This value of R_b favors a negative m_t^2 but allows $m_t = 270$ GeV at one standard deviation.

The total uncertainty in our measurement of R_b (5.5%) is too large to place any significant constraints on theory or on new physics. It should be noted that the best R_b measurement reported to date[20] has a 1.7% error (systematics limited) and that measurement does not place any significant constraints either.

This analysis is valuable because it demonstrates the feasibility of using a three–dimensional impact parameter technique at SLD. This analysis also indicates the items which must improve if the SLD collaboration is to make a more precise measurement of R_b:

- More Z^0's — There are $\sim 50,000$ hadronic events from the 1993 run stored on tape and ready to be analyzed.
- Improved GEANT — We are currently upgrading the Monte Carlo to use the GEANT 3.15 package. This package uses a corrected Molière scattering routine, which should remove the need for some of the tracking resolution smearing.
- Improved materials list — Some parts of the SLD were approximated in the materials list for GEANT. In a few cases we can see discrepancies between data and Monte Carlo because of these approximations.
- Improved alignment — More data will allow us to align the detector elements more precisely. For this analysis, the z alignment of the VXD is crucial — better alignment should remove much of the tracking resolution smearing.

With this analysis and the improvements listed above, we expect to obtain $\sim 2.5\%$ precision. The LEP average will remain dominated by ALEPH's results, but they

should be able to push their systematic error slightly lower, resulting in a total precision of $\delta R_b/R_b \simeq 1.5\%$. Within a few years, the SLD collaboration expects to have a data sample of 10^6 Z^0's. At that point we could switch to a double tag method and significantly reduce our systematic error. Roughly half of this data will be taken with an improved vertex detector. Current plans are for a three–layer device with full ϕ coverage in each layer and longer ladders for better $\cos\theta$ coverage. Preliminary studies indicate that it is possible to find tracks using the vertex detector alone, so the improved $\cos\theta$ coverage can be fully utilized. Assuming an improvement in the world–average measurement of R_c, we expect to obtain precision of $\delta R_b/R_b \lesssim 1\%$. This uncertainty is not small enough to measure m_t, but it could be small enough to unearth a discrepancy in the minimal standard model. For example, if we were to measure $R_b = 0.2270$ with 1% precision we would rule out positive m_t^2 at 3σ. Alternatively, if m_t were measured to be ~ 200 GeV, an R_b measurement of 0.2210 with 1% precision would clearly eliminate the two Higgs doublet model.

Bibliography

[1] "Partial–Symmetries of Weak Interactions," S.L. Glashow, Nucl. Phys. **22** (1961) 579;
"A Model of Leptons," S. Weinberg, Phys. Rev. Lett. **19** (1967) 1264;
"Weak and Electromagnetic Interactions," A. Salam in *Elementary Particle Theory*, ed. N. Svartholm, Stockholm: Almquist and Wiksell (1968) 367.

[2] "Quantitative Tests of the Standard Model of Electroweak Interactions," W. Marciano, Ann. Rev. Nucl. Part. Sci. **41** (1991) 469.

[3] *See*, in general, *Z Physics at LEP 1*, G. Altarelli, R. Kleiss and C. Verzegnassi, eds., CERN Yellow Book 89–08 (1989).

[4] "High Energy Tests of the Electroweak Standard Model," M. Swartz, presented at the XVI*th* Inter. Symp. on Lepton–Photon Interactions, Ithaca, NY, August 1993.

[5] "Heavy Flavours," J.H. Kühn and P.M. Zerwas *et al.* in *Z Physics at LEP 1*, G. Altarelli, R. Kleiss and C. Verzegnassi, eds., CERN Yellow Book 89–08, vol. 1 (1989) 267.

[6] "Review of Particle Properties," Particle Data Group, Phys. Rev. **D45**, part II (1992) 1.

[7] "Estimation of Oblique Electroweak Corrections," M.E. Peskin and T. Takeuchi, SLAC–PUB–5618 (November 1991). (Subm. to Phys. Rev. **D**.)

[8] "Electroweak Radiative Corrections with an Effective Lagrangian: Four–Fermion Processes," D.C. Kennedy and B.W. Lynn, Nucl. Phys. **B322** (1989) 1.

[9] "Heavy Top and Heavy Higgs Control in Electroweak Observables," F.M. Renard and C. Verzegnassi, Phys. Lett. B **260** (1991) 225.

[10] "Limit on Mass Differences in the Weinberg Model," M. Veltman, Nucl. Phys. **B123** (1977) 89.

[11] "Precision Tests of the Electroweak Theory at the Z^0," G. Altarelli *et al.* in *Physics at LEP*, J. Ellis and R. Peccei, eds., CERN Yellow Book 86–02, vol. 1 (1986) 1.

[12] "A General Sum Rule for the Top Mass from b Physics on Z Resonance," F. Boudjema, A. Djouadi and C. Verzegnassi, Phys. Lett. B **238** (1990) 423.

[13] "$b\bar{b}$–Production at the Z–Resonance: A Challenge to the Standard Model," A. Djouadi *et al.*, Nucl. Phys. **B349** (1991) 48.

[14] "Electroweak One–Loop Corrections to the decay of the Neutral Vector Boson," A.A. Akhundov, D.Yu. Bardin and T. Riemann, Nucl. Phys. **B276** (1986) 1.

[15] "The Width of the Z Boson," W. Beenakker and W. Hollik, Z. Phys. C **40** (1988) 141.

[16] "A Determination of the $Zb\bar{b}$ Vertex Correction from LEP Data," A. Blondel, A. Djouadi and C. Verzegnassi, Phys. Lett. B **293** (1992) 253.

[17] "Radiative Corrections to Muon Lifetime, $W^{\pm}$ Mass and Longitudinal Polarization Asymmetry in $e^+e^- \rightarrow \mu^+\mu^-$ in $N = 1$ SUSY SU(3)×SU(2)×U(1) and $N = 1$ Sliding Singlet Models," B. Lynn, SLAC–PUB–3358 (June 1984). (Subm. to Nucl. Phys. **B**.)

[18] "Radiative Corrections to $\mathrm{B}(\mathrm{Z}^0 \rightarrow b\bar{b})$ in the Minimal Supersymmetric Standard Model," M. Boulware and D. Finnell, Phys. Rev. **D44** (1991) 2054.

[19] "Heavy Flavour Production in Z Decays," D. Decamp *et al.* (ALEPH Collaboration), Phys. Lett. B **244** (1990) 551.

[20] "A Precise Measurement of $\Gamma_{Z\to b\bar{b}}/\Gamma_{Z\to\text{hadrons}}$," D. Buskulic *et al.* (ALEPH Collaboration), Phys. Lett. B **313** (1993) 53.

[21] "Measurement of the Partial Width of $Z^0 \to b\bar{b}$ Using Event Shape Variables," D. Buskulic *et al.* (ALEPH Collaboration), Phys. Lett. B **313** (1993) 549.

[22] "A Measurement of the Partial Width of the Z^0 Boson into b Quark Pairs," P. Abreu *et al.* (DELPHI Collaboration), CERN–PPE/90–118 (1990), contributed to the XXV*th* Inter. Conf. on High Energy Physics, Singapore, 2 – 8 August 1990.

[23] "Measurement of the Partial Width of the Z^0 into $b\bar{b}$ Final States Using their Semi–leptonic Decays," P. Abreu *et al.* (DELPHI Collaboration), Z. Phys. C **56** (1992) 47.

[24] "Measurement of the Z^0 Branching Fraction to b Quark Pairs Using the Boosted Sphericity Product," P. Abreu *et al.* (DELPHI Collaboration), Phys. Lett. B **281** (1992) 383.

[25] "Measurement of the Average Lifetime of B Hadrons," P. Abreu *et al.* (DELPHI Collaboration), Z. Phys. C **53** (1992) 567.

[26] "Classification of the Hadronic Decays of the Z^0 into b and c Quark Pairs Using a Neural Network," P. Abreu *et al.* (DELPHI Collaboration), Phys. Lett. B **295** (1992) 383.

[27] "Measurement of $Z^0 \to b\bar{b}$ Decay Properties," B. Adeva *et al.* (L3 Collaboration), Phys. Lett. B **241** (1990) 416.

[28] "Measurement of $Z^0 \to b\bar{b}$ Decays and the Semileptonic Branching Ratio $\text{BR}(b \to \ell + X)$," B. Adeva *et al.* (L3 Collaboration), Phys. Lett. B **261** (1991) 177.

[29] "Measurement of $\Gamma_{b\bar{b}}/\Gamma_{\rm had}$ from Hadronic Decays of the Z," O. Adriani *et al.* (L3 Collaboration), Phys. Lett. B **307** (1993) 237.

[30] "Measurement of the $b\bar{b}$ Fraction in Hadronic Z Decays," J.F. Kral *et al.* (MARKII Collaboration), Phys. Rev. Lett. **64** (1990) 1211.

[31] "Measurement of the $b\bar{b}$ Fraction in Hadronic Z^0 Decays with Precision Vertex Detectors," R.G. Jacobsen *et al.* (MARKII Collaboration), Phys. Rev. Lett. **67** (1991) 3347.

[32] "A Study of Heavy Flavour Production Using Muons in Hadronic Z^0 Decays," M.Z. Akrawy *et al.* (OPAL Collaboration), Phys. Lett. B **263** (1991) 311.

[33] "A Measurement of Electron Production in in Hadronic Z^0 Decays and a Determination of $\Gamma(Z^0 \to b\bar{b})$," P.D. Acton *et al.* (OPAL Collaboration), Z. Phys. C **55** (1992) 191.

[34] "Measurement of $\Gamma(Z^0 \to b\bar{b})/\Gamma(Z^0 \to$ hadrons) Using Leptons," P.D. Acton *et al.* (OPAL Collaboration), Z. Phys. C **58** (1993) 523.

[35] "A Measurement of $\Gamma(Z^0 \to b\bar{b})/\Gamma(Z^0 \to$ hadrons) Using an Impact Parameter Technique," P.D. Acton *et al.* (OPAL Collaboration), CERN–PPE/93–79 (1993). (Subm. to Z. Phys. C.)

[36] "Measurements of B^0–$\overline{B^0}$ Mixing, $\Gamma(Z^0 \to b\bar{b})/\Gamma(Z^0 \to$ hadrons), and Semileptonic Branching Ratios for b–Flavoured Hadrons in Hadronic Z^0 Decays," R. Akers *et al.* (OPAL Collaboration), Z. Phys. C **60** (1993) 199.

[37] "Measurement of $\Gamma(Z^0 \to b\bar{b})/\Gamma(Z^0 \to$ hadrons) Using Impact Parameters and Leptons," R. Akers *et al.* (OPAL Collaboration), CERN–PPE/93–155 (1993). (Subm. to Z. Phys. C.)

[38] "A Preliminary Measurement of $R_b = \frac{\Gamma(Z^0 \to b\bar{b})}{\Gamma(Z^0 \to \rm hadrons)}$ at SLD," D. Su *et al.* (SLD Collaboration), SLAC–PUB–5972 (November 1992), presented at the 7*th* Meeting of the American Physical Society Division of Particles and Fields, Batavia, IL, 10 – 14 November 1992.

[39] "A Measurement of $R_b = \frac{\Gamma(Z^0 \to b\bar{b})}{\Gamma(Z^0 \to \text{hadrons})}$ at SLD," SLD Collaboration, SLAC–PUB–6292 (August 1993) presented at the XVI*th* Inter. Symp. on Lepton–Photon Interactions, Ithaca, NY, August 1993.

[40] "The OPAL Silicon Microvertex Detector," P.P. Allport *et al.*, Nucl. Inst. Meth. **A324** (1993) 34.

[41] "Recent Results and Running Experience of the New Aleph Vertex Detector," G. Batignani *et al.*, IEEE Trans. Nucl. Sci. **NS–39** (1992) 701.

[42] "Review of SLC Performance," N. Phinney, SLAC–PUB–5864 (August 1992).

[43] "The SLD Design Report," SLAC–Report–273, 1984 (unpublished).

[44] "The Polarized Electron Gun for the SLC," D. Shultz *et al.*, SLAC–PUB–5768 (March 1992).
"Polarized Light Sources for Photocathode Electron Guns at SLAC," M. Woods *et al.*, SLAC–PUB–5965 (December 1992).

[45] "Design and Performance of the SLD Vertex Detector, a 120 MPixel Tracking System," G.D. Agnew *et al.*, Proc. of the XXVI*th* Inter. Conf. on High Energy Physics, Dallas, TX, August 1992, p. 1862.

[46] "Performance of a Silicon CCD Pixel Vertex Detector in the SLD," M. Strauss, and *The Fermilab Meeting* (Proc. of the 7*th* Meeting of the American Physical Society Division of Particles and Fields), Batavia, IL, 10 – 14 November 1992, vol. 2, p. 1758.

[47] "Proposal to Upgrade the SLD Vertex Detector," The SLD Collaboration, October 1993 (unpublished).

[48] "Performance of the SLD Central Drift Chamber in the 1992 Physics Run," T. Markiewicz and L. Rochester, SLD Note #231, 22 March 1993.

[49] "Performance of the SLD Barrel CRID During the 1992 Physics Data Run," K. Abe *et al.*, SLAC–PUB–5986 (November 1992).

[50] "Performance of the CRID at SLD," K. Abe *et al.*, SLAC–PUB–6276 (June 1993).

[51] "The Lead–Liquid Argon Sampling Calorimeter of the SLD Detector," D. Axen *et al.*, Nucl. Inst. Meth. **A328** (1993) 472.

[52] "Estimate of Combined Triggering and Selection Efficiency for Hadronic Events," P.N. Burrows, H. Park, K.T. Pitts, J.M. Yamartino, SLD Note #229, 13 January 1993.

[53] "Tower Thresholds for LAC Total Energy Trigger," E. Vella, J. Yamartino, SLD Note #213, 6 February 1992.
"Hadronic Event Selection Using the LAC," John M. Yamartino, SLD Physics Note #14, 4 November 1992.

[54] "The SLD Calorimeter System," A.C. Benvenuti *et al.*, Nucl. Inst. Meth. **A289** (1990) 463.

[55] "First–Pass Determination of the Energy Scale in the SLD Calorimeter," S. González, SLD Physics Note #24, 9 October 1993.

[56] "First Results from the SLD Silicon Calorimeters," S.C. Berridge *et al.*, SLAC–PUB–5694, OREXP–91–1101 (July 1992).

[57] "Luminosity Measurement for the 1992 Run," K.T. Pitts, SLD Physics Note #20, 6 April 1993. *See also* nn. 1–5 from this reference.

[58] "Electronic Technology and the SLD Detector," J.D. Fox *et al.*, Nucl. Phys. B (Proc. Suppl.) **23A** (1991) 227.

[59] "Performance Report for Stanford/SLAC Multi–Channel Sample–and–Hold Device," G.M. Haller *et al.*, IEEE Trans. Nucl. Sci. **NS–33** (1986) 221. *See also* **NS–35** (1988) 217.

[60] "The Pad Readout Electronics of the SLD Warm Iron Calorimeter," P.N. Burrows *et al.*, Nucl. Phys. B (Proc. Suppl.) **23A** (1991) 219.

[61] "The Digital Data Acquisition Chain and the Cosmic Ray Trigger System for the SLD Warm Iron Calorimeter," A. Benvenuti *et al.*, Nucl. Inst. Meth. **A289** (1990) 577.

[62] "SLD Online Tutorial Handout," 11 April 1991 (unpublished).

[63] "The Aleph Event Builder," A. Marchioro, W. von Rüden and G. McPherson, IEEE Trans. Nucl. Sci. **NS–34** (1987) 133.

[64] "Coherent Parton Showers Versus Matrix Elements — Implications of PETRA/PEP Data," M. Bengtsson and T. Sjöstrand, Phys. Lett. **B185** (1987) 435.

[65] "QCD Generators," T. Sjöstrand, *et al.* in *Z Physics at LEP 1*, G. Altarelli, R. Kleiss and C. Verzegnassi, eds., CERN Yellow Book 89–08, vol. 3 (1989) 143.

[66] F. Halzen and A.D. Martin, *Quarks and Leptons: An Introductory Course in Modern Particle Physics*, (New York: John Wiley & Sons, 1984).

[67] J. Snyder, D. Su, R. Schindler and G. Punkar, SLD B–Physics Internal Memo, 15 October 1992.

[68] "GEANT3 User's Guide," R. Brun *et al.*, CERN DD/EE/84-1 (1989).

[69] D. Su, SLD B–Physics Task Force Meeting, 19 August 1993.

[70] "Track Fitting with Multiple Scattering: A New Method," P. Billior, Nucl. Inst. Meth. **225** (1984) 352.

[71] "Experimental Studies on Multijet Production in e^+e^- Annihilation at PETRA Energies," W. Bartel *et al.* (JADE Collaboration), Z. Phys C **33** (1986) 23.

[72] "First Measurement of the Left–Right Cross Section Asymmetry in Z Boson Production by e^+e^- Collisions" K. Abe *et al.*, Phys. Rev. Lett. **70** (1993) 2515.

[73] "Background Measurement for the 1992 A_{LR} Analysis," R. Ben–David and H. Park, SLD Physics Note #18, July 1993.

[74] "Neutral Weak Couplings of Beauty and Charm," D. Brown, presented at the $5th$ Inter. Conf. on Heavy Flavor Physics, Montreal, Canada, July 6 – 10, 1993.

[75] "A Measurement of the Branching Ratio of the Z Boson to Bottom Quarks Using Precision Tracking," R.G. Jacobsen, SLAC–Report–381, 1991 (unpublished thesis).

[76] D. Su, private communication.

[77] R. Ben–David, private communication.

[78] "A Study of Jet Rates and Measurement of α_s at the Z^0 Resonance," Jan A. Lauber, SLAC–Report–413, 1993 (unpublished thesis).